LANDESAMT FÜR UMWELT,
LANDWIRTSCHAFT
UND GEOLOGIE

Freistaat
SACHSEN

The upper zone of the Storkwitz Carbonatite

Geoprofil, Heft 15 (2020)

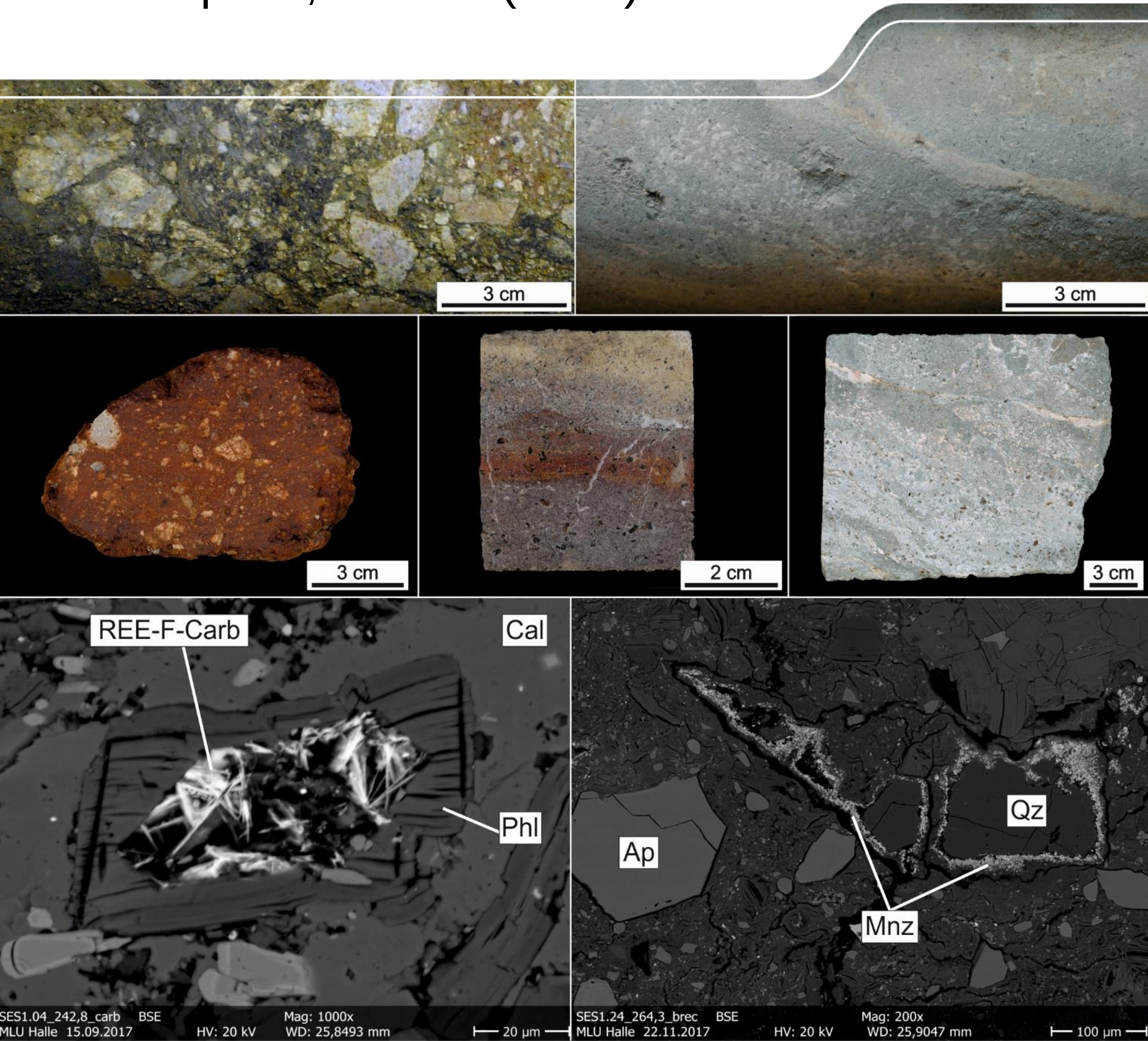

Geochemical and mineralogical characterization of the REE-mineralisation in the upper zone of the Storkwitz Carbonatite Complex from drill core SES-1/2012

Max Niegisch, Andreas Kamradt, Gregor Borg

MARTIN-LUTHER-UNIVERSITÄT
HALLE-WITTENBERG

LANDESAMT FÜR UMWELT,
LANDWIRTSCHAFT
UND GEOLOGIE

Freistaat
SACHSEN

Geoprofil	Freiberg	**15** (2020)	1-92	59 Fig., 22 Tab.

Geochemical and mineralogical characterization of the REE-mineralisation in the upper zone of the Storkwitz Carbonatite Complex from Drill core SES-1/2012

Max Niegisch, Andreas Kamradt, Gregor Borg

Table of Contents

List of figures

List of tables

List of abbreviations

REE	–	Rare earth elements
LREE	–	Light rare earth elements
HREE	–	Heavy rare earth elements
UML-CR	–	Ultramafic Lamprophyre - Carbonatite complex
MGCH	–	Mid-German Crystalline High
IUGS	–	International Union of Geological Sciences
XRF	–	X-ray fluorescence
ICP-MS/ES	–	Inductively coupled plasma mass spectrometry / emission spectrometry
SEM	–	Scanning electron microscope
(SEM)-BSE	–	Backscattered electron
(SEM)-EDX	–	Energy-dispersive X-ray spectroscopy
SWIR	–	Short-wavelength infrared
NIR	–	Near infrared
VIS	–	Visible light
EPMA	–	Electron probe microanalysis

Abbrevations of minerals

Ab	Albite*
Al-Silic	Alumosilicates
Ap	Apatite*
Bas	Bastnaesite*
Bdy	Baddeleyite*
Brt	Barite*
Cal	Calcite*
Ccp	Chalcopyrite*
Gth	Goethite*
Hem	Hematite*
Mag	Magnesite*
Mnz	Monazite*
Pcl	Pyrochlore*
Phl	Phlogopite*
Py	Pyrite*
Qz	Quartz*
REE-F-Carb	REE-fluorocarbonates
Sa	Sanidine*
Syn	Synchisite
Urp	Uranophane
Zcl	Zirkonolite

* taken from WHITNEY & EVANS (2009)

Abstract

The Storkwitz-Carbonatite is a Late Cretaceous intrusive complex, which is well-explored by a relatively large number of exploration bore holes both from the 1970ies, 1980ies and from one more recent bore hole, SES-1/2012. The carbonatite complex hosts a (currently) marginally economic mineralisation of rare earth elements (REE) and niobium, which is technically still difficult to recover. The upper part of the carbonatitic body is located some 100-120 m below the Pre-Cenozoic land surface, which in turn is overlain by approximately 100 m of glacial, fluvio-glacial, and fluviatile sediments.

The aim of this study was to characterize the mineralisation in the upper part of the intrusion geochemically and mineralogically and to try to identify indications of a supergene overprint on the late magmatic to hydrothermal mineralisation. Fresh drill core samples from the exploration bore hole SES-1/2012 have revealed that the mineralisation is associated with a carbonatitic igneous breccia body and also with several alvikite veins. The breccia body is very heterogeneous, displays a variety of matrix colours and also a range of matrix-to-clast ratios.

Non-destructive analytical methods like p-XRF analyses, magnetic susceptibility measurements, and SWIR-reflectance spectroscopy were carried out directly on the drill core. The samples were also investigated by optical microscopy, scanning electron microscopy (SEM) and their geochemical composition was analysed by whole rock analyses at a certified laboratory.

The geochemical results confirm the presence of a REE-enriched zone, which is closely associated with the carbonatitic intrusion, whereas the porphyritic clasts of the breccia and the porphyritic wall rocks do not contain any REE mineralisation. The mineral composition of the examined sections is very heterogeneous and comprises magmatic phenocrysts as well as a large variety of secondary mineral phases, which were formed by either hypogene, ascending late magmatic carbothermal or subsequent hydrothermal processes or alternatively by deeply descending meteoric supergene processes. The secondary processes were strongly oxidising and formed abundant hydrated mineral phases. The REE ore minerals are predominantly secondary monazites and REE-fluorocarbonates, which both occur in igneous breccias as well as in alvikite veins. Other minerals such as apatite or pyrochlore are slightly enriched in REE. However, there is no significant correlation between the proportion of REE-bearing minerals observed microscopically and the geochemical REE concentration.

Several mineral phases display intensive alteration textures and parageneses and especially the cryptocrystalline matrix of the breccias indicate a supergene influence. The supergene overprint has thus caused the alteration and formation of supergene Fe-oxyhydroxides and of an alumo-siliceous matrix and the local redistribution of the REE within the REE-mineral phases. However, no signs were detected that indicate a dissolution, transport, and especially fractionation of the dissolved REE in the (deep) supergene environment.

Zusammenfassung

Der Storkwitz-Karbonatit ist ein Intrusivkomplex aus der Oberkreide, welcher durch ein Bohrprogramm, beginnend in den 1970er Jahren und einer Explorationsbohrung aus dem Jahr 2012 (SES-1/2012) relativ engmaschig exploriert wurde. Der Komplex besitzt eine (derzeit) kaum wirtschaftlich gewinnbare Mineralisation von Seltenen Erden Elementen (SEE) und Niob. Der oberste Teil der Karbonatitintrusion befindet sich 100-120 m unter der prä-Känozoischen Landoberfläche, die wiederum von circa 100 m eiszeitlichen Sedimenten (glazial bis fluviatil) überdeckt wird.

Ziel der vorliegenden Untersuchung war es, den mineralisierten Bereich aus dem obersten Teil der Intrusion nach geochemischen und mineralogischen Gesichtspunkten anhand von Bohrkernproben zu charakterisieren und dabei mögliche Hinweise auf eine supergene Überprägung der spät-magmatisch bis hydrothermalen Mineralisation zu finden. Anhand dieser Proben, entnommen aus der Bohrung SES-1/2012, zeigt sich, dass die Mineralisation an einen karbonatitisch-magmatischen Brekzienkörper und zusätzlich an einige Alvikitadern gebunden ist. Der Brekzienkörper ist in sich sehr heterogen und zeigt eine Reihe verschiedener Matrixfarben und stark variierende Matrix-zu-Klasten Verhältnisse.

Zerstörungsfreie Untersuchungsmethoden wie p-XRF Analysen, Messungen der magnetischen Suszeptibilität und kurzwellige Infrarot-Spektroskopie wurden direkt am Bohrkern durchgeführt. Des Weiteren wurden Proben mittels optischer Mikroskopie, Rasterelektronenmikroskopie und geochemischen Gesamtgesteinsanalysen in einem zertifizierten Labor untersucht.

Die Ergebnisse der geochemischen Analysen bestätigen das Vorhandensein einer SEE-angereicherten Zone, welche eng an die karbonatitische Intrusion geknüpft ist, wohingegen die porphyrischen Klasten der Brekzien sowie das porphyrische Nebengestein keine SEE-Mineralisation aufweisen. Die mineralogische Zusammensetzung des untersuchten Bohrkernabschnittes ist sehr heterogen und umfasst neben magmatischen Einsprenglingen eine Vielzahl von sekundären Mineralphasen, die sich entweder hypogen, spät magmatisch, carbothermal bis hydrothermal oder durch tiefe meteorische Prozesse supergen gebildet haben können. Die sekundären Mineralphasen belegen die intensive Oxidation und Hydratation der Paragenese. Die SEE-Erzminerale sind hauptsächlich Monazit und SEE-Fluorokarbonate, die sowohl in der Matrix der magmatischen Brekzien als auch in den Alvikitadern vorkommen. Weitere Minerale wie Apatit oder Pyrochlor sind ebenfalls leicht an SEE angereichert. Eine signifikante Korrelation zwischen dem mikroskopisch beobachteten Anteil der SEE-führenden Mineralphasen und der geochemischen SEE-Konzentration wurde nicht festgestellt.

Einige Mineralphasen zeigen deutliche Alterationstexturen und -paragenesen, wobei speziell die kryptokristalline Matrix der Brekzien auf einen supergenen Einfluss hindeutet. Die supergene Überprägung kann somit die Alteration, die Formation der Fe-Oxihydroxide und der alumo-silikatischen Matrix sowie die lokale Neuverteilung der SEE mit der Bildung der sekundären SEE-Mineralphasen verursacht haben. Dennoch konnten keine geochemischen Hinweise gefunden werden, die auf eine substantielle Mobilisierung, Transport oder Fraktionierung der SEE in einer supergenen Umgebung deuten.

1. Introduction

In the 1970s and 1980s, a cluster of ultramafic and carbonatitic intrusions was detected by an intensive drilling campaign by the SDAG Wismut near Delitzsch. This Ultramafic Lamprophyre - Carbonatite complex (UML-CR) of Delitzsch is located at the border between Saxony and Saxony-Anhalt 20 km north of Leipzig and 25 km east of Halle (WASTERNACK 2008). Carbonatites are defined by the International Union of Geological Sciences (IUGS) as igneous rocks, with more than 50 % carbonate minerals. There are many aspects of the genesis, transport, solubility and alteration of carbonatites and their melts, which are poorly understood jet (MITCHELL 2005). Economically, these rocks can be interesting, because of their high amounts of rare earth elements (REE) and associated elements like yttrium, zirconium and niobium. Carbonatites have the highest contents of REE of all igneous rocks (CULLERS & GRAF 1984).

Therefore, carbonatite occurrences of the UML-CR became interesting again during the rare earth element crisis from 2009 to 2012. In 2009, the production of REE was nearly completely accumulated in China. Due to introduced production quotas, export taxes and other restrictions, the price for REE has risen dramatically (VONCKEN 2016). Since this crisis, many REE deposits were explored, so that the monopole of china will decrease until 2020 (POTHEN 2013). In these years, the State Office for Geology and Mining Saxony-Anhalt (LAGB) and the Saxon State Office for Environment, Agriculture and Geology (LfULG) carried out a couple of projects with the Martin-Luther-University Halle-Wittenberg to re-evaluate the carbonatites of the UML-CR Delitzsch (UHDE 2011; MARIEN 2014; IWAN 2017). The Storkwitz-Structure, a carbonatite body near the village of Storkwitz, was the most promising structure, which was described and drilled by the SDAG Wismut (MARIEN et al. 2012). In 2012, the Seltenerden Storkwitz AG began a new drilling project. The resulting drill core SES-1/2012, which was the subject of this project, has mineralised sections with the typical increased amounts of REE and niobium (REICHERT et al. 2015).

The surface nearest penetrated parts of the carbonatite are located approximately 120 m below the Pre-Cenozoic surface, so a supergene alteration and enrichment of the REE could be possible. Aim of this project was, to find hints for supergene processes. Therefore, the used part of the drill core is characterized with geochemical and mineralogical methods to derive hints on the genesis of the mineralisation and the associated processes and environments.

Regional geology

The UML-CR Delitzsch is located on the southern border of the Mid-German Crystalline High (MGCH) (KRÜGER et al. 2013). The MGCH is a NE-SW trending Variscan basement wedge, which is part of the Rheic suture (Fig. 1 a). The Rheic suture was formed by closure of the Rheic ocean during the collision between Avalonia and Saxo-Thuringia (ZEH & GERDES 2010). The MGCH consists of 2 major units, which come from different geotectonic setting and were juxtaposed during the Variscan collision. Unit 1 includes relics from a magmatic arc, which was formed by the subduction of the Rheic ocean under Saxo-Thuringia between 360 and 330 Ma and contains Cambrian to Ordovician sediments (ZEH & GERDES 2010).

Unit 2 consists of a metasediment-metabasite succession, which is part of the Rhenohercynian domain. Additional, gneisses belong to this unit, which are interpreted to be relics of a Late Silurian to Early Devonian magmatic arc. Outcrops of the MGCH in Germany are located for example in the Odenwald, in the Spessart, in the Ruhla Crystalline Complex and in the northern Zone of the Kyffhäuser (ZEH & GERDES 2010). In the area of the UML-CR Delitzsch, the MGCH is located 100 to 120 m under the recent surface with an overlap of Cenozoic sediments (STANDKE 1995). It contains the Palaeozoic sediments of unit 1, which are deposited on top of the Cadomian basement (KRÜGER et al. 2013) and represent members of the Rothstein-, Zwethau- and Delitzsch-Formations. The Rothstein- and Zwethau-Formations contain a variety of sediments like flysch layers, siltstones, sandstones, limestones and marl (EHLING 2008).

Magmatic intrusions occur seldom. Due to Late Variscan magmatism, contact metamorphism took place locally and was detected at some drill cores. The Delitzsch-Formation consists of alternating strata of mudstones, siltstones and sandstones and a rare occurrence of meta-basalts (EHLING 2008).

The hanging wall succession overlaying the sediments of the MGCH is characterized by conglomerates, sand- and siltstones, pyroclastic rocks, volcanic rocks and occasional organic rich shale and is stratigraphically assigned to the Early Carboniferous Klitschmar-Formation (SCHWAB & EHLING 2008). In the Late Variscan phase, magmatism led to the intrusion of differentially evolved magma batches in the area around the UML-CR. In the southeast of Delitzsch, a multiphase intrusive complex of 13 x 8 km represents one of these magmatic bodies, whereas it mainly consists of diorites with an age of 237 Ma and granitoids with an age of 292 Ma (WALTER & SCHNEIDER 2008).

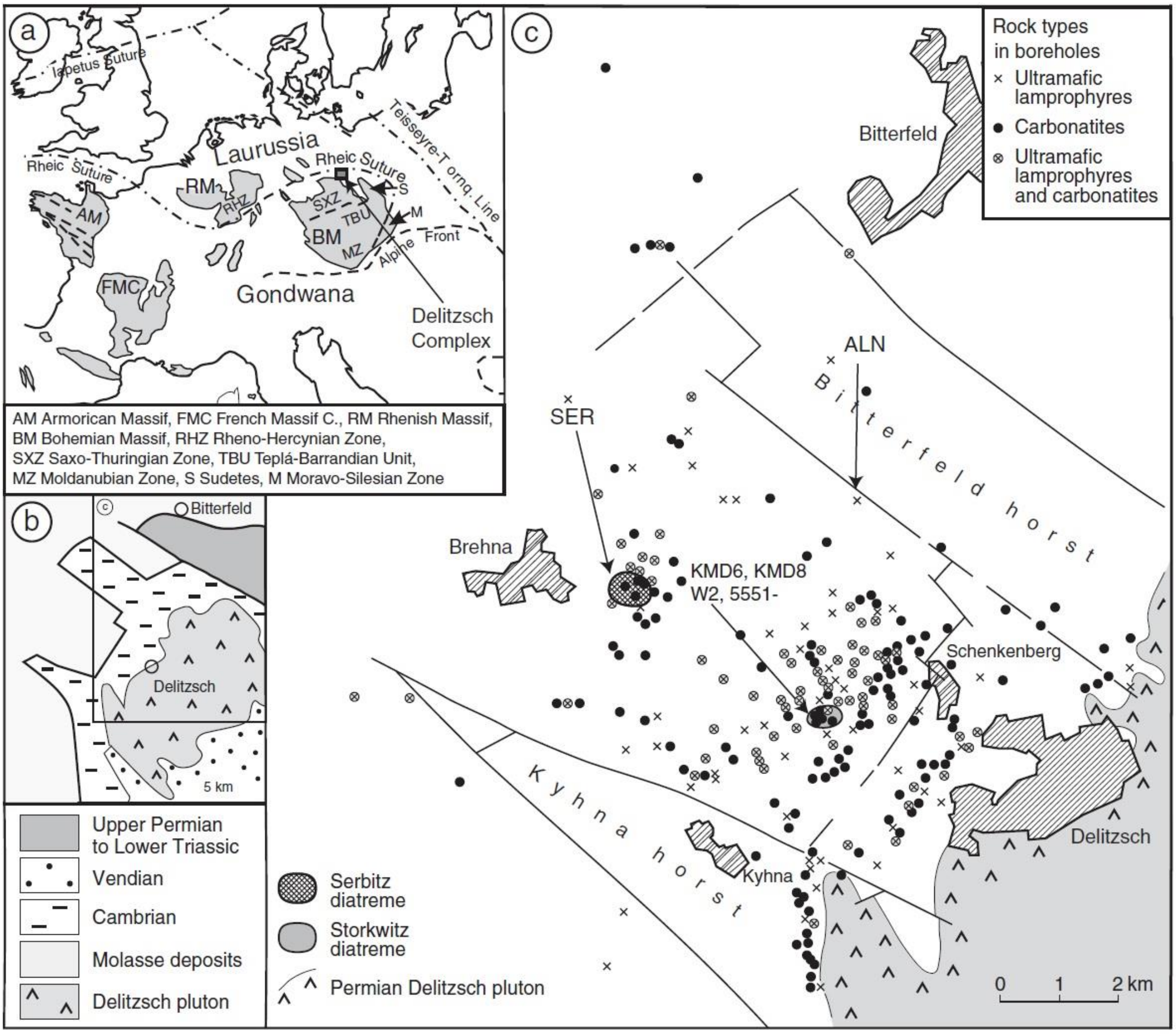

Figure 1: a – Regional geology and plate tectonic of central europe.; b, c – Position of the UML-CR Delitzsch with an overview of some drillings carried out by the SDAG Wismut (KRÜGER et al. 2013).

Abbildung 1: a – Regionale Geologie und Plattendtektonik von Mitteleuropa; b, c – Lage der UML-CR Delitzsch mit einigen, von der SDAG Wismut abgeteuften, Bohrungen (KRÜGER et al. 2013)

In Storkwitz and the near Schenkenberg, a small porphyritic laccolith was detected by magnetic exploration in the course of a drilling program conducted by the SDAG Wismut in the 1960s, which is poorly documented by scientific publications or difficult of access, because of confidentiality of internal reports. The laccolith is a light grey and fine crystalline quartz-porphyry and contains 0.6 to 7 m thick andesite Late Carboniferous (WASTERNACK 2008). In the regional geology, this unit is called “Schenkenberger Plagiogranitporphyr” (WISMUT GMBH 1999).

The UML-CR Delitzsch is located on the intersection of two fault systems, the E-W trending Delitzsch-Doberlug-Syncline and the N-S trending Leipzig-Rostock-Regensburg fault zone (WASTERNACK 2008). During reorganization of the regional stress field, these fault systems were repeatedly reactivated and caused horst and graben structures, near the UML-CR Delitzsch, namely the “Bitterfelder Horst” and the “Kyhnaer Horst” with a transform offset up to 3 km (WAGNER et al. 1997). Reactivating events were for example the development of the Oslo Rift, the opening of the Tethys and the Atlantic, and the Alpine Orogeny (KRÜGER et al. 2013).

During the Late Cretaceous, the UML-CR Delitzsch with its carbonatites and ultramafic lamprophyres is emplaced into a heterogeneous series of the Palaeozoic and Carboniferous sediments and the Late Variscan volcanic rocks. That has been revealed by intensive drilling campaigns in the 1970s and 1980s carried out by the SDAG Wismut (Fig. 1 b, c). Based on these drillings, the extension of the complex of

Table 1: Overview of the six intrusion stages of the Storkwitz-Structure (after WASTERNACK 2008).

Tabelle 1: Übersicht der sechs Intrusionsphasen der Storkwitz-Struktur (nach WASTERNACK 2008)

Stage	Event	Depth level	Rock types
I	Intrusion of carbonatitic magma body	Hypabyssal	Dolomite–carbonatite
II	Intrusion of ultramafic and alkali lamprophyres	Subvolcanic	Ultramafic lamprophyres (alnöite, aillikite, monchiquites)
III	Formation of diatremes (‘intrusive breccia’)	Subvolcanic	Dolomite–carbonatite (beforsite) with xenoliths (UML and dolomitecarbonatite)
IV	Intrusion of lamprophyres within diatremes of stage III	Subvolcanic	Ultramafic and alkalilamprophyres
V	Formation of beforsite dikes	Subvolcanic	Dolomite–carbonatite (beforsites) without xenoliths
VI	Formation of carbonate dikes	Subvolcanic	Calcite–carbonatite (alvikite), partly with xenoliths

80 m^2 was proved. Further estimations incorporating more peripheral drilling locations suggest that the size could be expanded to approximately 450 km2 (WASTERNACK 2008). Intrusive breccias, diatremes, dikes, sills, pipe shaped intrusions of lamprophyres (alnöits, monchiquites, etc.) and carbonatites (dolomite- and calcite-carbonatite) take evidence for subvolcanic intrusions. These were found up to a depth range of 600 m below ground level. The carbonatite occurrence of Storkwitz is characterized by intrusive dolomite-carbonatite breccias, which among other contain xenoliths of coarse-grained dolomite–carbonatite (rauhaugite), fenites, and glimmerites. This indicates the presence of a hypabyssal stockwork, which was not yet explored by the drill programs (KRÜGER et al. 2013). A total of six intrusion stages can be distinguished, a first hypabyssal stage and later five subvolcanic intrusions (Tab. 1) (RÖLLIG et al. 1995).

The timing of the emplacement of the different subvolcanic stages was dated with the U/Pb, the Rb/Sr and the 87Sr/86Sr isotope system. The determined ages correlate, so that for the main phase an age of 75 Ma to 71 Ma can be supposed (KRÜGER et al. 2013).

Carbonatites mainly occur as intrusive breccias with carbonatic matrix and clasts, which mostly consist of the adjacent magmatites and sediments. These clasts are mostly angular. Some breccias contain also xenoliths from the hypabyssal stage or deeper levels of the crust. These rock fragments are often more rounded, because of the longer way of transportation. On basis of the occurrence of these xenoliths two different types of breccias were distinguished by their composition and geochemical signature. The type A includes all intrusive breccias with the ultramafic lamprophyre clasts, while breccias without these clasts belong to type B. The size of the clasts is varying from some millimetres to a few cubic metres and concentration from less than 10 to over 90 volume percent (RÖLLIG et al. 1990). In addition to the breccias, there are also fine crystalline carbonatite veins, which are composed of more than 50 vol.% of calcite. The compact carbonatites and the carbonatite breccias occur as dolomite-carbonatite (beforsite) as well as calcite-carbonatite (alvikites) (KRÜGER et al. 2013).

The drilling spot of the examined drilling (SES-1/2012) is located in the southwest of the village Storkwitz (REICHERT et al. 2015) and penetrated the Storkwitz-Carbonatite, a subvolcanic diatreme like carbonatite-breccia intrusion of the UCC Delitzsch (Fig. 2) with a big amount of REE and Nb.

1.2 Carbonatites

As described in the introduction, Carbonatites are igneous rocks, which may be plutonic or volcanic origin and contain more than 50 % carbonate minerals (STRECKEISEN 1979). This definition, which is also accepted as the official IUGS definition, is very general, which is caused by the fact, the genesis of carbonatite and the behaviour of the magma is not understood very well jet (MITCHELL 2005).

Carbonatites in general are mantle derived and there are three scenarios, how a carbonatitic magma can arise. They can be generated by (a) primary mantle melting, (b) liquid immiscibility and (c) crystal fractionation. In first scenario, there has to be a metasomatic enrichment of CO_2 in the mantle, which causes the building of a primary magma. Subducted oceanic crust could be a possible source of the CO_2 (BELI et al. 1998). Because of the association of the most carbonatite with silicate magmatic rocks, the other two scenarios are conceivable. The cooling of a siliceous-carbonatitic magma in the mantle would cause immiscibility and separation in a siliceous melt and a carbonatitic melt. This would explain the common association of both igneous rocks (Panina & Motorina 2008).

The third scenario is a fractionated crystallization of a siliceous magma, which causes the transformation in a residual carbonatite melt (Bell et al. 1998). The classification of carbonatite is defined by the mineralogy and grain size (Tab. 2) or their main oxides (Tab. 3), if the carbonates are too small for identification (Le Maitre et al. 2002).

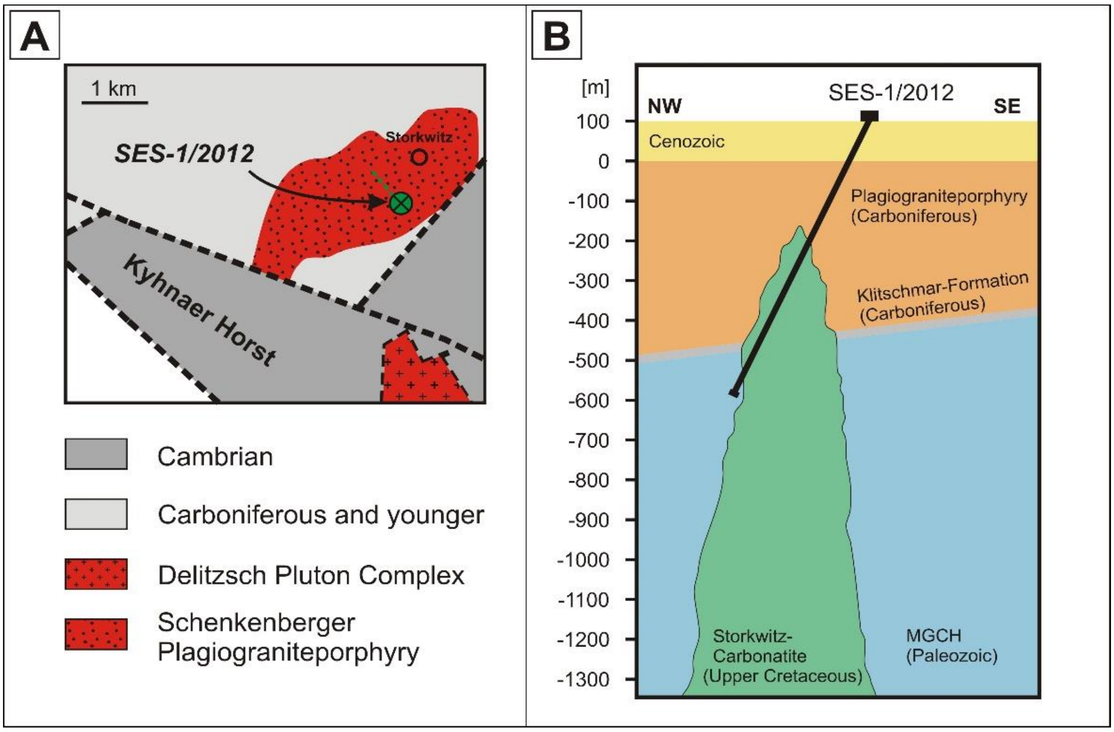

Figure 2: A – Location of the drilling spot of SES-1/2012 (modified after Ehling 2008).; B – Simplified profile of the drilling SES-1/2012 (modified after Seltenerden Storkwitz AG 2012).

Abbildung 2: A – Lage der Bohrung SES-1/2012 (verändert nach Ehling 2008); B – Vereinfachtes Profil des Storkwitz-Karbonatits mit der Bohrung SES-1/2012 (verändert nach Seltenerden Storkwitz AG 2012)

Table 2: Classification of carbonatites by their main carbonates and their grain size (after Le Maitre et al. 2002).

Tabelle 2: Klassifikation von Karbonatiten nach den Hauptkarbonaten und deren Korngröße (nach Le Maitre et al. 2002)

Carbonatite subtype	Main carbonate	Grain size
Calcite-carbonatite	Calcite	-
Alvikite	*Calcite*	*Fine-grained*
Sövite	*Calcite*	*Coarse-grained*
Dolomite-carbonatite	Dolomite	-
Beforsite	*Dolomite*	*Fine-grained*
Rauhaugite	*Dolomite*	*Coarse-grained*
Ferrocarbonatite	Fe-rich carbonates	-
Natrocarbonatite	Na, K, Ca-rich carbonates	-

Table 3: Classification of carbonatites by their main oxides (after Le Maitre et al. 2002).

Tabelle 3: Klassifikation von Karbonatiten nach deren Hauptoxiden (nach Le Maitre et al. 2002)

Carbonatite subtype	Main oxides
Calciocarbonatite	CaO > 80 %
Magnesiocarbonatite	SiO_2 < 20 %, CaO > 80 %, MgO/(FeO + Fe_2O_3 + MnO) > 1
Ferrocarbonatite	SiO_2 < 20 %, CaO > 80 %, MgO/(FeO + Fe_2O_3 + MnO) < 1
Silicocarbonatite	SiO_2 > 20 %

Until the year 2008, there were 527 carbonatite occurrences described (Fig. 3). These are mainly associated with extensional tectonics, rifting and crossing fault-systems. The majority of the carbonatites placed in an intra-plate setting, but also minor at plate boundaries. Furthermore, there are carbonatites linked to orogenic belts, although they occur rarely directly in an orogen (Woolley 1989).

There seems to be an affinity of carbonatites to surface near Precambrian rocks (Woolley & Kjarsgaard 2008). Furthermore, carbonatites can occur in clusters. The associated deep fault systems can be reactivated several times, so that a group of intrusions accumulate (Bell et al. 1987).

2. Methodology

Due to the high lithological variability of the drill core, preliminary examinations with a portable XRF and a susceptibility-meter were carried out, to determine the best sampling spots. Samples were taken from 33 positions of the drill core, which were used for a geochemical whole rock analysis. Additionally, thin sections were prepared from 30 samples. The selection of the sampling spots was carried out according lithological aspects, so that the sample suite extracted from the drill core comprise five samples account to porphyries, 17 to breccias and 11 to alvikites. As main investigations, the geochemical whole rock analysis and the microscopy were made, in which optical microscopy and scanning electron microscopy (SEM)

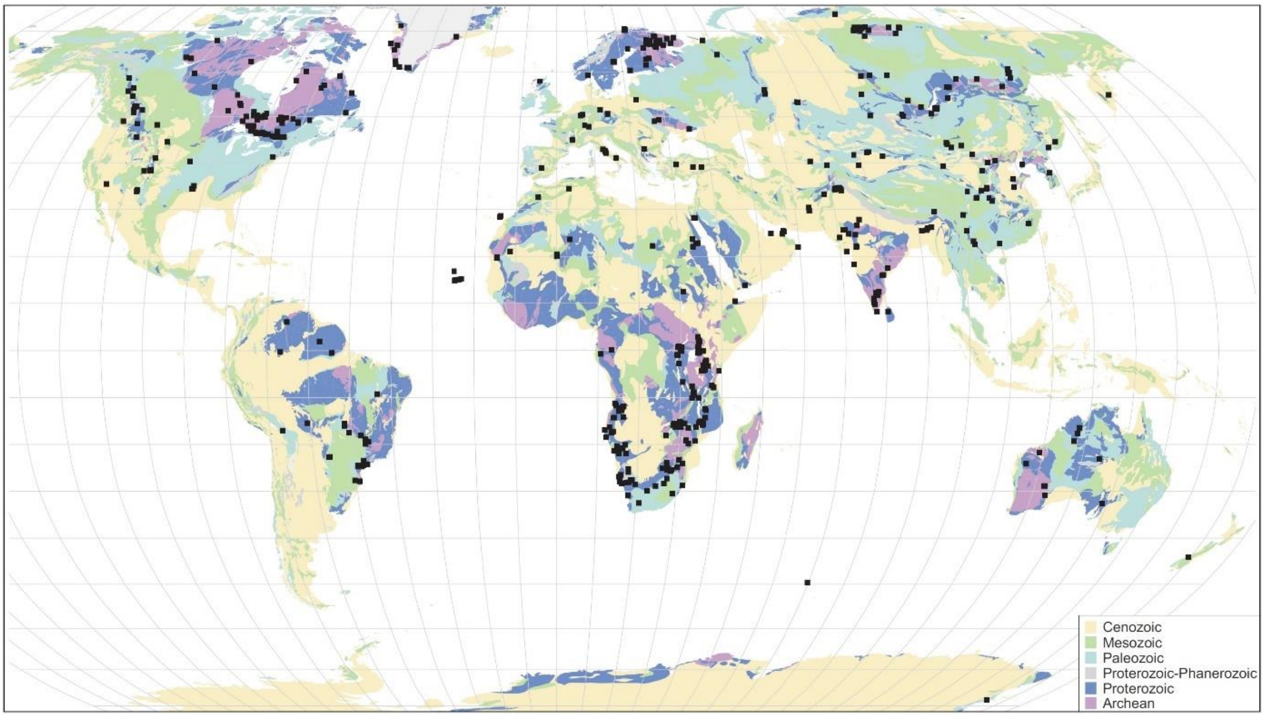

Figure 3: World map with all carbonatite occurrences known in 2008 (Woolley & Kjarsgaard 2008).

Abbildung 3: Weltkarte mit allen im Jahr 2008 bekannten Karbonatitvorkommen (Woolley & Kjarsgaard 2008)

were used. The reflectance spectroscopy was used supplementary, to get additional information about the minerals and phases, which could not be classified with the microscopic methods.

2.1 Portable XRF

For the logging with a pXRF (Thermo Scientific Niton Xl3t), the Ta/Hf mode for environmental samples was used with a measuring time of 90 s (30 s standard filter and 60 s filter for heavy elements), in which it is possible, to measure the concentration of some REEs, especially lanthanum and cerium. Due to the usage of the "small spot" option, the measuring field is 3 mm in diameter, so separate measurements of small heterogeneous areas such as the matrix and the clasts of breccias can be performed. If possible, measurement took place directly on the core and otherwise on crushed and dried samples with a size < 2mm in diameter. Because the portable XRF results correlate linearly with the results from other methods (ICP-ES, ICP-MS, wavelength-dispersive XRF), the measurement can easily be calibrated (RYAN et al. 2017) with sample returns from the geochemical whole rock analyses (Fig. 4).

2.2 Magnetic susceptibility

The measurement of the volume magnetic susceptibility was carried out with a "MS2 Magnetic Susceptibility System" with a "MS2E Core Logging Sensor" from Bartington and took place directly on the core.

The spot size of the sensor is 10.5 mm in diameter and the maximum depth of total response is 3.8 mm and 50 % response in a depth of 1 mm, so that the measurement represents a surface analysis (Bartington Instruments Ltd.).

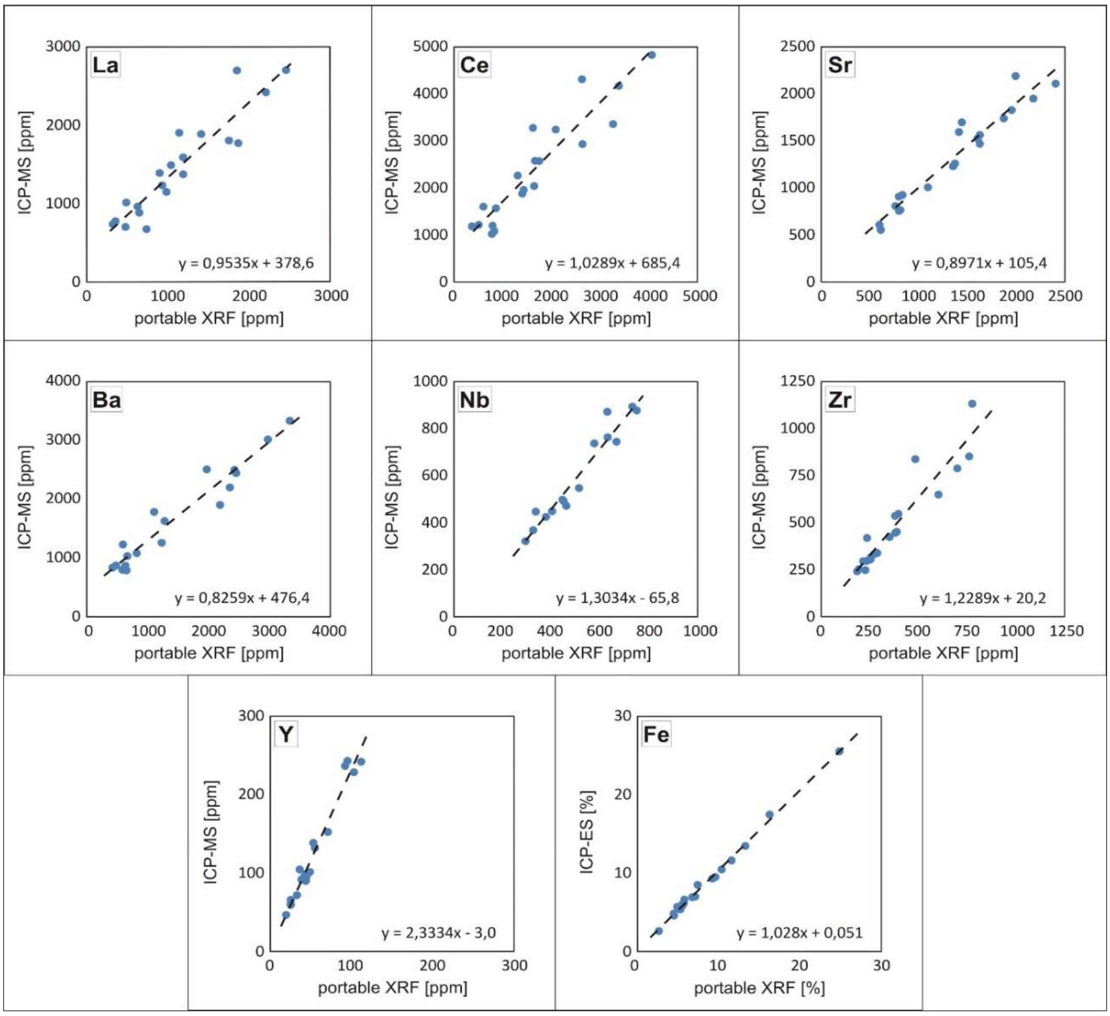

Figure 4: ICP-MS/ES vs. portable XRF - plot for several elements. The linear correlation is clearly visible for all these elements although the scattering of the plots and the slope of the correlation graph is varying.

Abbildung 4: ICP-MS/ES – portable RFA-Diagramm. Die Lineare Korrelation zwischen den Messverfahren ist bei allen Elementen sichtbar, auch wenn die Qualität der Korrelation von Element zu Element variiert.

2.3 Geochemical analysis

The samples (whole rock samples) were crushed, and analysed by Bureau Veritas. In the chosen package, the major oxides were measured by inductively coupled plasma emission spectrometry (ICP-ES) and trace elements, including the rare earth elements, by inductively coupled plasma mass spectrometry (ICP-MS).

2.4 Microscopy

The main phases and textures were analysed by normal polarization and reflectance microscopy. The used microscope was an Axiophot polarization microscope from Carl Zeiss with a Digital Sight DS-Fi2/ DS-U3 analogue-to-digital converter from Nikon. Furthermore, the SEM from the Institute of Geosciences and Geography of the Martin-Luther-University Halle-Wittenberg, a SEM JSM 6300 SEM from JOEL with the EDX-detector XFlash 5010 from Bruker, was used. The acceleration voltage was approximately 20 kV and the resolution of the EDX-detector is 123 eV.

2.5 Reflectance spectroscopy

For the reflectance spectroscopy, a TerraSpec spectrometer from ASD Inc. was used, whose spectral range includes the visible light (VIS), the near infrared (NIR) and short-wavelength infrared (SWIR) sections of the electromagnetic spectra (350-2500 nm)(ASD Inc. 2012). If possible, the measurement took place directly on the drill core, in which a broken rough surface showed better results, than a sawn smooth surface. For the breccias, matrix dominated areas were selected. If the conservation of the core was too bad, the grain size smaller 2 mm was separated and used as loose dried sample for the measurements. This treatment has no influence on the position of the detected features in the spectrum and their relative size. Due to the similarity of several reflectance spectra, these were summarized to groups, in which only the average graph was evaluated.

3. Lithological description

The examined part of the drill core SES-1 is located from 240 m to 273 m of depth and was only logged during the drilling process. In this part, the core is 10 cm in diameter and mostly in a well-preserved state. Three main lithotypes can be distinguished clearly that comprise porphyritic rocks (Fig. 5), breccias (Fig. 6) and carbonatite veins (alvikites) (Fig. 7), which are described below. A detailed drill log can be found in the annex and in figure 8.

3.1 Porphyritic rock

The porphyries (Plagiogranitporphyr) have a fine to medium grained porphyritic texture and contain some quartz and feldspar phenocrysts (Fig. 5 A,B), which can have a size up to 5 mm in diameter.

This lithotype shows no reaction with diluted hydrochloric acid (10 %). The colour is varying from yellow-beige to reddish colours and there is a pronounced zonation in some areas, especially around joints and a carbonatitic vein at a depth of 244 m.

In the sections dominated by porphyry rock are well preserved and only fractured by joints. These joints occur irregularly as single joint or as joint sets without extend into other lithotypes. Thus, the porphyries can be regarded as the oldest unit. In some cases, there is talc in the joints, on which slickensides can be found (Fig. 5 C). The porphyries can be interpreted as wall rock.

3.2 Igneous breccia

The breccias have the biggest macroscopic variability among the lithotypes. Over the whole examined core section, there is one breccia body from 252.5 m to 265.6 m depth, which is penetrated by several carbonatite (alvikite) veins.

The breccias have a fine- to cryptocrystalline matrix, which has a very large colour variability from dark red (Fig. 6 C,E) to beige (Fig. 6 B,D) to greyish (Fig. 6 A) colours. The colour gradient from red to beige is particularly pronounced at the border to carbonatite veins. The matrix shows, with the exception of the greyish coloured matrix, no reaction with hydrochloric acid. In these greyish areas, a very light reaction with hydrochloric acid can be observed.

The clasts have a size range from a few millimetres to tens of centimetres in diameter. They consist mostly of the wall rock lithotypes, in particular subangular fragments of porphyries. Other clasts, such as black shale, occur occasionally, which appear more rounded.

The clast-to-matrix ratio varies widely, allowing the distinction between breccias with abundant clasts, which have a clast supported texture and breccias with a minor portion of clasts, where the texture is matrix based.

The preservation of the core sections is very different and generally more disturbed than in the other occurring lithotypes within the drill core section. In some areas the core is partly well preserved so that the rock structure is still recognizable while in other areas the rock fabric is completely disintegrated. The rock properties of the breccias indicate an igneous origin developed by intrusion-related fracturing.

The origin of the igneous breccias of the Storkwitz carbonatite complex has been the subject of considerable debate for some time. Proposed interpretations include an origin as an intrusive breccia as well as a diatreme breccia (pers. communication M. Fiedler, M. Lapp).

3.3 Alvikite

The occurring alvikite veins in the section of the drill core penetrate the porphyries as well as the breccias and can be regarded youngest lithological unit. They have a thickness range from a few centimetres to a few metres and the overlap of veins indicate, that they belong to different generations.

The alvikites have a finely crystalline matrix, which is of greyish (Fig. 7 A,B), brownish (Fig. 7 D) to reddish (Fig. 7 C,E) colouring and show black magnetite and phlogopite crystals in the lower millimetre range. In the carbonatites, different textures can be identified ranging from areas with a mostly homogeneous matrix to heterogeneous areas. There are calcitic streaks, pure calcite veins which have a thickness of a few centimetres, heterogeneous areas with an accumulation of phenocrysts and areas with a clayey matrix that may indicate alteration. Carbonatite xenoliths, which can be up to 5 cm thick, can be found in some veins.

The alvikite sections shows a very strong reaction with hydrochloric acid. The core is mostly well preserved in these sections and only in some areas fragmented. The fragments are large enough, to reproduce the rock fabric.

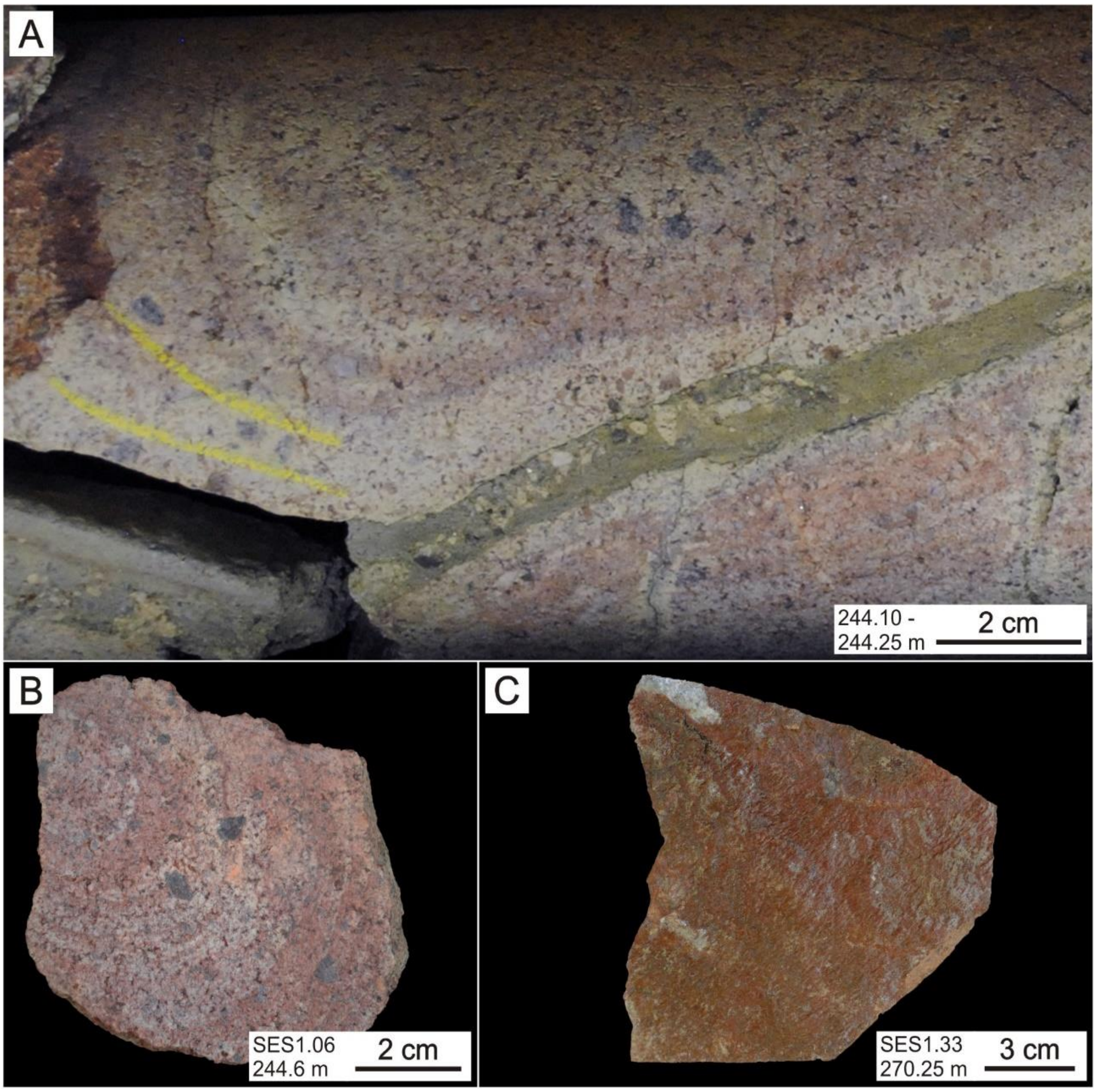

Figure 5: Porphyry of the "Plagiogranitporphyr"; A: Drill core section with an alvikite vein; B: Porphyry with spherical zoned colouring; C: Joint, filled with talc, with slickensides.

Abbildung 5: Porphyr des “Plagiogranitporphyrs”; A: Bohrkernabschnitt mit Alvikitader; B: Porphyr mit sphärischer Farbzonierung; C: Kluftfläche mit Talk und Harnischen

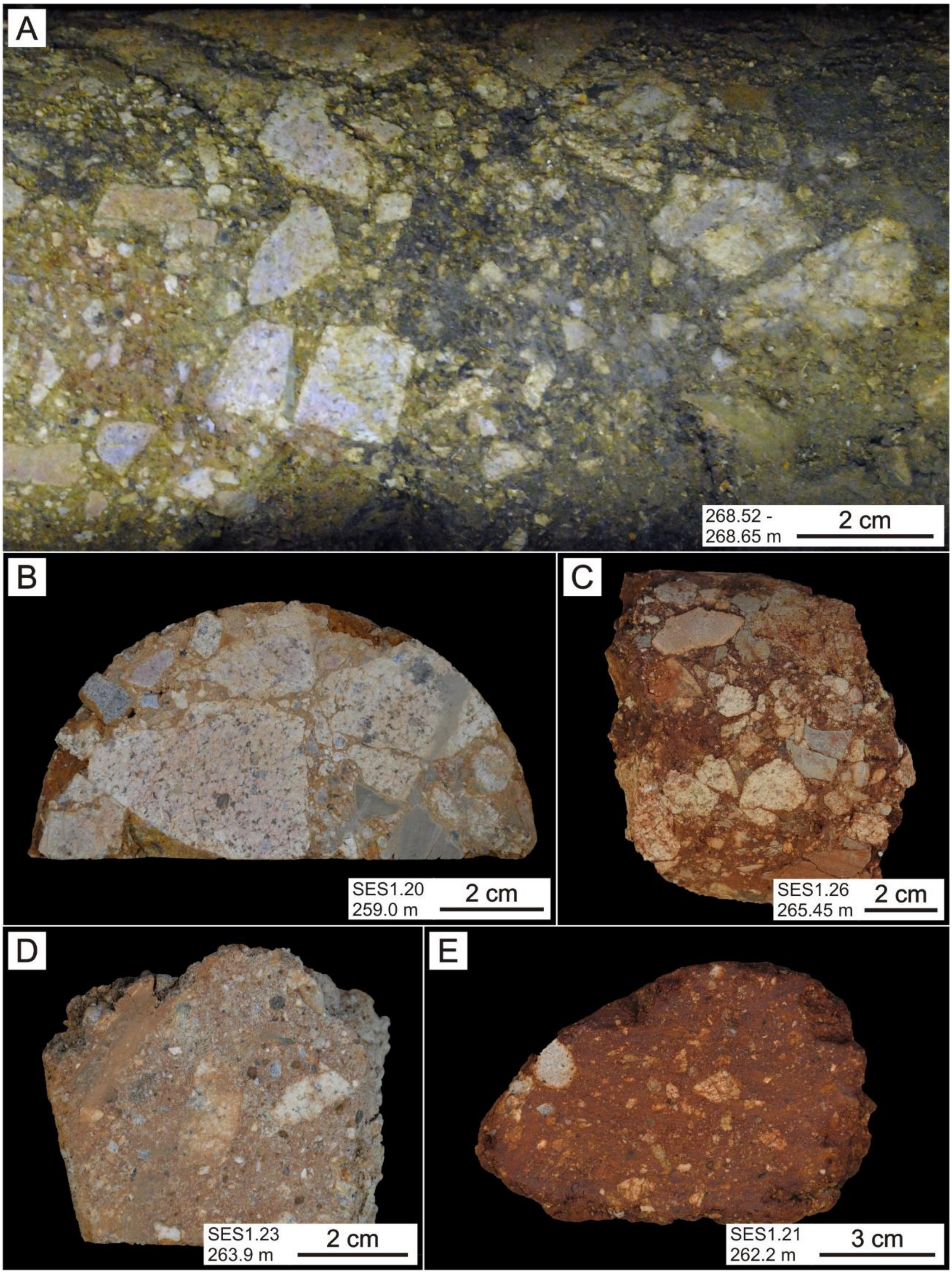

Figure 6: Igneous breccia samples; A: Clast-rich breccia with grey to beige matrix; B: Clast-rich breccia with beige matrix, C: Clast-rich breccia with red matrix, D: Breccia with minor clasts with beige matrix, E: Breccia with minor clasts with red matrix (wet surface).

Abbildung 6: Magmatische Brekzie; A: Klastendominierte Brekzie mit grauer bis beiger Matrix; B: Klastendominierte Brekzie mit beiger Matrix, C: Klastendominierte Brekzie mit roter Matrix; D: Klastenarme Brekzie mit beiger Matrix; E: Klastenarme Brekzie mit roter Matrix (feuchte Oberfläche)

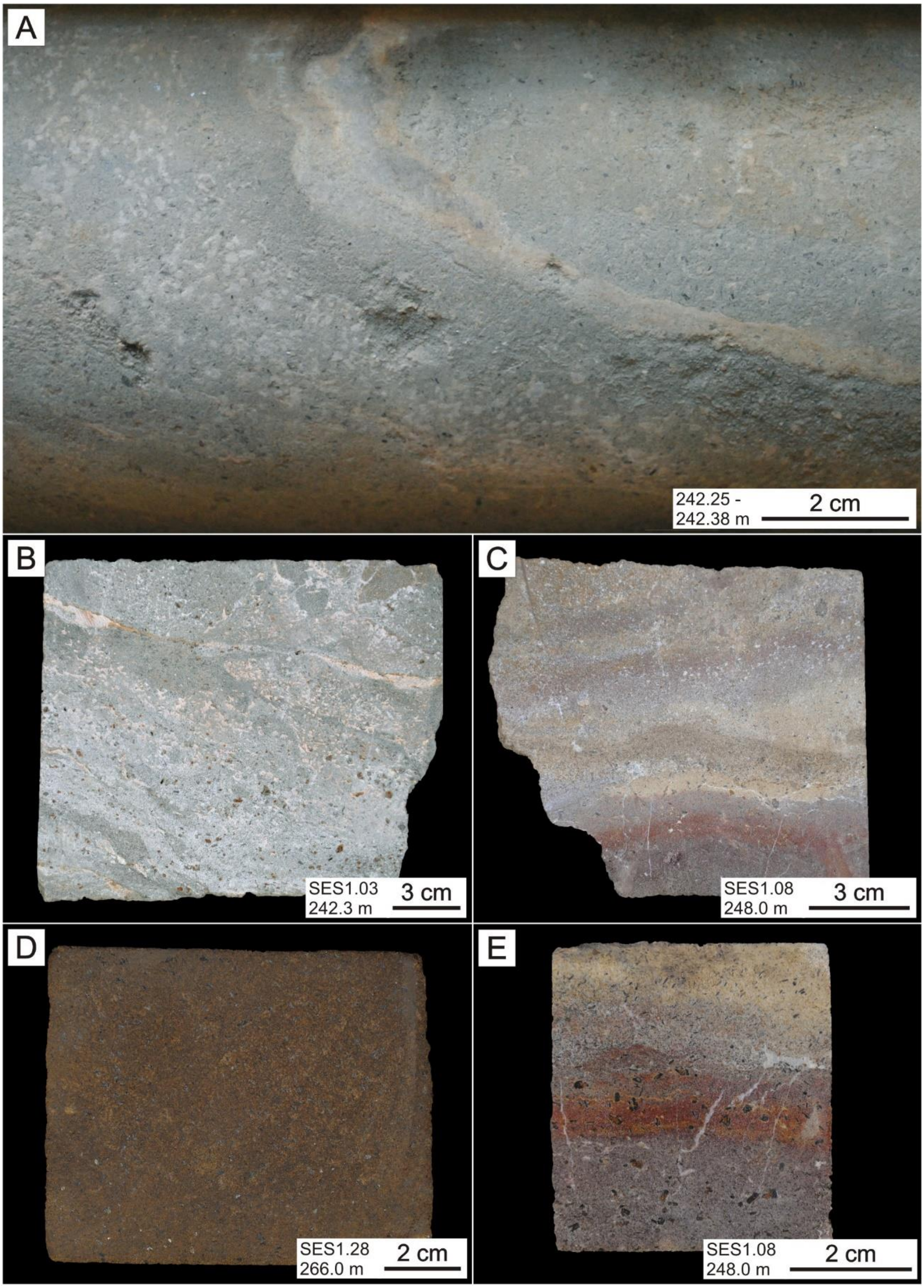

Figure 7: Alvikite samples; A: Drill core section with greyish blue matrix; B Alvikite with greyish blue matrix, with brown phlogopites and calcitic streaks; C: Zoned alvikite; with reddish zone; D: Alvikite with brownish matrix (wet surface); E: Zoned alvikite; with reddish zone (wet surface).

Abbildung 7: Alvikit Handstücke; A: Bohrkernabschnitt mit gräulich-blauer Matrix; B: Alvikit mit gräulich blauer Matrix, braunen Phlogopiten und calcitischen Schlieren; C: Alvikit mit Farbzonierung; D: Alvikit mit bräunlicher Matrix (feuchte Oberfläche); E: Alvikit mit Farbzonierung (feuchte Oberfläche)

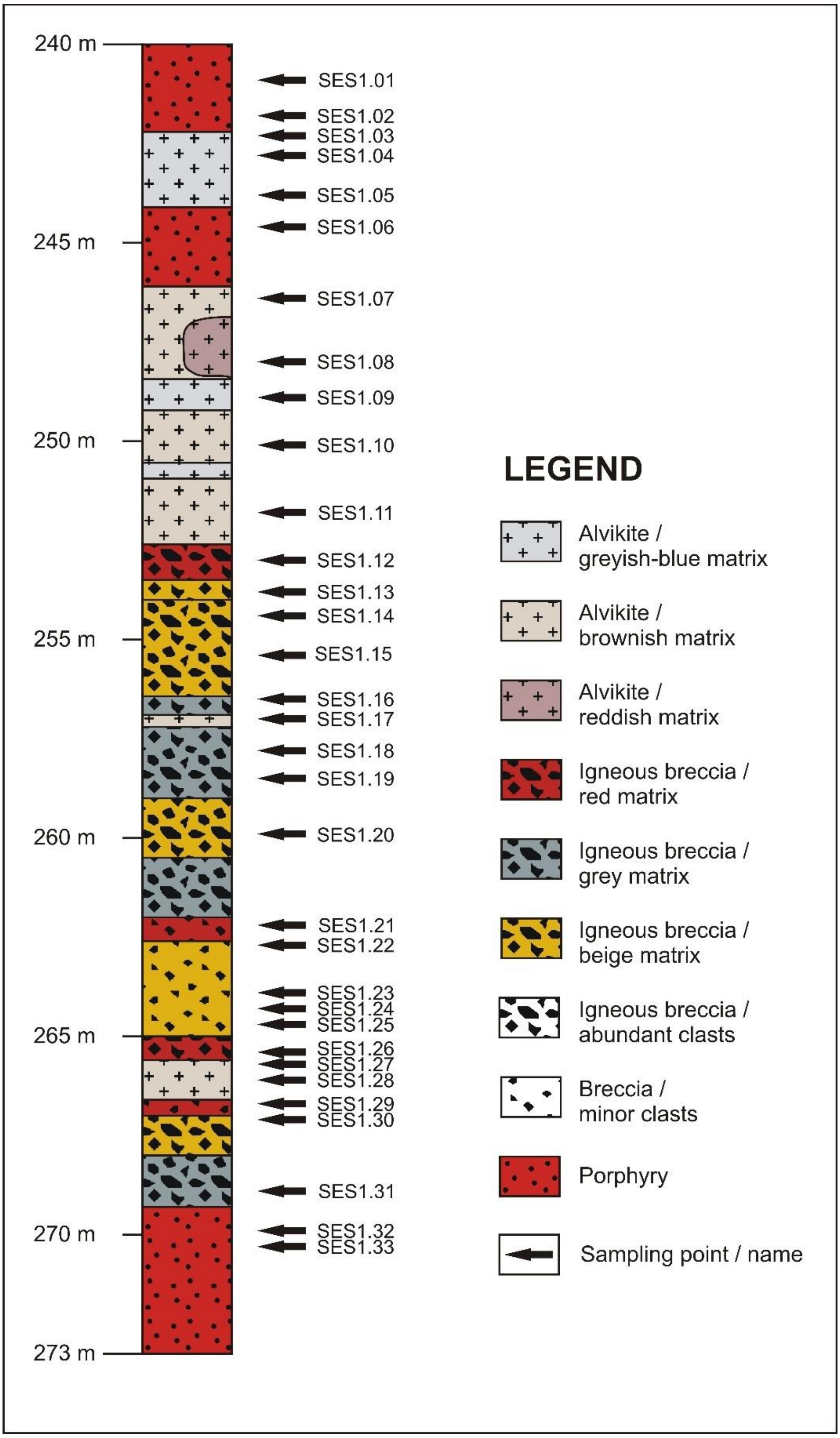

Figure 8: Core log with the position of the taken samples for geochemistry and thin sections. From the samples 14, 15 and 25 no thin section could be made.

Abbildung 8: Bohrlog mit der Position der für Geochemie und zur Dünnschliffherstellung entnommenen Proben. Aus den Proben 14, 15 und 25 konnten keine Dünnschliffe hergestellt werden.

4. Magnetic susceptibility

With the susceptibility logging, the three major lithotypes can be identified and clearly distinguished. For better comparability, all results are converted in the SI Unit system (Tab. 4). While the porphyritic wall rock has a very low susceptibility, the alvikites have on average 1000 times higher values which is most likely caused by magnetite. The susceptibility of the breccias lies between the other two lithotypes, whereby some parts with a red matrix in the breccia section exist, where an increased susceptibility could be measured. This can be an indication of hematite as a major iron phase in the matrix, which has a higher susceptibility than goethite.

The detailed measurement between 240.0 m and 240.4 m depth shows, that the transition between the lithotypes is very sharp (Fig. 9). The complete log of the drill core section is shown in figure 10 and the complete dataset can be found on the enclosed CD.

Table 4: Average measured magnetic susceptibility of the main lithotypes.

Tabelle 4: Durchscnittlich gemessene magnetische Suszeptibilität der Hauptlithotypen

Lithotype	**Measured points**	**Average** [10^{-6}(SI)]	**Std. deviation** [10^{-6} (SI)]
Porphyry	103	37	26
Alvikite	215	35.496	13.684
Breccia	93	575	1.073
Breccia without values >1000	87	346	156

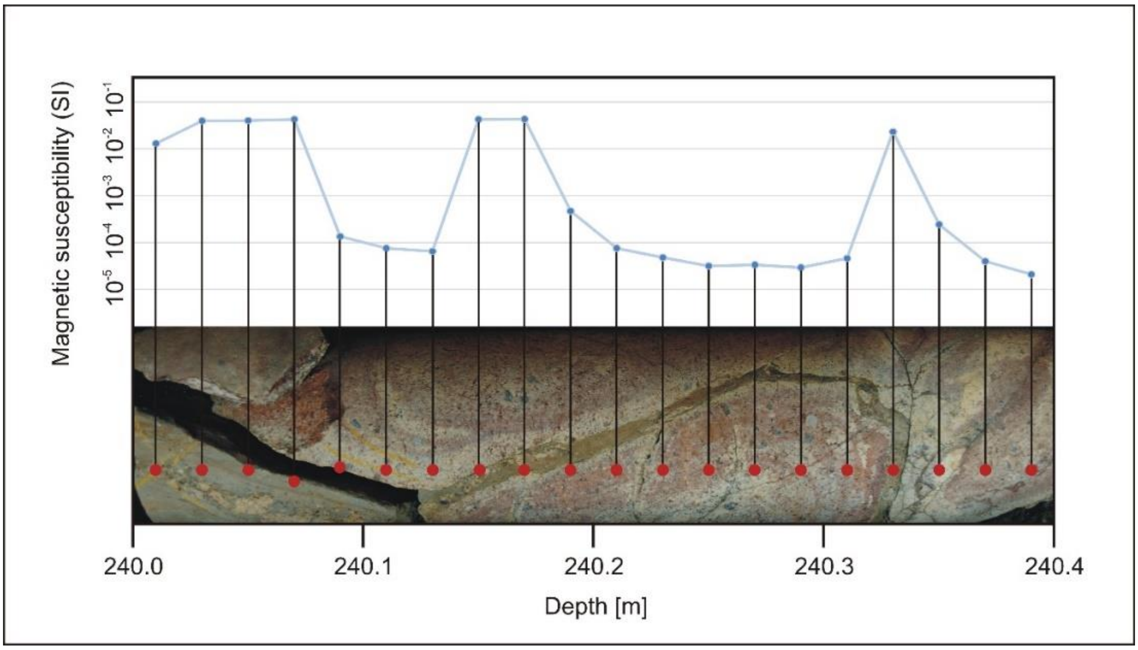

Figure 9: Detailed measurement of a core section with an alvikite (left side) and a porphyritic rock, which is penetrated by an alvikite vein. The lithotypes can be distinguished very clearly.

Abbildung 9: Detaillierte Suszeptibilitätsmessungen an einem Bohrkernabschnitt mit Übergang von Alvikit zum Porphyr, welcher durch eine weitere kleine Alvikitader penetriert wird. Die verschiedenen Lithotypen können klar und scharf unterschieden werden.

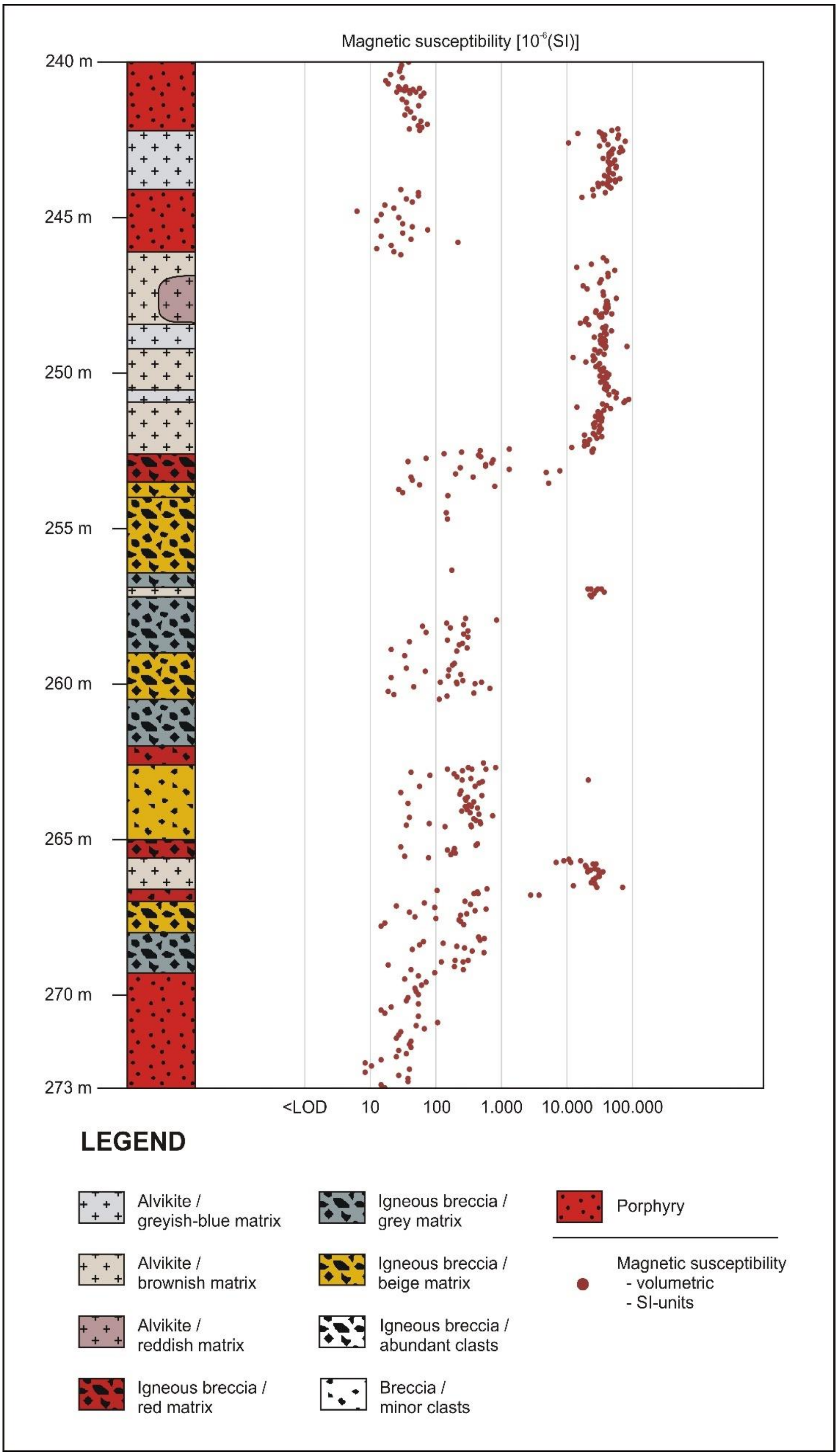

Figure 10: Magnetic susceptibility core log; the different lithotypes can be distinguished clearly.

Abbildung 10: Bohrlog der magnetischen Suszteptibilität. Die verschiedenen Lithotypen können eindeutig unterschieden werden.

5. Geochemistry

In this chapter, all results of the portable XRF and certified whole rock analysis are summarized. All percent or ppm values in this chapter refer to mass concentration, if not described different.

5.1 Portable XRF

The portable XRF analysis enables to create detailed loggings for some elements like lanthanum, cerium, niobium, iron, or zirconium. Although this measurement cannot be used to get precise quantitative data, the values correlate very well with the results of the certified whole rock analysis. Different lithotypes can be identified and distinguished clearly according the reading log of the REE lanthanum and cerium (Fig. 11). While the breccias have the biggest variation of values, the measurements of the porphyries and alvikites show consistent values for the majority of the logged elements.

It has been shown, that the REE-mineralisation occurs predominantly in alvikite veins and in the matrix of the igneous breccias, while the clasts of the breccias and the porphyry sections contain no indication for a REE-mineralisation. In these mineralised sections, also the highest values of niobium, zirconium and yttrium occur and seem to be associated to the REE-mineralisation. However, the high variability of values for the concentration of the REE and associated elements is in general higher in the matrix of the breccias, compared to the alvikites.

The contents of barium and strontium show noteworthy variations with the highest values in the alvikite section between 246.1 m and 252.5 m (Fig. 12). This is remarkable, because these elements are correlating with each other but not to any other geochemical or macroscopic logging. Except for these very high values, barium and strontium also occur predominantly in the alvikites and the matrix of the breccias. The highest values for iron were detected in the matrix of the breccias, especially in sections with red matrix. Furthermore, some porphyry sections have also increased amounts of iron.

The loggings for iron, yttrium, niobium and zirconium can be found in the annex.

5.2 Whole rock analyses

With the results of the whole rock analysis, the three main lithotypes can be clearly distinguished by a couple of element concentrations and element associations, for example by calcium and silicon (Fig. 13). A table with all results of the analysis can be taken from the annex. A main outcome is, that the geochemical lab analyses confirm the portable XRF measurements. As already measured with the portable XRF, the igneous breccia is the lithotype with the biggest variability of the geochemical composition, in which especially iron concentration is varying in a wide range. The difference of the barium concentration is bigger in the alvikite samples, than in the other lithotypes, which was also prior analysed by portable XRF. Furthermore, the REE and the associated elements occur predominantly in the breccia and alvikite samples, while the grade is in general higher in the breccias. Due to the variation of the matrix/clast ratio of the breccia samples, it is only possible, to deduce general geochemical statements seriously. For some elements, like the REE, the link between content and amount of clasts is clearly visible, which indicates, that these elements only occur in the matrix. For other elements like barium, this correlation is not so clear (Fig. 14).

In addition with data from older drillings of the UML-CR Delitzsch, two different types of intrusive breccias (with and without lamprophyric clasts) can be defined and are illustrated in a REE-Ti-Ni/Cr ternary plot (RÖLLIG et al. 1990). A comparison with this old plot shows, that there are no lamprophyric xenoliths in the breccias. The same can be assumed for the alvikite veins, although this is a comparison of two different rock types (Fig. 15).

5.2.1 Major components

The porphyry sections contain 70 % silicon oxide (**SiO_2**), 15 % alumina oxide (**Al_2O_3**) and 7,5 % alkali metal oxides (**Na_2O** + **K_2O**), which is a typical composition for felsic igneous rocks (LE MAITRE et al. 2002). In the TAS diagram (Fig. 16), all samples are situated in the granite field. The amounts of total iron oxide (**Fe_2O_3**) are varying between 1 % and 3 % and there is no influence of the colour of the samples to the concentration of iron.

Comparing the samples from the mineralised section, the alvikites have a lower variability in their geochemical composition than the breccia samples. Their main oxide is calcium oxide (**CaO**), which is up to 48 % in the samples. (56 % would be the highest possible amount, if the sample would consist of 100 % calcite.) Silicon and iron oxides (**SiO_2** and **Fe_2O_3**) are included with less than 13 % and magnesium oxide (**MgO**) with less than 8 %. After classification by main oxides (WOOLLEY & KEMPE 1989), the sample data plot in the fields of the calciocarbonatite and the ferrocarbonatite (Fig. 17). Based on SEM-EDX analyses, which showed, that calcite is the only existing matrix forming carbonate in these samples and that iron is predominantly bound in magnetite, phlogopite and cryptocrystalline iron phases, calciocarbonatite or alvikite can be applied for the classification

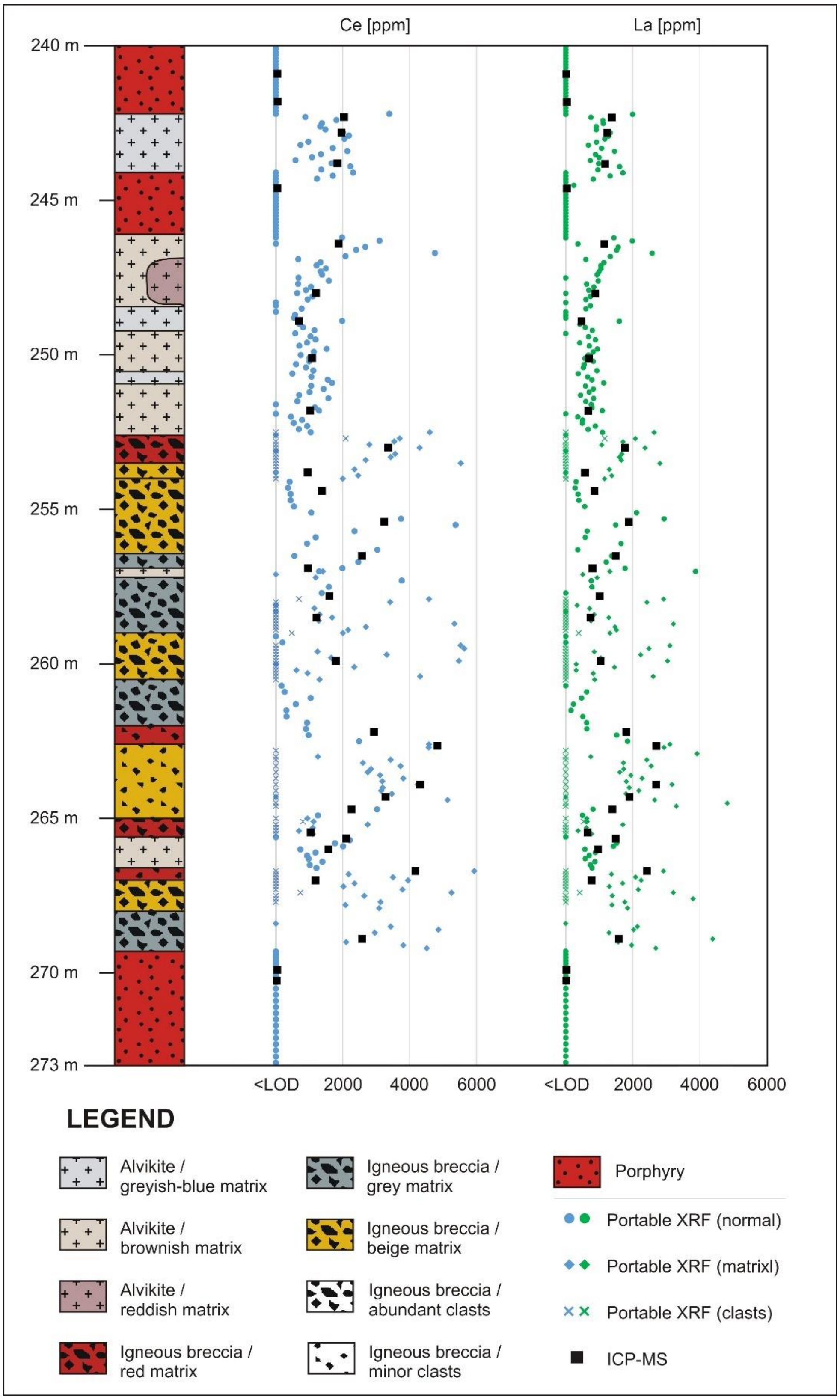

Figure 11: Portable XRF reading of the La and Ce concentrations in comparison with ICP-MS whole rock analysis. Portable XRF data are presented separate for matrix and clasts in the breccia sections.

Abbildung 11: Ergebnisse der portablen RFA-Messungen für La und Ce im Vergleich mit der ICP-MS Gesamtgesteinsanalyse. In den Brekzien-Bereichen sind die portablen RFA Werte in Klasten und Matrix unterteilt.

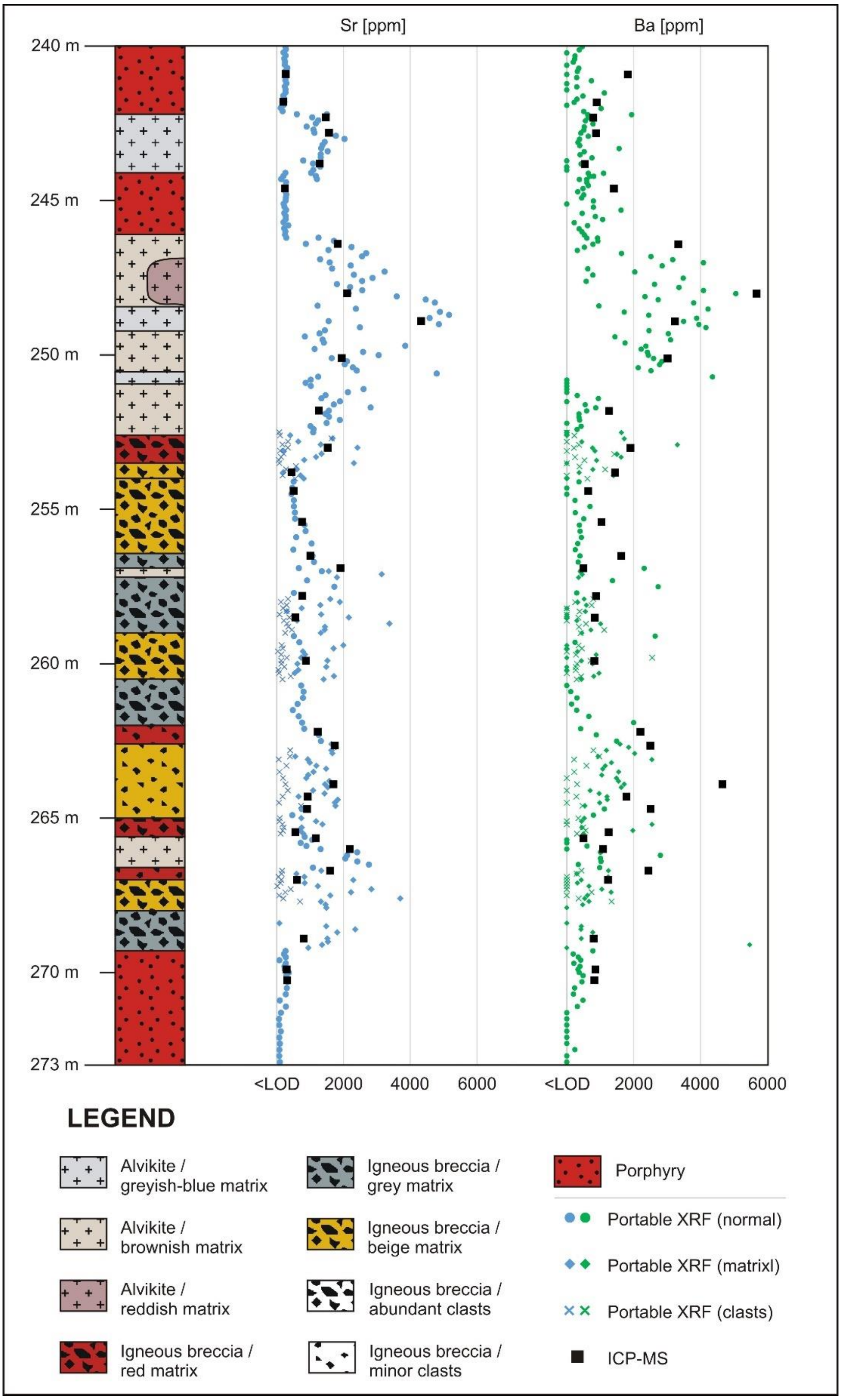

Figure 12: Portable XRF reading of the Sr and Ba concentrations in comparison with ICP-MS whole rock analysis. Portable XRF data are presented separate for matrix and clasts in the breccia sections.

Abbildung 12: Ergebnisse der portablen RFA-Messungen für Ba und Sr im Vergleich mit der ICP-MS Gesamtgesteinsanalyse. In den Brekzien-Bereichen sind die portablen RFA Werte in Klasten und Matrix unterteilt.

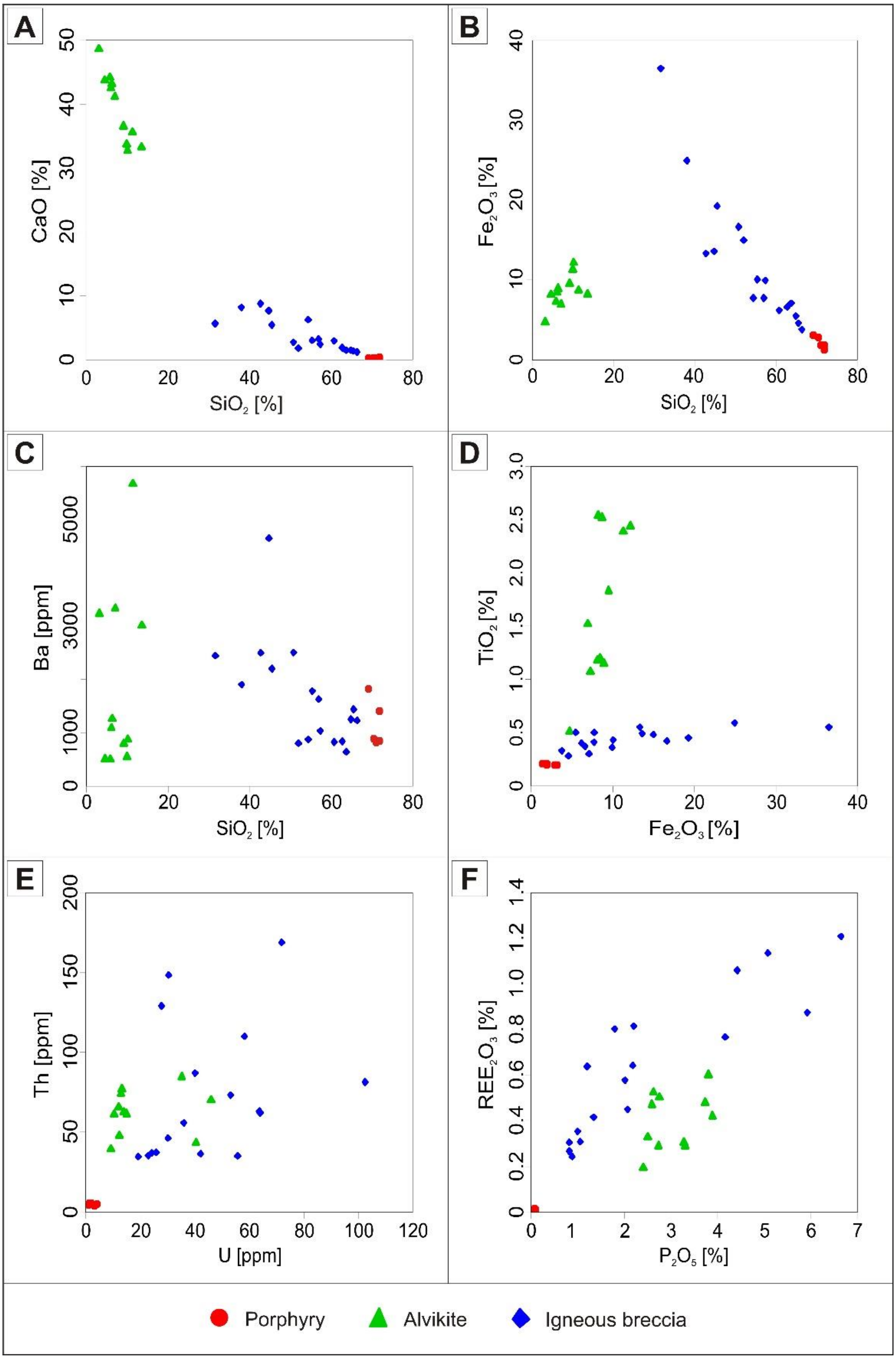

Figure 13: Binary plots of geochemical data; the three main lithotypes can be clearly distinguished by the main oxides.

Abbildung 13: Binäre Diagramme der geochemischen Daten. Die drei Hauptgesteinstypen können eindeutig mit den Hauptoxiden unterschieden werden.

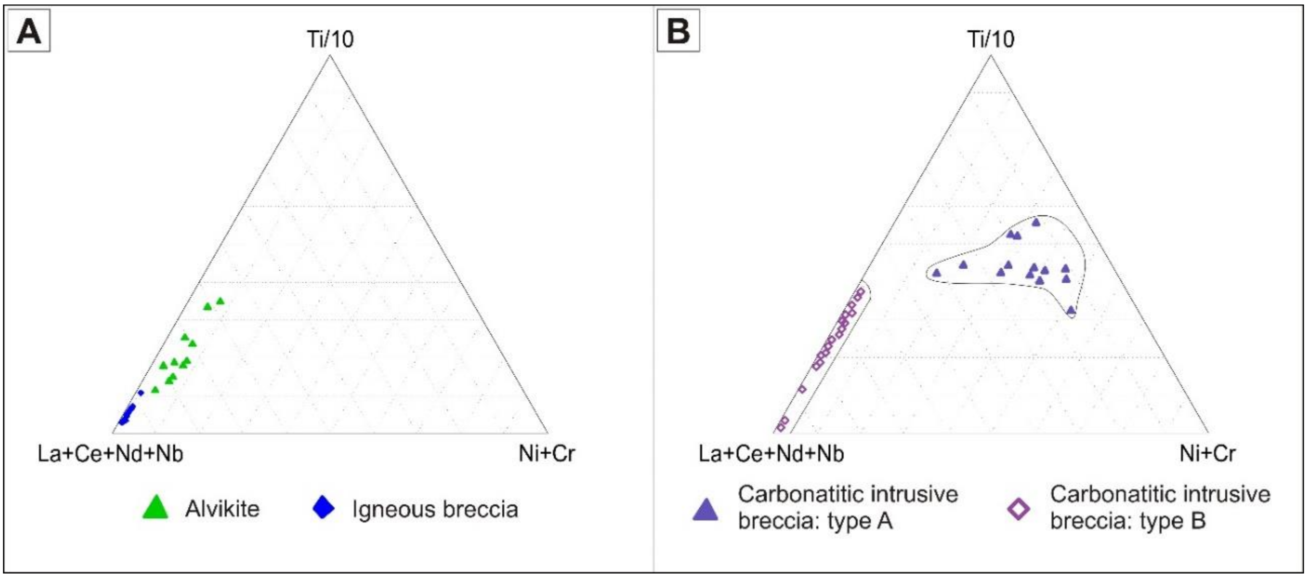

Figure 14: Ternary plots to categorize the samples; A: samples from the actual geochemical analysis; B: Breccia samples from older drilling from the UML-CR, type A are samples with lamprophyric xenoliths and type B samples without these xenoliths (RÖLLIG et al. 1990).

Abbildung 14: Ternäre Diagramme zur Kategorisierung der Proben; A: Proben der aktuellen geochemischen Analyse; B: Brekzienproben von älteren Bohrungen durch den UML-CR; Typ A sind Brekzien mit lamprophyrischen Xenolithen und bei Typ B fehlen diese (RÖLLIG et al. 1990)

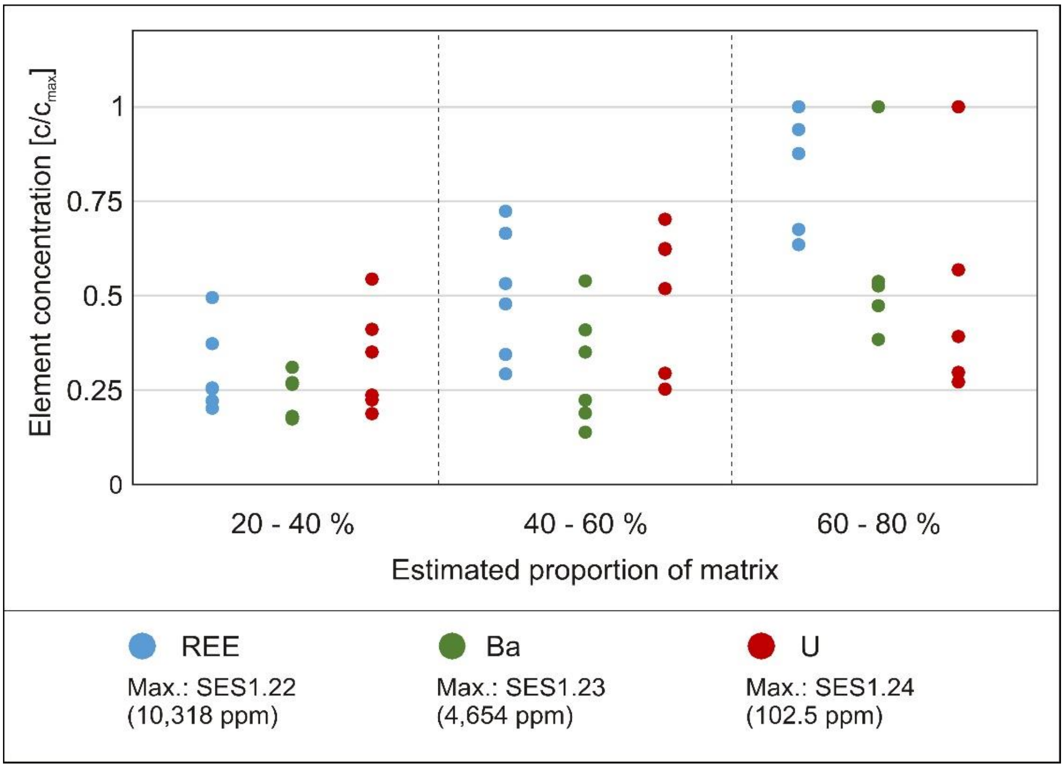

Figure 15: Link between the content of REE, Ba and U and the proportion of matrix in the breccia samples. For the REE, there is a correlatoin recognizable.

Abbildung 15: Verknüpfung zwischen dem Gehalt an REE, Ba und U und dem Anteil der Matrix an der Brekzienprobe. Für die REE ist eine Korrelation erkennbar.

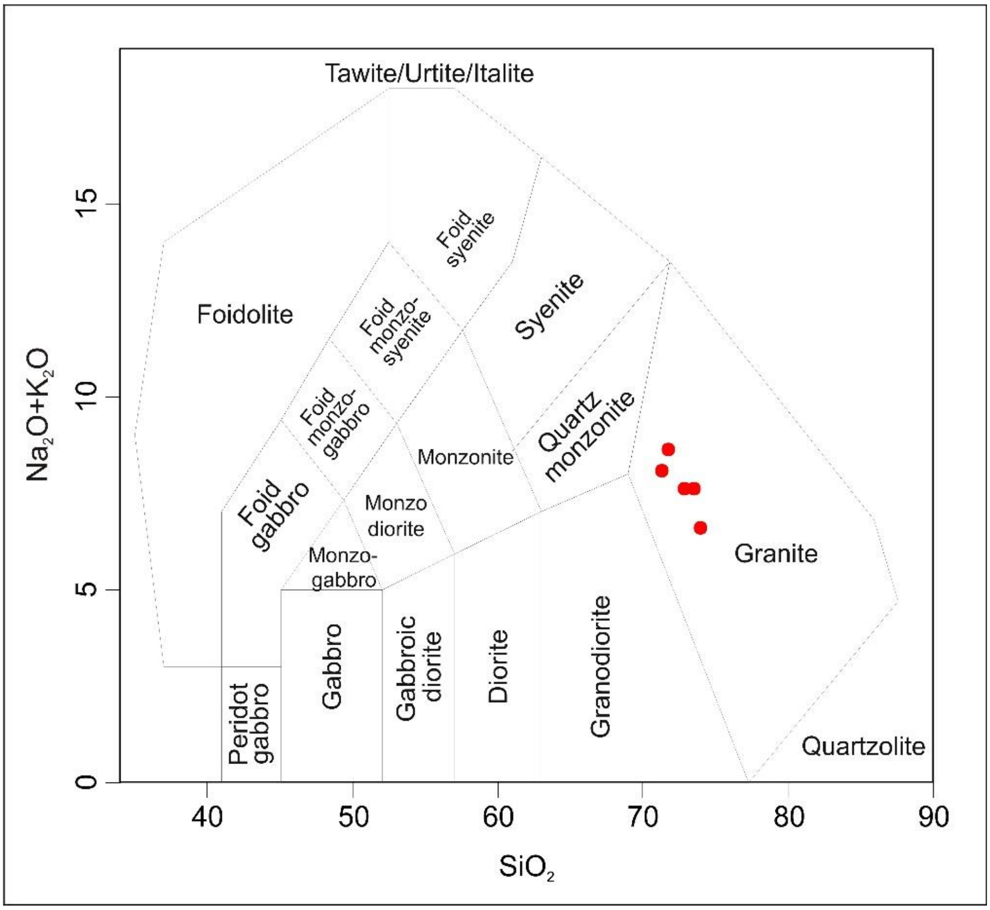

Figure 16: TAS-Diagram for volcanic rocks (after Le Maitre et al. 2002); the porphyry samples (red dots) plot in the granite field.

Abbildung 16: TAS Diagramm für Vulkanite (nach Le Maitre et al. 2002); Die porphyrischen Proben (rote Punkte) plotten in das Granitfeld.

The geochemical characterization of the igneous breccias is more complex, compared to other lithotypes. Generally, the breccias consist of two main components of varying ratio of clasts and matrix. Accordingly, breccia samples have the biggest variation of all lithotypes.

The amount of silicon oxide (**SiO_2**) for example, which is mainly bound in the clasts, has a range from 30 % to 70 % in the samples. Although the breccia is part of a carbonatitic intrusion, there is a comparatively small proportion of calcium oxide (**CaO**), which is less than 4 % in average and obviously not linked to the colour of the matrix. The amount of total iron oxide (**Fe_2O_3**) is the highest of the three lithotypes and especially in the breccias with a red matrix, in which the iron content is increased up to 40 %. Sample SES1.26 (breccia with red matrix) is an exception, because it is extremely clast dominated.

5.2.2 Trace elements

In regards to other trace elements, especially the amounts of strontium, niobium, yttrium, thorium and uranium they are 10 to 100 times higher than values for the upper continental crust. Zirconium and barium are also slightly increased. Furthermore, rubidium occurs to much lower amounts in the alvikite than in the breccia samples (Fig. 18). The chondrite data from (McDonough & Sun 1995) was used as a reference for the trace elements.

5.2.3 Rare earth elements

The concentration of the REE oxides (**REE_2O_3**) is 6397 ppm in average in the breccia samples and 4007 ppm in average in the alvikite samples. The concentration of the light rare earth elements (LREE) is much higher than the concentration of the heavy rare earth elements (HREE) (Tab. 5). The amount of lanthanum and cerium is approximately 65-75 % of all REE and if adding neodymium, then the amount rises to 80 – 90 % (Tab. 6) (Fig. 19). This is typical for carbonatitic intrusions, which have the highest amount of REE and the highest enrichment of LREE in comparison to HREE of all igneous rocks (Cullers & Graf 1984). In all samples, the Oddo-Harkins-rule is valid for the REE (expect the radioactive promethium), so that cerium (Z=58) is the most abundant REE and has higher amounts than lanthanum (Z=57) or praseodymium (Z=59).

Compared to chondrites, the amount of the LREE in the mineralised section is up to 5000 times higher and the amount of HREE up to 500 times higher (Fig. 20). The distribution of the REEs is nearly the same in the breccia and alvikite sections. There is no europium or cerium anomaly. The distributions of REEs in the porphyry is nearly the same, but with a small negative europium anomaly and some variation at the HREE, which can be caused by the small total amounts of 13 ppm for all HREE in average. Compared to the upper continental crust the LREE have higher amounts, than the HREE. The Porphyry has a little bit lower amounts of REE than the upper continental crust while it is up to 50 times higher in the mineralised sections. As reference for the REE, the chondrite data from Boynton (1984) was used.

5.3 Comparison with deeper sections

Geochemical data from deeper sections of the same drill core were used basically for comparison. This geochemical dataset was provided by the Ceritech AG and represents an excerpt from the official exploration report (Reichert et al. 2015).

According to this dataset, the drill core penetrates the main intrusive breccia body of Storkwitz from 371 - 617 m depth. Further, the breccia body can be divided in an outer zone, where the breccia contains abundant clasts and an inner zone from 436 m - 529 m depth, where the breccia is free of clasts (Reichert et al. 2015). As in the section investigated in this study, alvikite veins occur as well in deeper levels of the drill core, which penetrate the breccia body. In order to compare both depth intervals, the average chemical composition of the several units is used. The inner breccia zone is considered to define reference values, because it can be assumed, that this breccia is associated with the intrusion stage, and thus represents the pristine composition (Fig. 21).

Unfortunately, the statistical quality is much lower for the alvikites than for the breccias, because geochemical data from just six alvikite samples are available from the deeper section. These samples originate from two different veins. Nevertheless, there are some significant differences in their composition. The deeper veins contain in average higher amounts of oxides, which can be associated with silicate minerals (**SiO_2**, **Al_2O_3**, **K_2O**, **Na_2O**), while in the upper veins main element oxides have higher concentrations, which can be bound in typical carbonatite minerals like carbonates in general, pyrochlore or apatite (**CaO**, **TiO_2**, **P_2O_5**). Furthermore, the alvikites from deeper levels have higher amounts of rubidium than the samples from the upper drill core area.

The breccia samples contain generally lower amounts of magnesium oxide (**MgO**), calcium oxide (**CaO**), and manganese oxide (**MnO**) than the breccia from the deeper core section. Especially the higher amount of calcium oxide in the deeper sections indicates a calcitic matrix, which is obviously altered in the upper section. The contents of some oxides, which that are typical for silicate minerals, are higher in the upper breccia (**SiO_2**, **Al_2O_3**, **K_2O**), what indicates, that an increased proportion of clasts occur in the upper core section. Rubidium is higher concentrated in the upper breccia section.

The geochemical data in regards to trace elements and REE differ slightly in order to determine deviations with an adequate statistical quality. Consequently, the amount and distribution of REE is obviously not changing with an increasing level of depth.

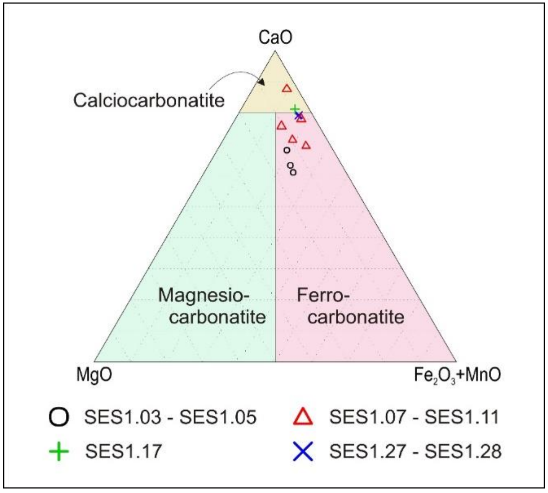

Figure 17: Ternary plot for the classification of the alvikite samples by their proportion of their main oxides CaO, MgO, Fe2O3 and MnO (after Woolley & Kempe 1989)

Abbildung 17: Dreiecksdiagramm zur Klassifizierung der Alvikitproben durch das Verhältnis ihrer Hauptoxide CaO, MgO, Fe2O3 und MnO (nach Woolley & Kempe 1989)

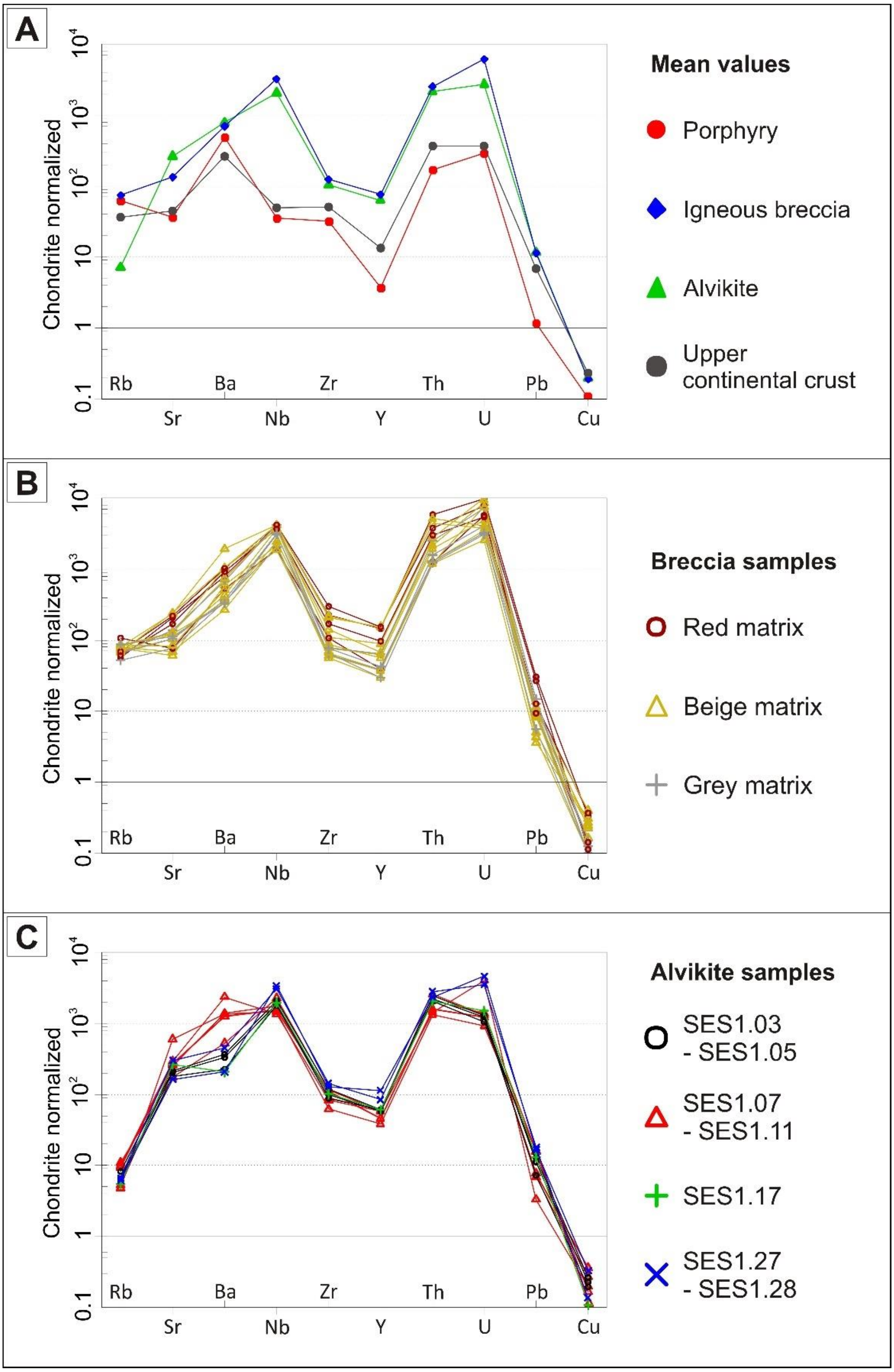

Figure 18: Spider plot showing geochemical data of some trace elements (chondrite normalised after McDonough & Sun 1995); A: Average amounts in the different lithotypes; B: amounts in breccia samples; C: amounts in alvikite samples.

Abbildung 18: Spider-Plot mit den geochemischen Daten einiger Spurenelemente (Chrondrit normalisiert nach McDonough & Sun 1995); A: Durchschnittliche Gehalte in den verschiedenen Lithotypen; B: Gehalte in Brekzienproben; C: Gehalte in Alvikitproben

Table 5: Absolute average concentrations of REE of the three major lithotypes.

Tabelle 5: Absolute durchschnittliche Konzentration von REE in den drei Hauptlithotypen

	$LREE_2O_3$ [ppm]		$HREE_2O_3$ [ppm]		REE_2O_3 [ppm]	
Lithotype	**Average**	**Std. deviation**	**Average**	**Std. deviation**	**Average**	**Std. deviation**
Porphyry	109	26	13	1	122	26
Breccia	6115	2971	282	170	6397	3129
Alvikite	3778	1215	229	74	4007	1266

Table 6: Relative average concentrations of the most common REE of the three major lithotypes.

Tabelle 6: Relative durchschnittliche Konzentration der häufigsten REE in den drei Hauptlithotypen

	(La + Ce) / ∑REE [%]		(La + Ce + Nd) / ∑REE [%]		La/Yb $_{[chondrite\ normalized]}$	
Lithotype	**Average**	**Std. deviation**	**Average**	**Std. deviation**	**Average**	**Std. deviation**
Porphyry	65.6	1.7	81.9	1.7	28.2	7.4
Breccia	73.6	1.6	89.0	1.0	134.4	38.6
Alvikite	72.6	2.7	87.3	1.6	107.6	29.6

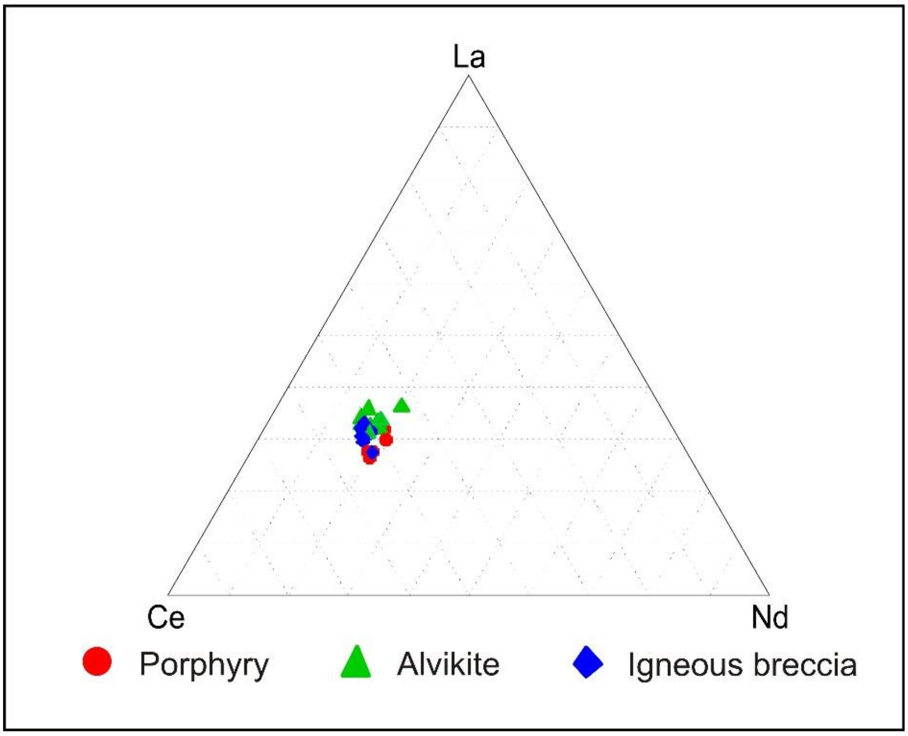

Figure 19: Distribution of the three most common REE (Ce, La, Nd) in various rock types.

Abbildung 19: Verteilung der drei am meisten vorkommenden SEE (Ce, La, Nd) in den einzelnen Geochemieproben

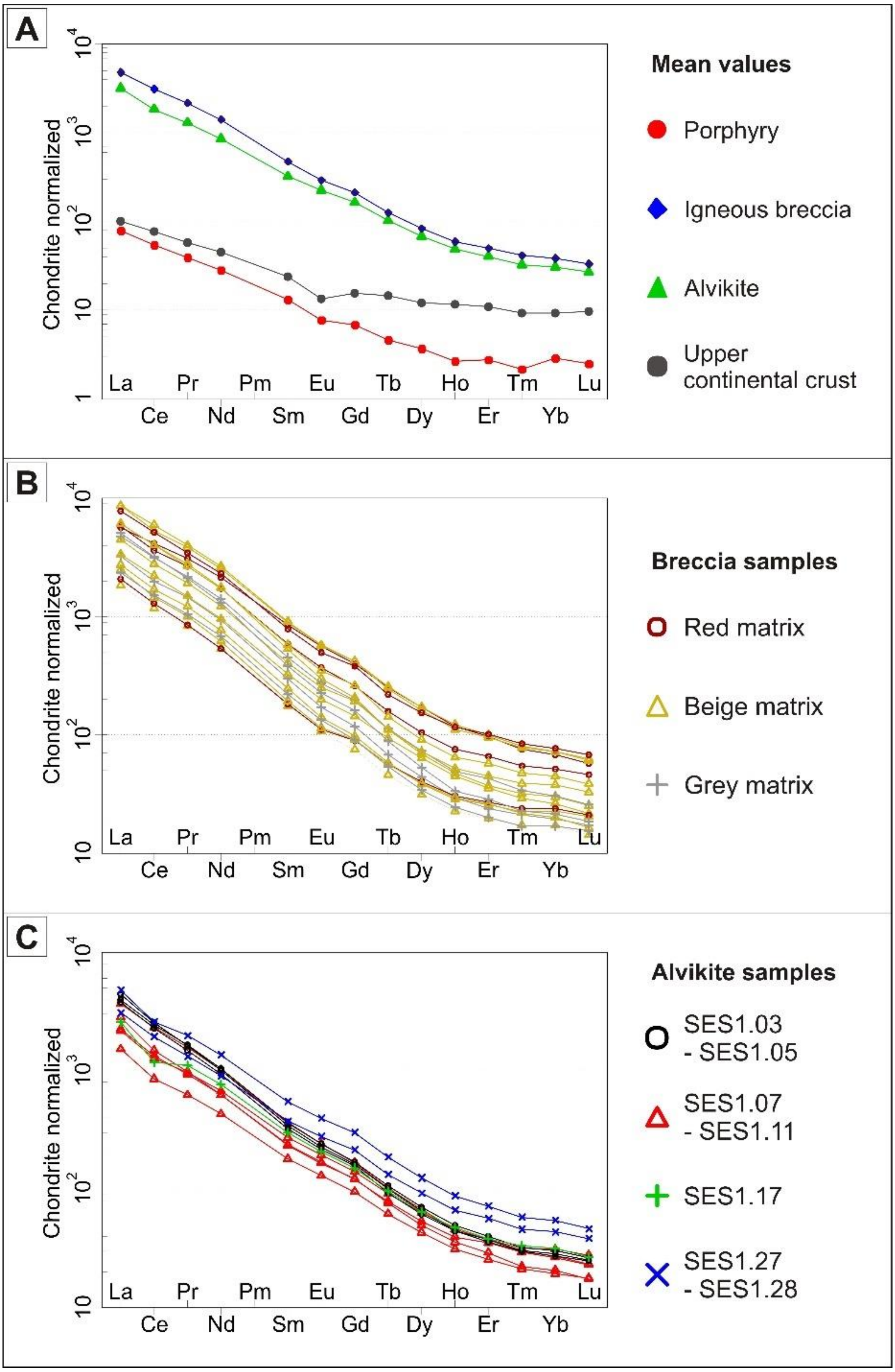

Figure 20: Spider plot showing geochemical data of the REE (Boynton 1984); A: Average concentrations in the different lithotypes; B: concentration in breccia samples; C: concentration in alvikite samples.

Abbildung 20: Spider-Plot mit den geochemischen Daten der SEE. (Chrondrit normalisiert nach Boynton 1984); A: Durchschnittliche Gehalte in den verschiedenen Lithotypen; B: Gehalte in Brekzienproben; C: Gehalte in Alvikitproben

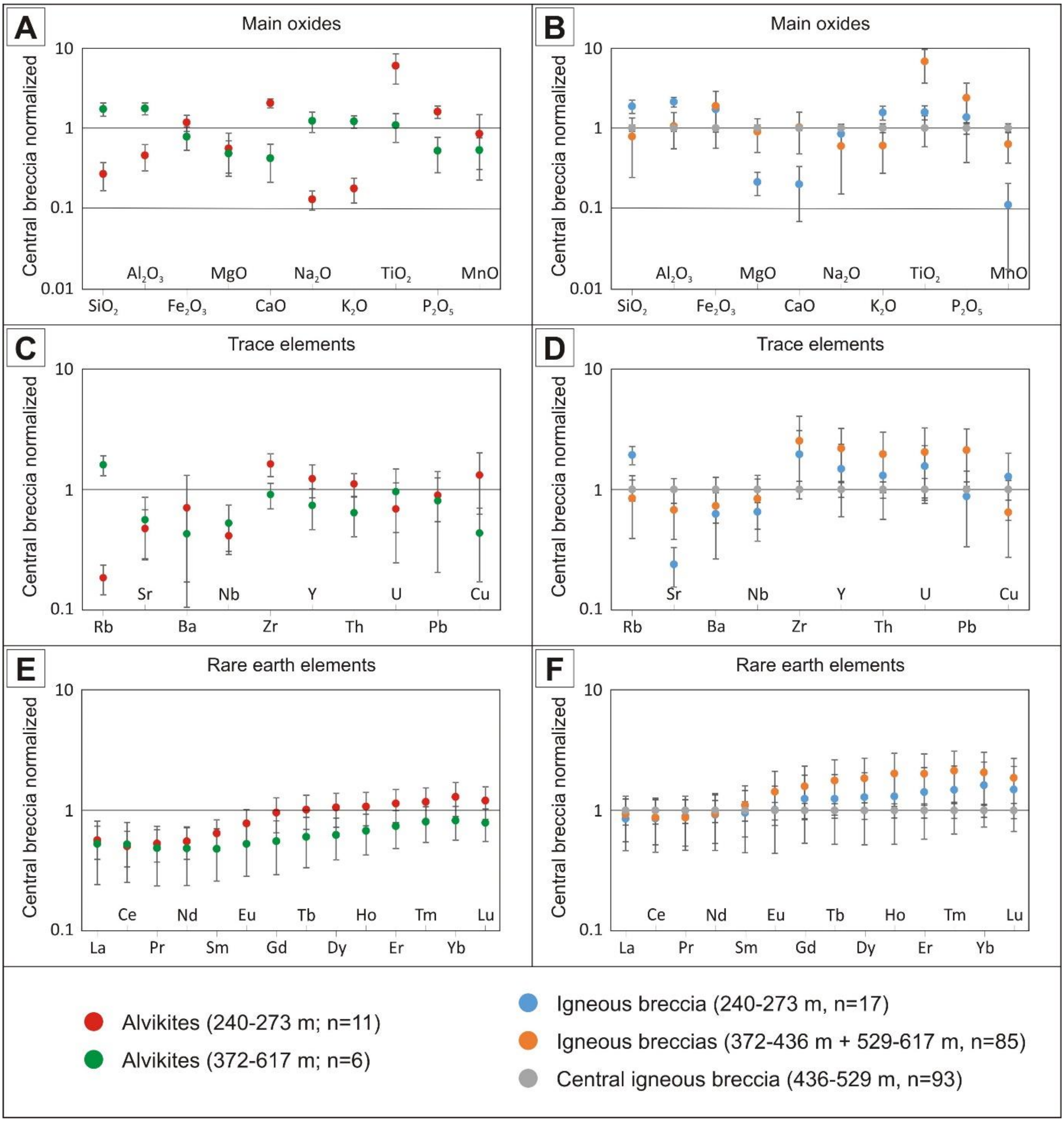

Figure 21: Geochemical comparison from the samples with deeper sections of the same drilling; A,C,E: Comparison of the alvikite sections; B,D,F: Comparison of the breccia sections. There are recognizable differences at some main oxides and rubidium. The contents of REE are similar in the different lithological units.

Abbildung 21: Geochemischer Vergleich der genommenen Proben mit tieferen Bohrkernabschnitten; A,C,E: Vergleich der Alvikitadern; B,D,F: Vergleich der Brekzienproben. Es sind deutliche Unterschiedebei manchen Hauptoxiden und Rubidium feststellbar, während sich die Konzentration an SEE kaum unterscheidet.

6. Mineralogy

6.1 Porphyry

The mineral assemblage of thin sections from the porphyry ("Plagiogranitporphyr") are dominated by silicates. Rock-forming minerals are represented by quartz, sanidine, albite, muscovite and biotite. Zircon, rutile, apatite and monazite occur accessorily. There is a fine-grained quarzitic matrix intergrown with coarse-grained quartz and feldspar mineral phenocrysts, which can be a few millimetres in diameter (Fig. 22 A).

Indication for alteration and secondary minerals are clearly visible. The minerals of the feldspar group, especially the large albite crystals are partially sericitized and the EDX-readings show clearly that the micas are potassium undersaturated. Clay minerals like chlorite indicate secondary alteration. Additionally, the porphyry is penetrated by veins filled with hematite, barite and quartz. Some phenocrysts are fractured by these veins (Fig. 22 B).

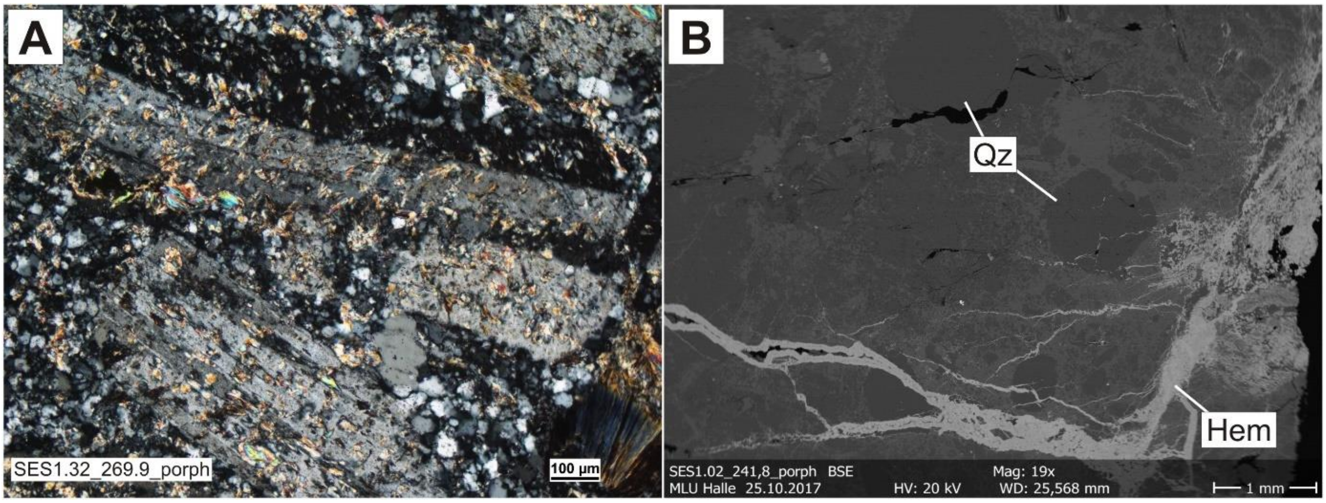

Figure 22: Overview of the porphyry thin sections; A: Sericitized porphyry with quarzitic matrix and feldspar phenocrysts (optical microscopy, crossed nicols); B: Quarzitic matrix with quartz phenocrysts and hematite vein (SEM-BSE).

Abbildung 22: Überblick über die Porphyr Bereiche; A: Serizitisierter Porophyr mit quarzitischer Matrix und Feldspat Einsprenglingen (Durchlichtmikroskopie, gekreuzte Nicols); B: Quarzitische Matrix mit Quarz Einsprenglingen und Hematitader (SEM-BSE)

6.2 Igneous Breccia

The thin sections from the igneous breccias contain, with one exception (SES1.18), no calcitic, but an amorphous to cryptocrystalline alumo-siliceous or ferrous matrix (Fig. 23). Especially breccias with red matrix are ferrous-dominated.

Apatite phenocrysts in the matrix can have a size up to some hundreds of micrometres and are often fractured. Furthermore, the breccia contains up to a few millimetres large phlogopite. Monazite, REE-fluorocarbonates, pyrochlore, baddeleyite and occasional sulphide minerals (pyrite, chalcopyrite, galena) as well as barite occur accessorily. The presence of REE-fluorocarbonates is restricted to breccias with grey matrix. The majority of the rock fragments are made of the surrounding porphyry and contain consequently silicate minerals. Individual quartz or more common feldspar crystals represent phenocrysts from the carbonatitic magma or, more likely, display smaller xenoliths from the surrounding porphyry. These are often fractured with anhedral shape and show partially signs of dissolution at the rims. The thin section of SES1.18 (257.8 m) is a breccia with grey matrix, which is dominated by calcite and goethite. It correlates with the observation, that the grey coloured areas show a low fizzing by testing with hydrochloric acid, which is not observed on the other thin sections with grey matrix. Possibly, the carbonate minerals are distributed heterogeneously. The carbonate minerals are intergrown with large crystals of REE-fluorocarbonates with up to 250 µm size. Macroscopically, this breccia section contains approximately 50 % clasts, but the thin section does not contain any clasts. Consequently, the thin section is not representative for this part of the breccia.

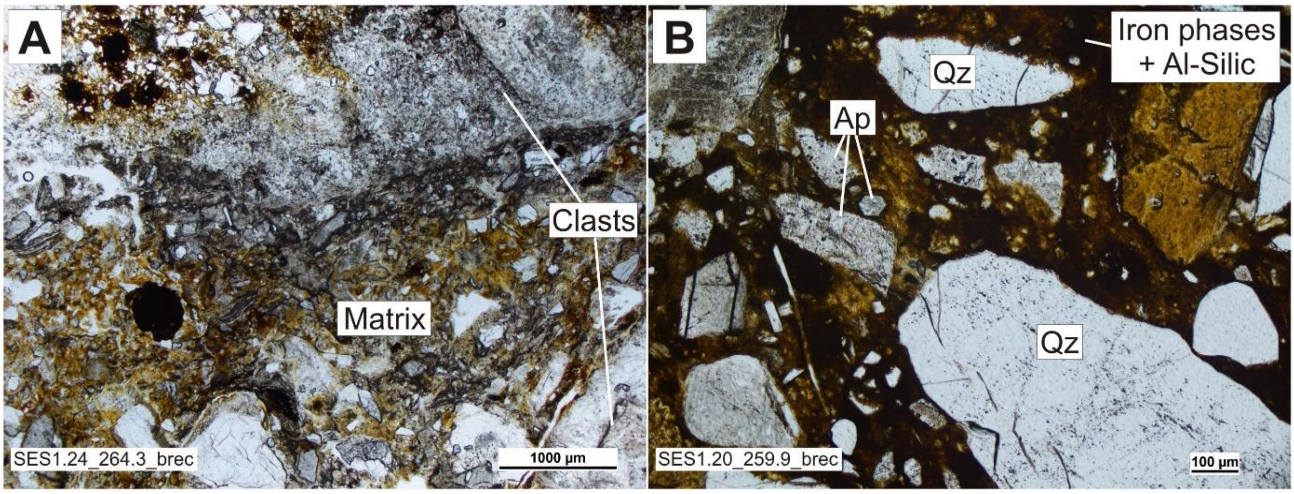

Figure 23: Overview of the igneous breccia thin sections; A: Breccia texture with clasts and matrix (optical microscopy); B: Matrix section with phenocrysts and/or xenoliths (optical microscopy).

Abbildung 23: Überblick über die Dünnschliffe der magmatischen Brekzien; A: Brekzientextur mit Klasten und Matrix (Durchlichtmikroskopie); B: Matrix Abschnitt mit Einsprenglingen oder Xenolithen (Durchlichtmikroskopie)

6.3 Alvikite

The alvikite veins have a calcite matrix, which is, however, partially altered and replaced by an amorphous to cryptocrystalline alumo-siliceous matrix in some samples. Especially, samples SES1.27 and SES1.28 contain large amounts of this alumo-siliceous matrix, while the alvikites with greyish matrix host the highest amount of calcite. Calcite is the only carbonate mineral in the matrix and it can contain up to 5 mol.% manganese and strontium. Coarse-grained minerals with a size up to a few millimetres are represented by apatite, phlogopite and magnetite.

Especially, the phlogopites are macroscopically visible, but also apatite show partly large crystals as detected in the igneous breccias. These big crystals can be considered as phenocrysts (Fig. 24). Monazite, REE-fluorocarbonates, pyrochlore, zirconolite and occasional sulphide minerals (pyrite, chalcopyrite, galena), uranophane and barite occur accessorily in the mineral association.

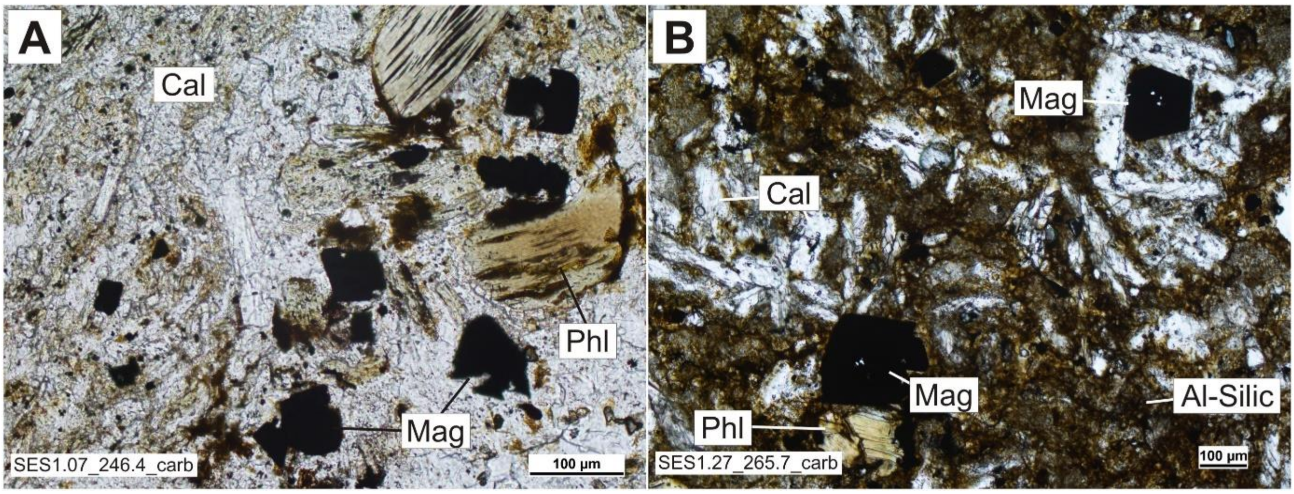

Figure 24: Overview of the alvikite thin sections; A: Alvikite with greyish matrix (optical microscopy); B: Alvikite with brownish matrix, more altered (optical microscopy).

Abbildung 24: Überblick über die Alvikit Dünnschliffe; A: Alvikit mit gräulicher Matrix (Durchlichtmikroskopie); B: Alvikit mit bräunlicher Matrix (Durchlichtmikroskopie)

6.4 Characterisation of relevant Minerals

In this chapter, all minerals and phases are described, which were detectable with microscopic methods. All percent or ppm values in this chapter refer to molar concentration, if not indicated differently. The molar concentration is recalculated from EDX-data. In addition, the description of the minerals and their occurrence refer to the alvikites and the matrix of the breccia samples unless otherwise specified.

6.4.1 Calcite

Calcite (**Ca[CO$_3$]**) is the main matrix-forming mineral in the alvikites and occur exemplarily in the thin section of the breccia sample SES1.18. It has a homogeneous appearance in the BSE-image, but shows crystal structures with different sizes under the optical microscope. The major part of the calcitic matrix is made of anhedral crystals, which are evenly distributed and variate in the size, depending on the sample, from a few µm up to 100 µm (Fig. 25 A,B). In addition, some areas contain much larger, anhedral crystals as determined in the surrounding matrix that have a size up to 300 µm (Fig. 25 C-D).

In calcite, the divalent calcium can be substituted by manganese, iron, magnesium, strontium, cobalt, zinc, barium, lead and REE (RÖSLER 1991). With the EDX, small amounts of magnesium, manganese, iron and strontium were detected in some calcites (Fig. 26; Tab. 7). Especially the difference between pure calcite and calcite with manganese or strontium is visible in the BSE-image and the chemical transition between calcite and manganese/strontium enriched calcite is sharp (Fig. 27). It can be concluded, that the different calcite compositions belong to different crystals and not to a zonation. In the breccia sample SES1.18, the calcites contain up to 5 % manganese, which is higher than in the alvikites. Whether there are traces of REE in the calcite, cannot be clarified with the EDX. If the calcite contains REE, these elements would be distributed homogeneously and the amount would be smaller than 0.1 %.

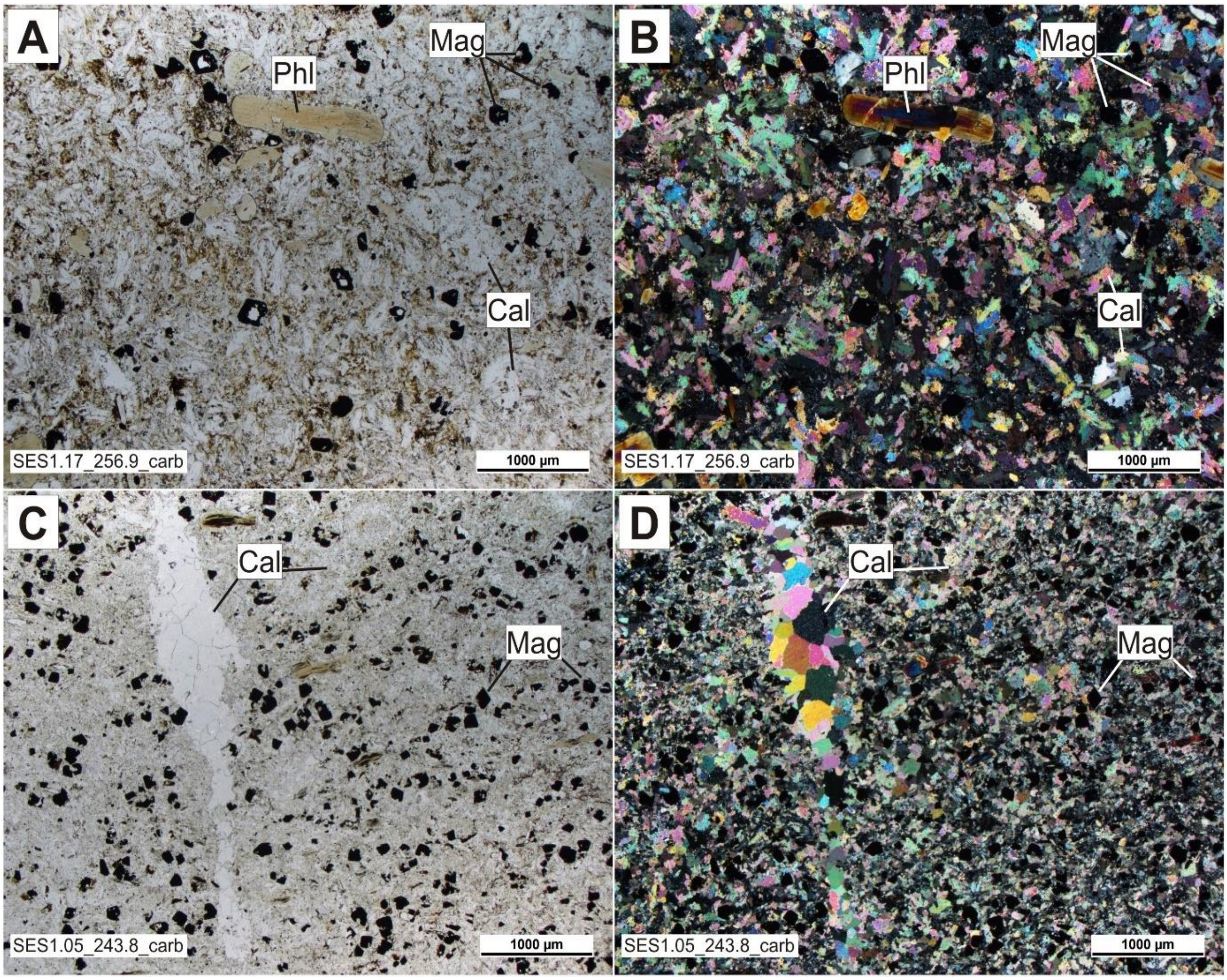

Figure 25: Textures of calcite under the optical microscope (B,D) with crossed nicols; A,B: Typical calcitic matrix in alvikites; C,D: Calcitic vein with bigger crystals.

Abbildung 25: Kalzittexturen unter dem Durchlichtmikroskop (B,D mit gekreuzten Nicols; A,B: Typische kalzitische Matrix in Alvikiten; C,D: Kalzitader mit größeren Kristallen

Table 7: Minor elements (EDX-data; n = 40) in calcite composition in alvikite and breccia.

Tabelle 7: Nebenelemente (EDX-Daten, n = 40) in der Kalzitzusammensetzung in Alvikiten und Brekzien

Element	Readings > LOD [%]	Average content [%]	Std. deviation [%]
Magnesium	50	0.35	0.19
Manganese	32	2.32	0.99
Iron	13	0.23	0.07
Strontium	53	0.41	0.34

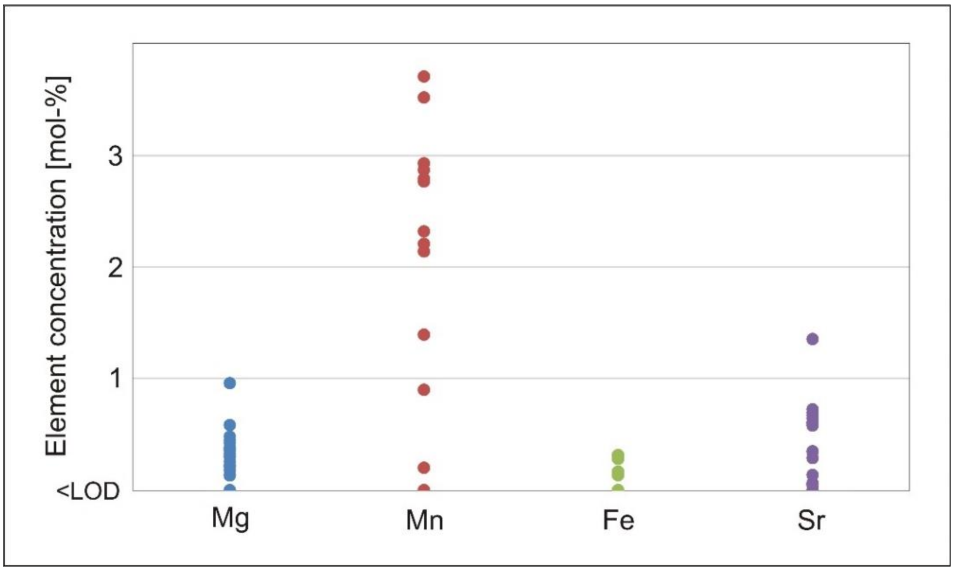

Figure 26: Distribution and concentration of minor elements in calcite crystals.

Abbildung 26: Häufigkeit und Konzentrationen von Spurenelementen in Calcit Kristallen

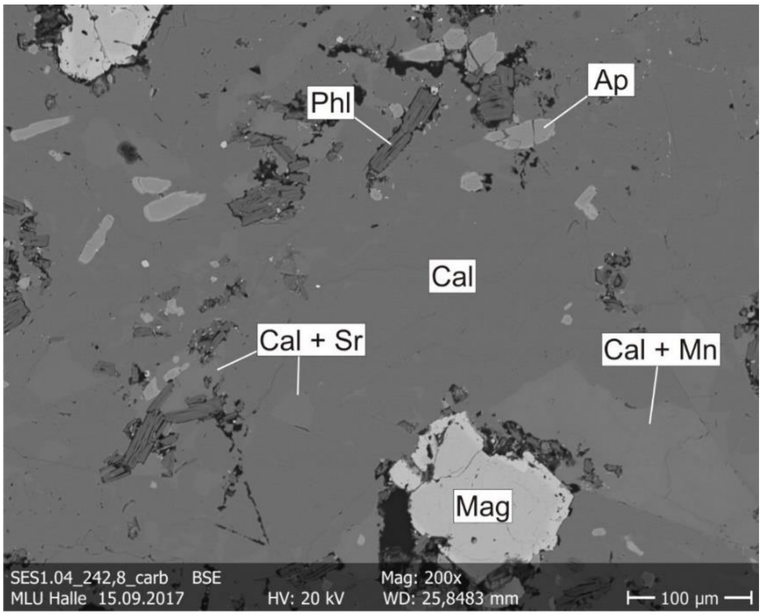

Figure 27: Calcite with different minor elements. The sharp transitions indicate crystal boundaries (SEM-BSE).

Abbildung 27: Calcite mit verschiedenen eingebauten Spurenelementen. Der scharfe Übergang deutet auf Kristallgrenzen (SEM-EDX)

6.4.2 Cryptocrystalline matrix and clay minerals

In all thin sections, especially from the igneous breccias, amorphous to cryptocrystalline areas were observed. Commonly they look very heterogeneous in the BSE-image and show a higher amount of cavity than the surrounding phases. In order to characterize these phases, reflectance spectroscopy was carried out (chapter 6.5). The chemical composition of the amorphous areas can roughly indicate estimations on the mineral content. According to the composition, the cryptocrystalline matrix is built up by alumo-siliceous phases and iron oxides/hydroxides. In general, these two mineral groups can be clearly distinguished, but measurements represent mixtures of both (Fig. 28). This can be caused by a mixed phase or by two or more single phases that are physically not measurable by EDX-analysis, because of the small particle size.

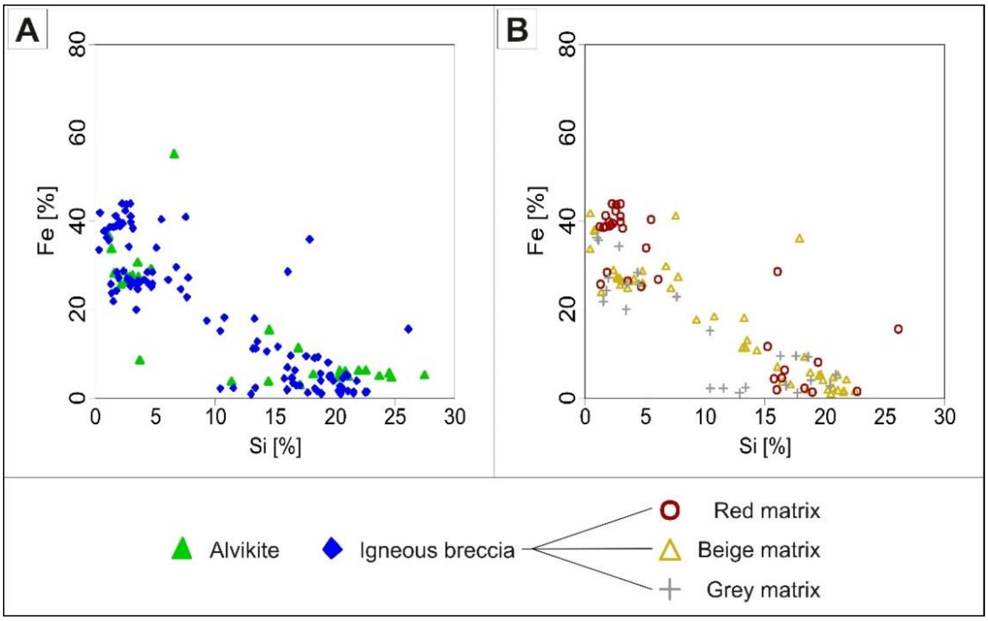

Figure 28: Fe-Si-ratio of cryptocrystalline phases determined by EDX-analysis (n=137). Although two groups are recognizable, either of iron- or silica-rich composition, some samples with moderate Fe and Si content represent a transitional zone.

Abbildung 28: Fe-Si-Verhältnis der kryptokristallinen Phasen bestimmt durch EDX-Analysen (n= 137). Obwohl mit eisen- und siliziumreichen Phasen zwei Gruppen ausgemacht werden können, zeigen einige Probenpunkte mit moderaten Fe- und Si-Gehalten das Vorhandensein eines Übergangsbereiches.

6.4.2.1 Iron oxyhydroxides

Iron oxyhydroxides can be found in the breccia as well as in the alvikite samples. While the iron phases are mostly occurring in smaller altered areas in alvikites, they form wide parts of the matrix in breccias (Fig. 29 A). In breccias with red matrix, nearly the complete matrix is made of hematite, which can be determined by optical reflectance microscopy (Fig. 29 B).

Areas with iron phases show often a heterogenic appearance in BSE-images and occasionally a zonation by altering distribution of different colours (Fig. 29 C). These are caused by alternating amount of iron, which is varying from 20 % to 40 % in the most cases. Furthermore, these phases contain smaller amounts of titanium (up to 5 %).

In some thin sections occur altered phlogopite crystals, in which secondary iron oxyhydroxide needles were formed. These needles can be interpreted as goethite and are described in more detail in the mica section below (chapter 6.4.3).

6.4.2.2 Alumo-siliceous matrix

The determination of the predominantly amorphous alumo-siliceous matrix (alumosilicates) cannot be carried out unequivocal with microscopic methods, because it lacks of clearly defined mineral properties. These phases consist of silicon (10-25 %) and alumina (5-15 %) as major elements. Furthermore, small amounts of magnesium (1-3 %), chlorine (<1 %), potassium (1-2 %), calcium (0.5-4 %) and iron (3-15 %) are typical components, while sodium (<1 %) and titanium (<1 %) occur only in some measured phases.

Especially the varying amount of iron causes a heterogeneous appearance in the BSE-image. In sections, where the amount of iron is consistent, the BSE-image looks more homogeneous (Fig. 30). Alumosilicates partly show a laminated shape assumedly representing phyllosilicates.

6.4.3 Mica

Besides the quartz phenocrysts in the porphyry core section, Mica represents the largest minerals, which can be found in the examined drill core. They are anhedral and show mostly elongated crystals, which occur in a size range from few micrometres to few millimetres. Especially, the large phenocrysts can be detected easily with the optical microscope. Micas show a pleochroism from white to pale yellow and show a variety of second order interference colours with crossed nicols (Fig. 31), so they can be interpreted as biotites, more precisely as phlogopite, the magnesium-rich endmember of the biotite group (BRIGATTI et al. 1996). Annite crystals (the iron endmember) would show more greenish to brownish colours (FLEET et al. 2003).

The possible chemical variability of micas makes their classification with the EDX-data more complicated, because some elements like lithium cannot be detected and other elements like iron or alumina can occur in the octahedron as well as in the tetrahedron position (FERRARIS & IVALDI 2002). With the formula **Li_20** = [2.1/(0.356 + MgO)] - 0.088, the amount of lithium (oxide) can be estimated by the amount of magnesium (TISCHENDORF et al. 1999). Therefore, the average lithium amount of the 53 EDX measurements is less than 0.05 wt.%.

Further signs of alteration could be detected with the help of microscopy images. Goethite is intergrown within the interlayers of mica crystals. Depending on the cutting position of the thin section, the goethite is visible as stellate needles (Fig. 32 A) (if looking on the layers), or as brownish stripes (if looking with an angle) (Fig. 32 B). In the BSE-image, it can be shown, that some crystals are disintegrate, presumed along of interlayers (Fig. 32 C). In the sections with high amounts of barium, the micas have an enriched edge with up to 3 % barium (Fig. 32 D).

In one alvikite thin section (sample SES1.28), an approximately 3 mm long mica clast was detected. Although there are even larger crystals in other samples, the clast is special, because it consists of several smaller crystals in different orientations. Therefore, it can be interpreted as xenolith from a deeper stage (Fig. 33).

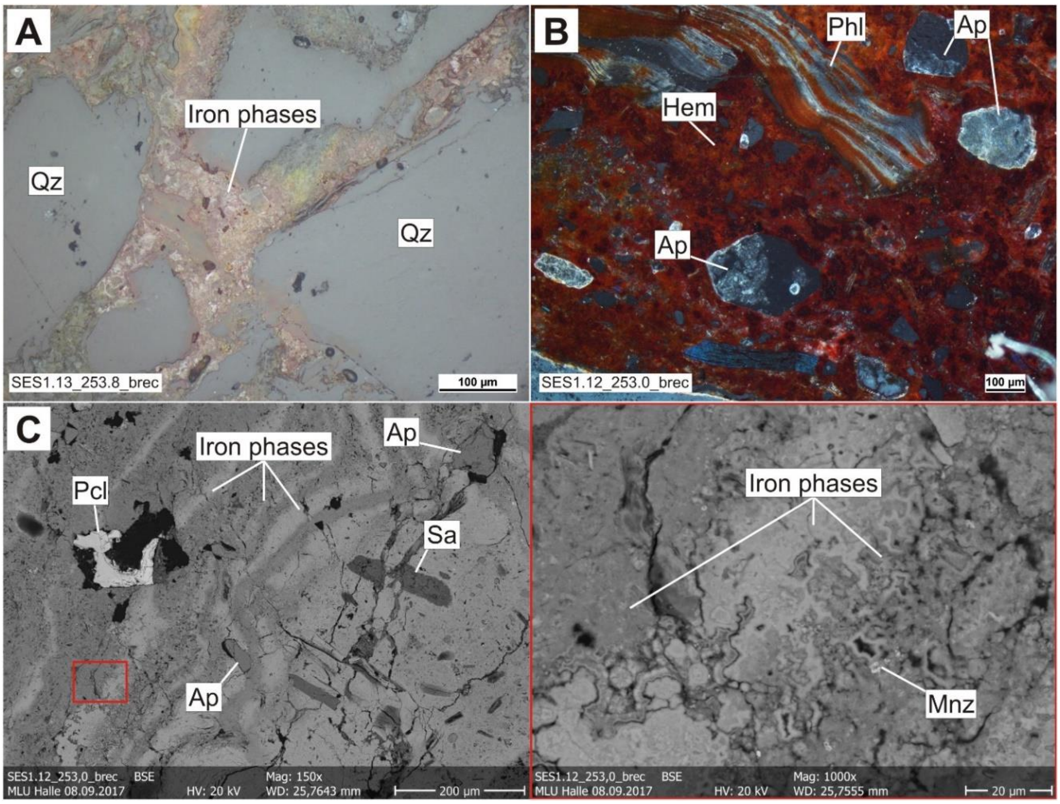

Figure 29: Breccia samples with iron oxyhydroxides; A: Iron phases, not determinable with microscopic methods (optical reflectance microscopy); B: Hematite dominated breccia sample (optical reflectance microscopy, crossed nicols); C: Hematite dominated matrix of a breccia sample (SEM-BSE).

Abbildung 29: Brekzienproben mit Eisen-Oxyhydroxiden; A: Eisenphase, nicht genauer bestimmbar mit mikroskopischen Methoden (Auflichtmikroskopie); B: Hämatit dominierter Brekzienbereich (Auflichmikroskopie, gekreuzte Nicols); C: Hämatit dominierte Matrix einer Brekzienprobe (SEM-BSE)

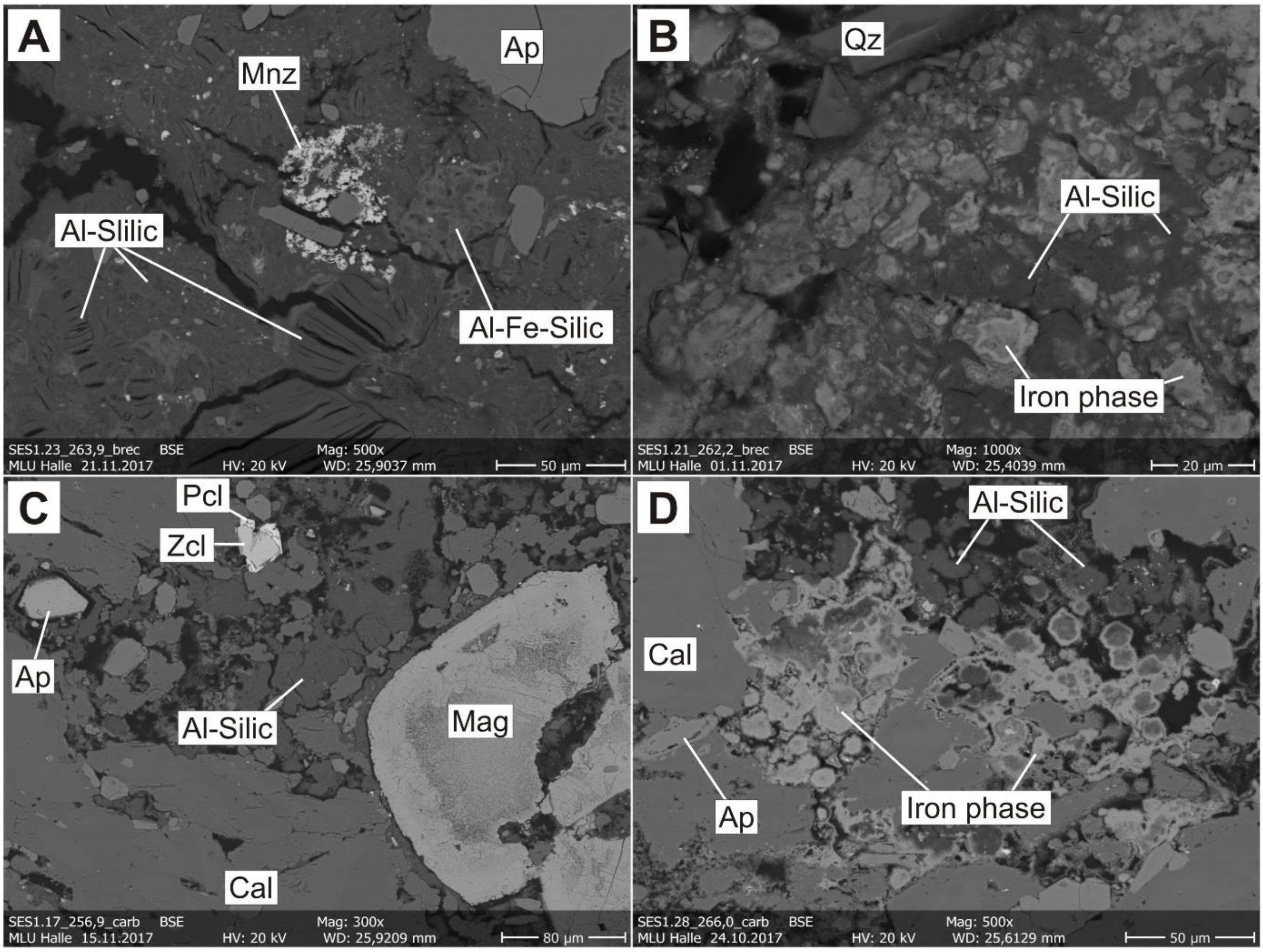

Figure 30: Examples for alumo-siliceous phases (SEM-EDX); A: Alumosilicates in a breccia section; the layer structures in the lower left corner indicate clay minerals (phyllosilicates); B: Alumosilicates and iron oxyhydroxydes in a breccia; C: Alumosilicates in altered parts of the calcitic matrix; D: Alumosilicates and iron phases in an alvikite. The variation of the iron content causes the heterogeneous character in B and D.

Abbildung 30: Beispiele für alumo-silizische Phasen (SEM-EDX); A: Alumosilikate in Brekzienbereich; die Lagenstruktur in der unteren linken Ecke sind ein Indiz für Tonminerale; B: Alumosilikate und Eisenphasen in einem Brekzienschliff; C: Alumosilikate in alterierten Bereichen zwischen kalzitischer Matrix in einem Alvikit; D: Alumosilikate und Eisenphasen in einem Alvikit. Die Variation des Eisengehalts verursacht den heterogenen Charakter in B und D.

6.4.4 Apatite

Minerals of the apatite-group occur with an abundance of 5-20 vol.% in the majority of the samples. The shape of the detected apatites is varying from large mostly euhedral (100-1000 µm) phenocrysts, which can be broken, to smaller anhedral to euhedral crystals (5-100 µm), which are unevenly distributed in the matrix.

Apatites are one of the earliest mineral, which crystallize in a carbonatitic magma. Because of the big difference in density between the carbonatitic magma (≤ 2.8 g/cm3; (Sykes et al. 1992)) and the apatites (3.1-3.2 g/cm3) and the low viscosity of the melt, there is a gravitational separation of the apatite from their parental magma. These apatites occur as phenocrysts in the subvolcanic environment (Chakhmouradian et al. 2017).

Apatite phenocrysts occur in the breccia samples as well as in the alvikites. They are often euhedral, slightly rounded and can be fractured (Fig. 34 A, B). Especially in the breccia samples occur large apatite fragments without coherent structure between individual fragments (Fig. 34 D). The additional occurrence of smaller, partly euhedral, partly anhedral apatites gives the evidence, that apatite was formed subsequently.

These apatites can also be slightly rounded, but show more often slightly dissolved crystal rims

In some thin section, predominantly from the alvikite samples, the apatites have a REE-enriched rim (Fig. 34 C). This rim has mostly no sharp demarcation from the inner part of the apatite crystals and can be up to 5 µm wide. It was mainly detected at smaller apatites, but occurs also narrower developed on larger phenocrysts.

The content of REE detected in the rim area is in average 0.7 % (Tab. 8). This enrichment relative to the core goes along with the enrichment of silicon and decreasing amounts of fluorine (Fig. 35). In general, fluorine is the only possible detected anion, which can be incorporated in apatites, so that it can be estimated, that a part of apatite represents fluoroapatite. Chlorine only occurs in some crystals with an amount of less than 0.3 % and hydroxide cannot be detected by the EDX. Furthermore, there is no significant difference in the EDX-data between the small crystals and the large phenochrysts.

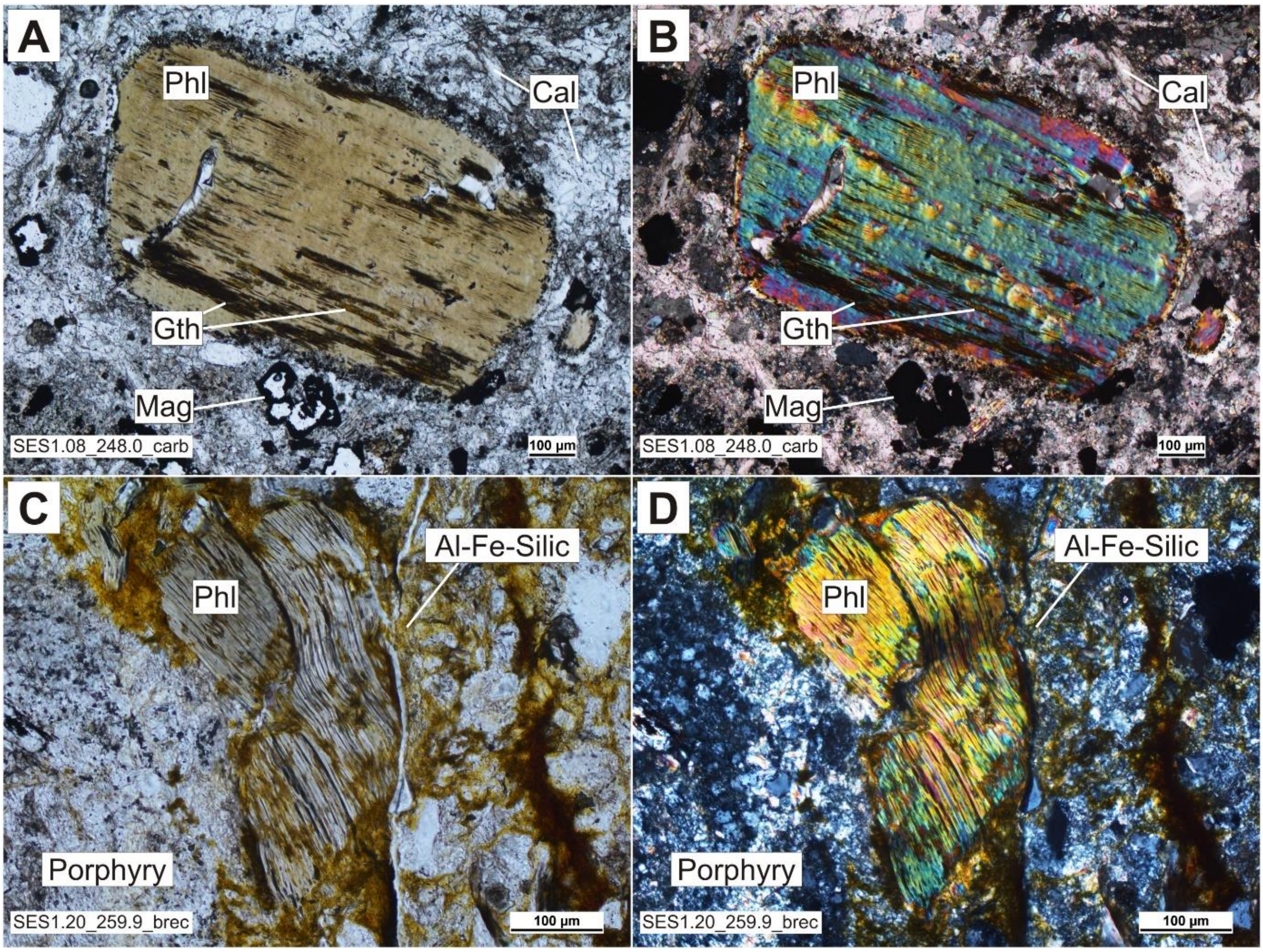

Figure 31: Optical mircoscopy image of phlogopites (B,D with crossed nicols); A,B: Phlogopite crystal in an alvikite; C,D: Phlogopite crystal in a breccia (in the matrix, surrounded by clasts). The pale yellow colour under uncossed nicols indicates, that the mica is magnesium-rich.

Abbildung 31: Durchlichtmikroskopiebilder von Phlogopiten (B,D mit gekreuzten Nicols); A,B: Phlogopitkristall in Alvikitbereich. C,D: Phlogopitkristall in Brekzienbereich (in Matrix, von Klasten umgeben). Die leicht gelbliche Farbe im Hellfeld impliziert, dass die Glimmer magnesiumreich sind.

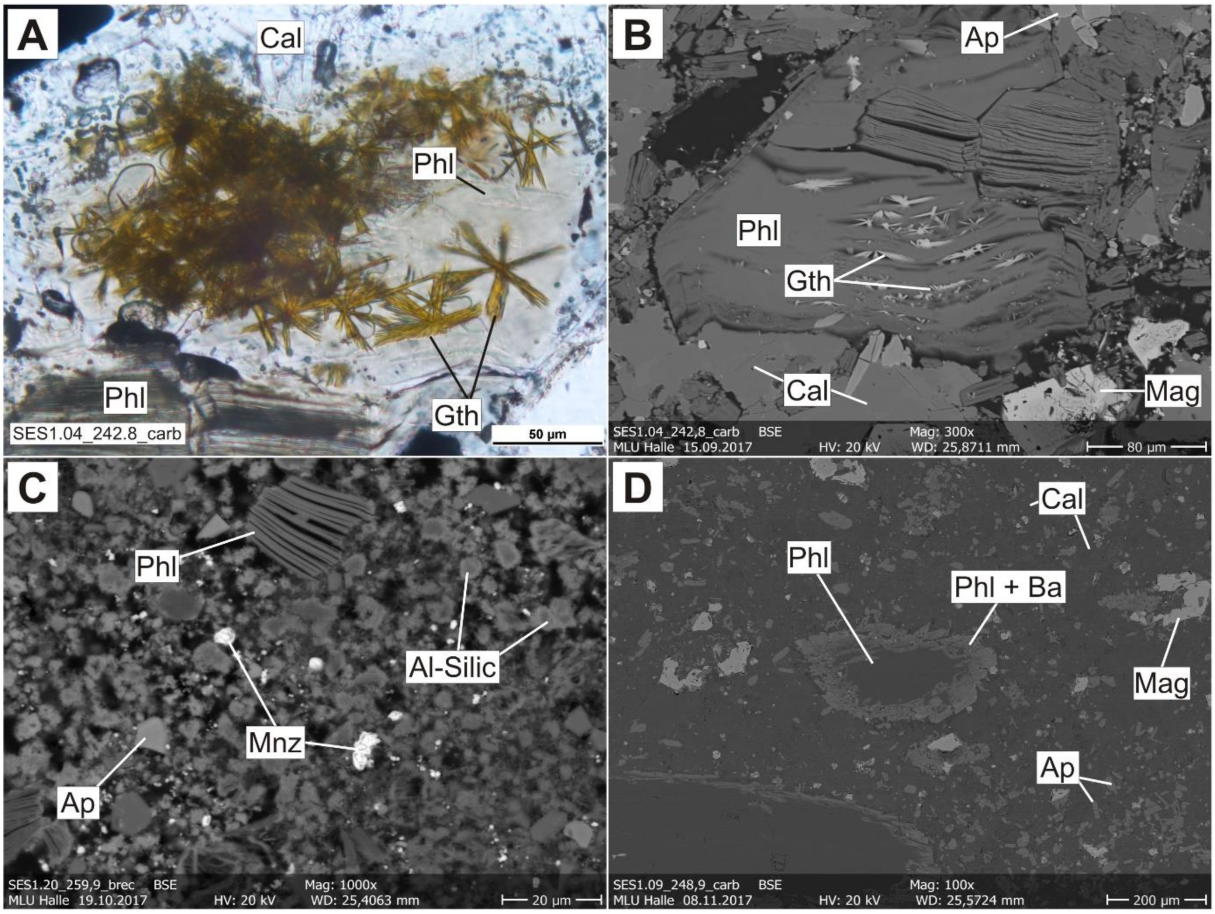

Figure 32: Indications of alteration at phlogopite crystals; A: Secondary goethite on a phlogopite (optical microscopy); B: Secondary goethite between phlogopite layers (SEM-EDX); C: Altered and partly decomposed phlogopite (SEM-EDX); D: Phlogopite with barium-enriched rim (SEM-EDX).

Abbildung 32: Alterationsspuren an Phlogopit-Kristallen; A: Sekundäre Goethitausfällungen auf einem Phlogopit (Durchlichtmikroskopie); B: Sekundäre Goethitausfällungen zwischen Phlogopit-Layern (SEM-EDX); C: Alterierter und zersetzter Phlogopit (SEM-EDX); D: Phlogopit mit Barium-angereichertem Randbereich (SEM-EDX)

Table 8: Comparison of the content of selected elements measured in the core (n=49) and rim (n=21) of apatite crystals with EDX-analyses.

Tabelle 8: Vergleich der Gehalte von bestimmten Elementen, gemessen mit EDY-Analysen im Kernbereich (n=49) und Randbereich (n=21) von Apatit-Kristallen

		Fluorine [%]		Silicon [%]		REE [%]	
		Core	Rim	Core	Rim	Core	Rim
All values	Average content	2.06	0.72	0.66	1.25	0.11	0.73
	Std. deviation	2.32	1.27	0.41	0.65	0.24	0.38
	Readings > LOD	55	30	59	90	29	90
Readings > LOD	Average content	3.74	2.40	0.76	1.41	0.38	0.81
	Std. deviation	1.85	1.12	0.33	0.46	0.30	0.30

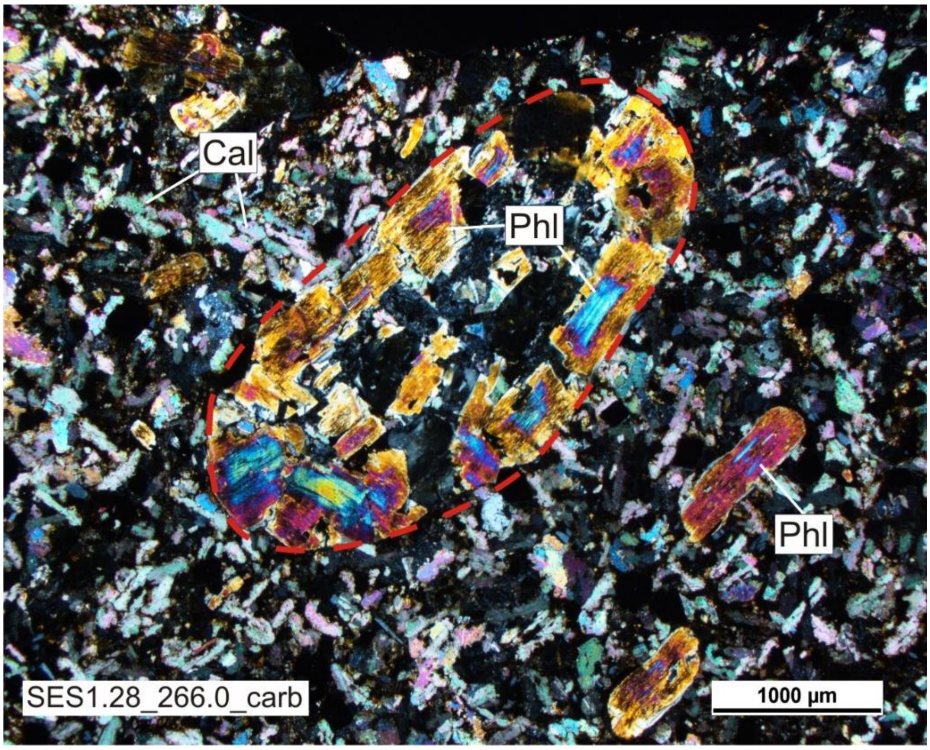

Figure 33: Phlogopite grain in an alvikite sample. The texture, which is consisting of many smaller crystals, allows the interpretation as xenolith (optical microscopy, crossed nicols).

Abbildung 33: Phlogopit Korn in Alvikitprobe. Die Textur, bestehend aus mehreren kleinen Kristallen, kann auf einen Xenolith hinweisen (Durchlichtmikroskopie, gekreuzte Nicols).

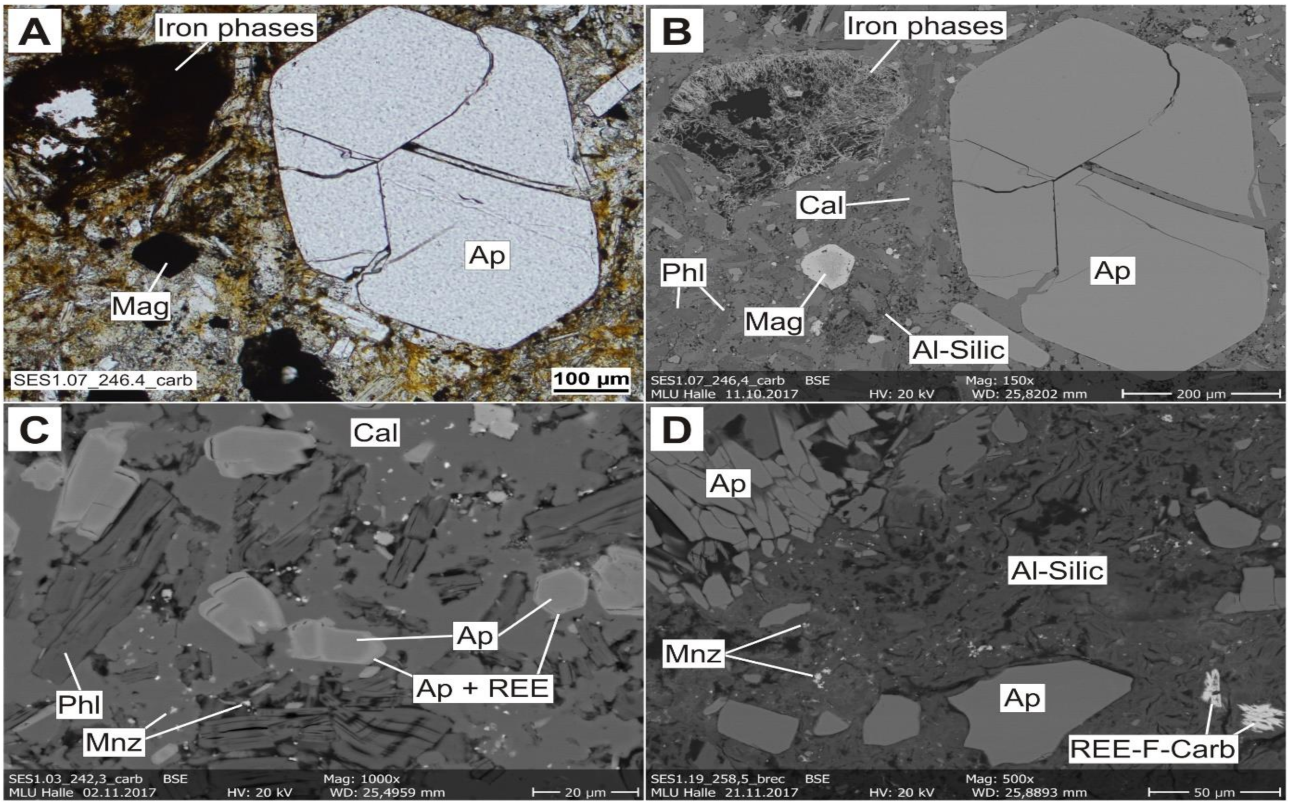

Figure 34: Examples for apatite forms: A: Euhedral phenocryst in an alvikite section (optical microscopy); B: Euhedral phenocryst in an alvikite section (SEM-BSE); C: Small apatites with REE enriched rim in an alvikite section (SEM-BSE), D: Fractured apatites in a breccia section (SEM-BSE).

Abbildung 34: Beispiele für Apatit-Formen: A: Idiomorpher Einsprengling in einem Alvikitbereich (Durchlichtmikroskopie); B: Idiomorpher Einsprengling in einem Alvikitbereich (SEM-BSE); C: Kleine Apatite mit einem an SEE angereichertem Saum in einem Alvikitbereich (SEM-BSE); C: Zerbrochene apatite in einem Brekzienbereich (SEM-BSE)

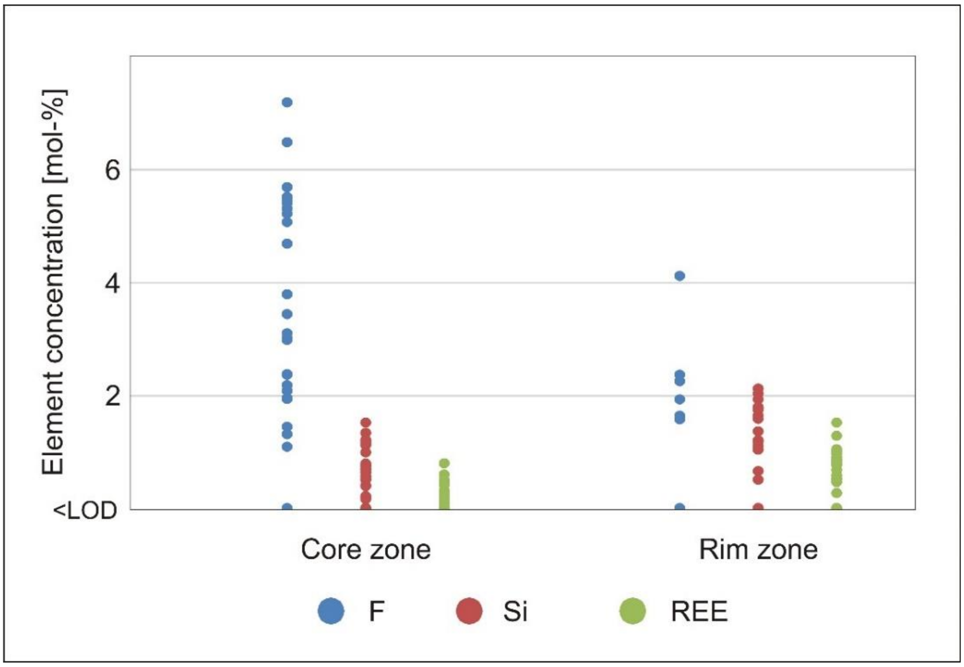

Figure 35: Distribution of minor elements in the apatite crystals, comparing core and rim. The rim has increased values for Si and REE, while F occurs with higher amounts in the core zone.

Abbildung 35: Verteilung von Nebenelementen in Apatit-Kristallen, Rand- und Kernbereich vergleichend, Randbereich hat höhere Gehalte an Si und SEE, während F stärker im Kernbereich vorkommt

6.4.5 Magnetite

In the examined thin sections, magnetite predominantly occurs in the alvikites, while it is very rare in the igneous breccias. The crystals are euhedral, often octahedral and sometimes show twinning. Magnetite crystals are between 50-150 µm large and occur homogeneous distributed (Fig. 36). In some samples, single crystals reach up to 800 µm size.

Depending on the thin section, different grades of alteration can be determined, which are obviously not correlating with the colour of the matrix (alvikite sections) and the alteration of the surrounding textures. In many samples, magnetite is recognizable as euhedral crystals with slight dissolution features at the crystal edges and occasionally with titanium-rich phases as a product of segregation. In the BSE-image is often a zonation from the core to the edge visible, which is an indication of the beginning alteration of magnetite. In some crystals, other phases like secondary apatites were detected in the altered centre.

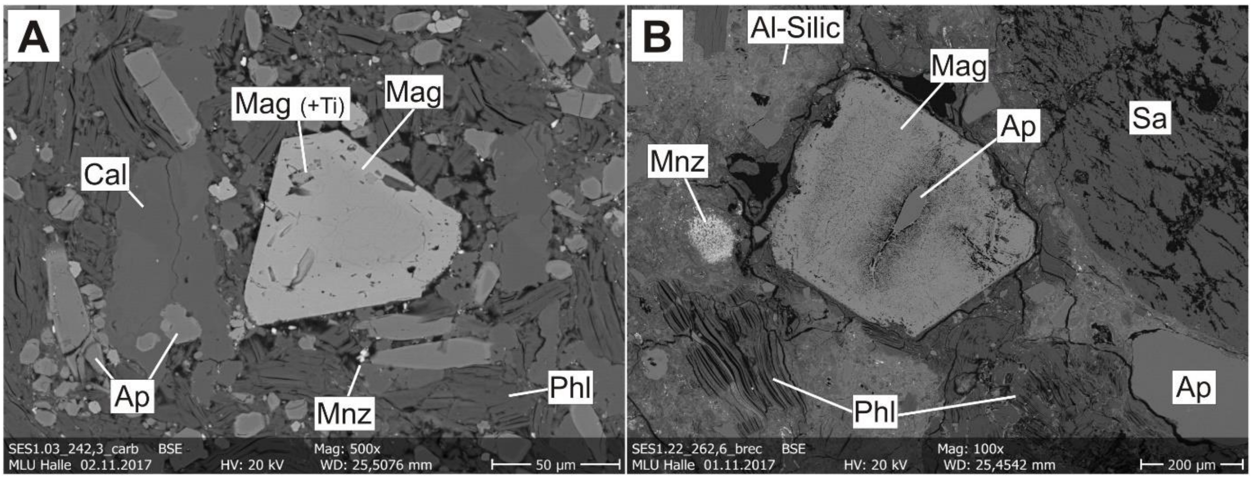

Figure 36: Euhedral magnetite in alvikite section (A) and breccia section (B) (SEM-EDX).

Abbildung 36: Idiomorphe Magnetit Kristalle in Alvikitbereichen (A) und Brekzienbereichen (B) (SEM-BSE)

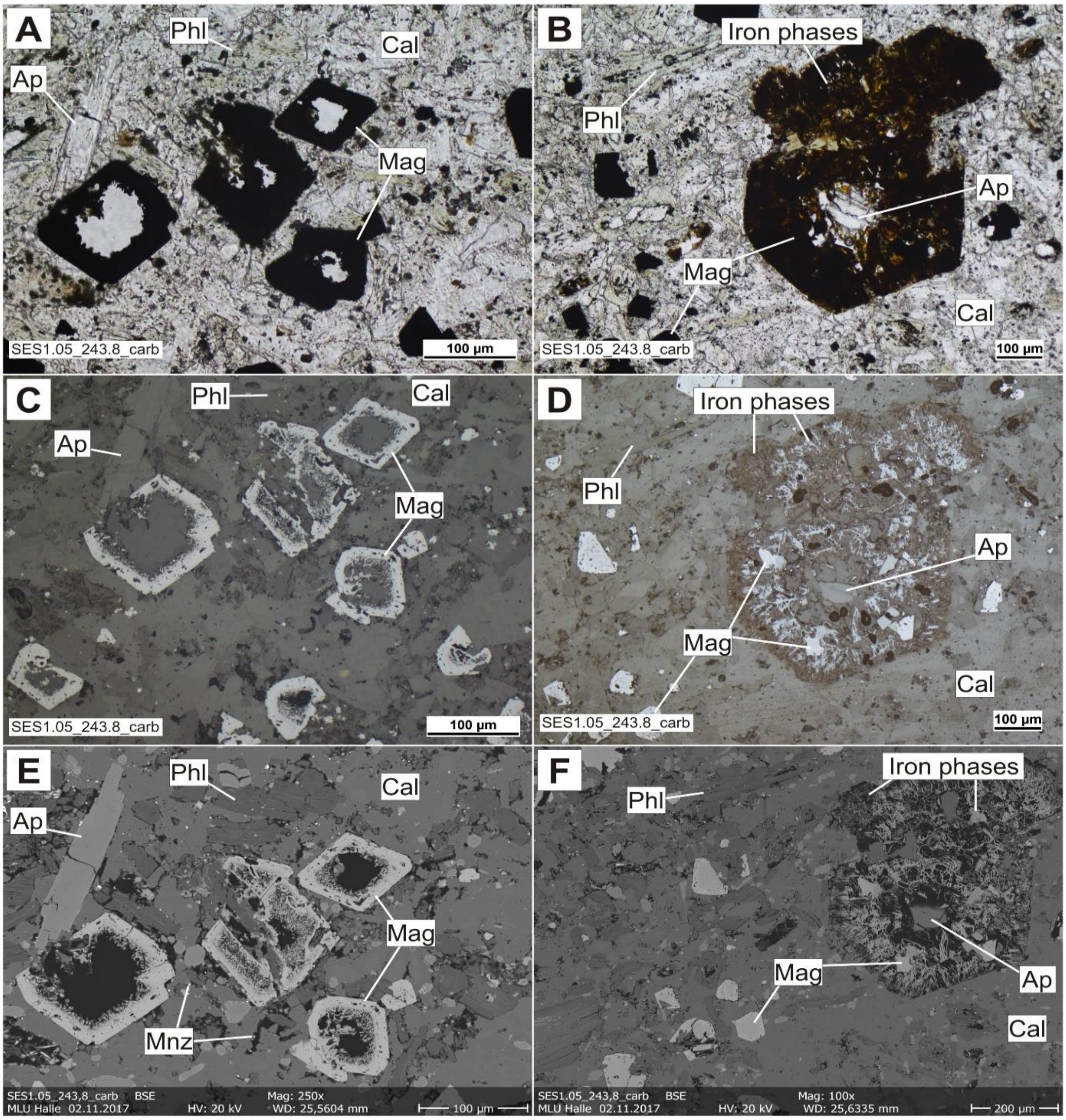

Figure 37: Different dissolution stages of magnetites in alvikite sections; left side: partially dissolved crystals; right side: nearly complete dissolved magnetite, were only magnetite fragments are remaining (A,B: optical microscopy; C,D: optical reflectance microscopy; E,F: SEM-BSE).

Abbildung 37: Verschieden starke Lösungserscheinungen an Magnetit in Alvikiten; linke Seite: teilweise Aufgelöster Kristall; rechte Seite: fast komplett weggelöster Kristall, in dem nur noch Magnetit Fragmente erhalten sind (A,B: optische Mikroskopie; C,D: Auflichtmikroskopie; E,F: SEM-BSE).

In other sections, magnetite appears more altered, so that the complete core is missing. In extreme cases, the former magnetite can only be identified by a phenocryst and small remaining crystal fragments (Fig 37). These dissolved areas are in general empty or contain secondary phases like apatite and amorphous iron-oxyhydroxide.

EDX-measurements on magnetite phenocrysts (total 32) show a high amount of iron (25-35 %), the amount of titanium (2-8 %) and the amount of oxygen, which is approximately 57 % and a bit lower than in the other iron phases. A negative correlation exists between iron and titanium, which displays that crystals represent members of the magnetite-ulvite solution series (Fig. 38). Other elements detected are magnesium (3-5 %), alumina (1-4 %) and manganese (0.5-1.5 %).

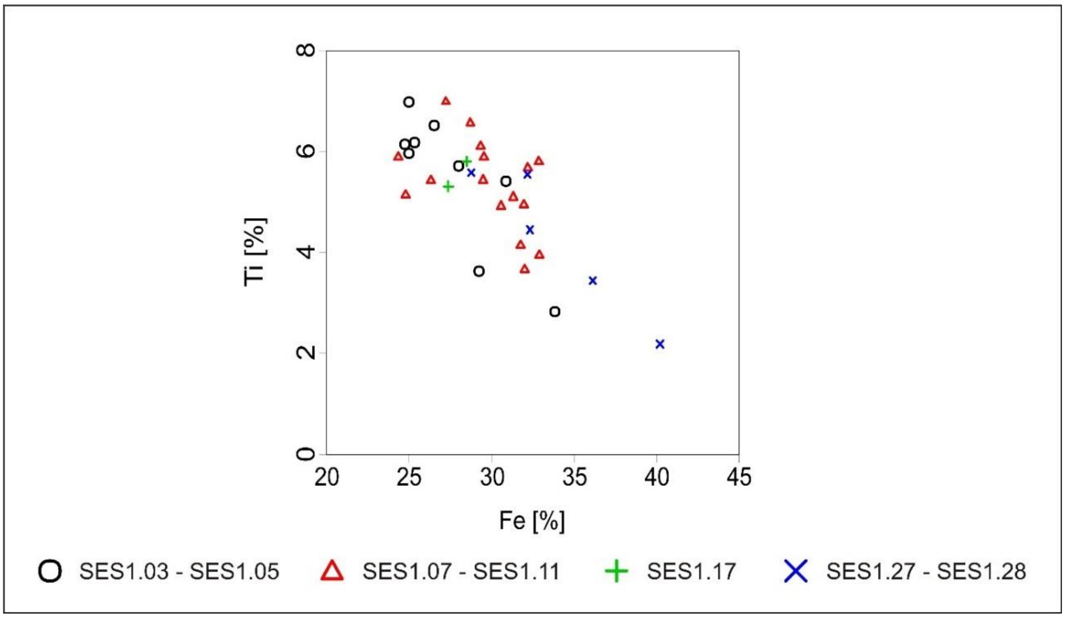

Figure 38: Titanium-iron plot of the magnetites from alvikite sections (EDX data, n = 32). The negative correlation is caused by solid solution between magnetite and ulvite.

Abbildung 38: Titan-Eisen-Plot von den Magnetiten der Alvikitbereiche (EDX-Daten, n = 32). Die negative Korrelation entsteht durch die Mischreihe zwischen Magnetit und Ulvit.

6.4.6 Monazite

All detected REE-containing phosphates were classified as monazite, although the difference between monazite and rhabdophane, which also belongs to the monazite-group, was indistinguishable with EDX-measurements.

Monazite was found in nearly each thin section of the breccias and alvikites. It can easily be detected in the BSE-image by its very intense brightness because of the great mass of the REE atoms. The big majority of the detected monazite crystals was smaller than 1 µm in diameter and occur in different textures, which are mostly related to alteration.

In the alvikites, the monazites grains are finely distributed in the matrix and often associated to alteration areas like joints, areas with cryptocrystalline alumosiliceous matrix and other altered minerals (Fig. 39 B). In the breccia samples, finely disseminated monazites represent one of three different textures (Tab. 9). These monazites are not bound to alteration structures in contrast to the alvikite samples, because the whole matrix consists of secondary phases (Fig. 39 A). The content of this fine disseminated monazite is varying in a wide range. While in some thin sections only some single grains occur randomly, a high concentration of monazite is associated with the matrix in other section. Partially the REE-concentration is varying in one section across streak structures.

The second texture is a corona structure around quartz clasts that is formed by monazite. This texture occurs in the breccia samples with a minor amount of clasts. The quartz clasts are enveloped by a small stripe strongly enriched with monazites (Fig. 40 B, C). With the optical microscope, this texture can be only suspected by a diffuse greyish rim around quartz clasts (Fig. 40 A). Some quartz clasts seem to be impregnated with titanium in these areas, which is remarkable, because monazite does not contain any titanium (Fig. 40 C).

Quartz grains contain spots at the edge, which contain up to 10 % (20 wt.%) titanium. The size of these titanium enriched zones correlate with the amount of monazite next to the clast.

The third texture is characterized by an area with a remarkable high content of monazite. This accumulation occurs very randomly distributed in the matrix of the breccia samples. There are replacements, which are related to former minerals and therefore have the shape of phenoclasts as well as fillings, which are related to joints or other cavities and have no well-defined shape (Fig 41. A,B). The latter can be found nearly in all breccia samples expect in those with a grey matrix. In the sections with a minor content of clasts, there are also areas, where monazite occurs as corona texture accompanied by irregular accumulation (Fig. 41 C).

In the porphyries, monazite occur very rare as accessory mineral and therefore it cannot be clarified in the frame of this study, whether this small amount of monazite was formed in relation to the carbonatitic intrusion, or originate from the porphyry genesis.

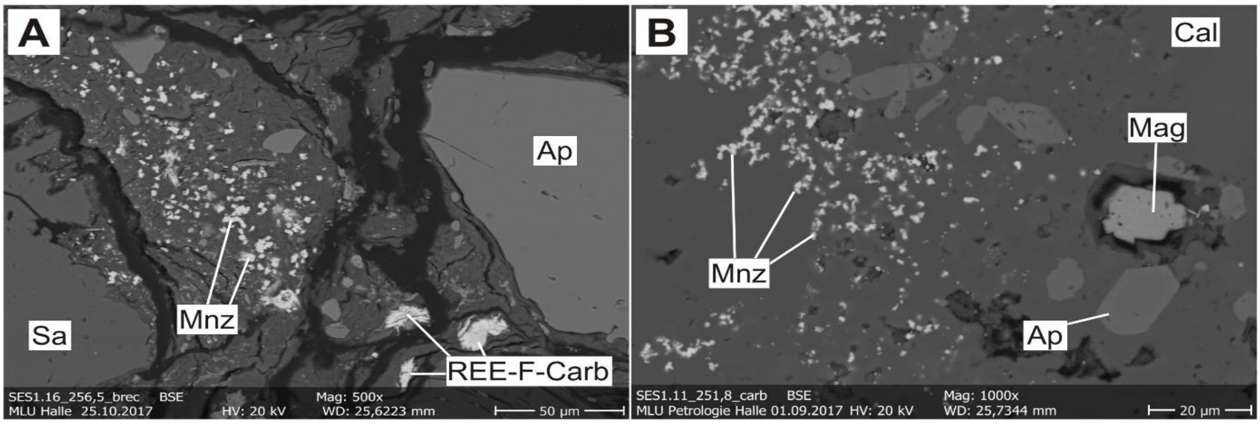

Figure 39: Finely distributed monazites in A: Breccia section and B: Alvikite section (SEM-BSE). In the alvikite samples, monazites only occur in this texture and are linked to alteration structures.

Abbildung 39: Fein verteilte Monazite in A: Brekzienprobe und B: Alvikitprobe (SES-BSE). In den Alvikitbereichen treten Monazite nur in dieser Textur und an Alterationsstrukturen gebunden auf.

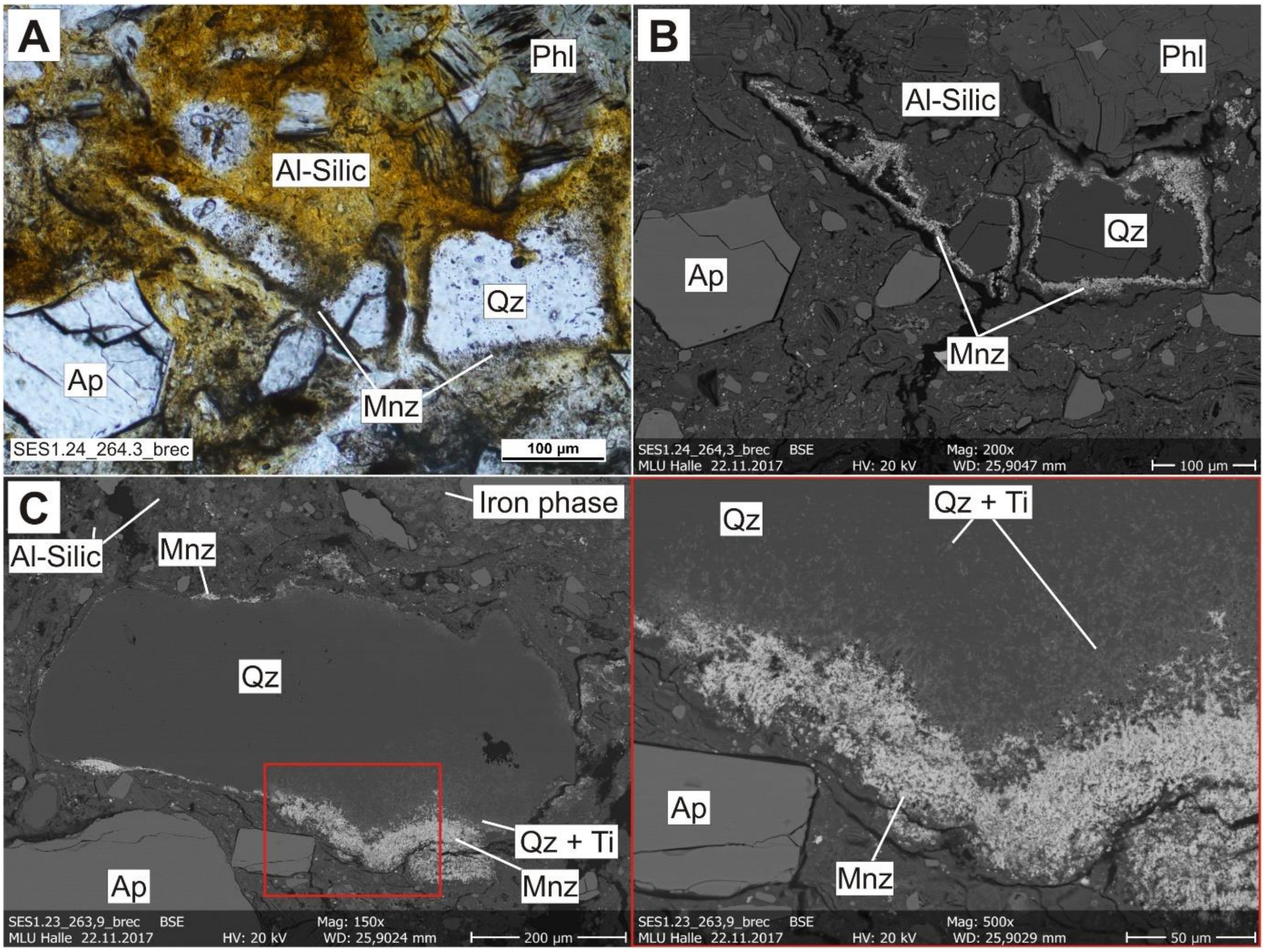

Figure 40: Monazite occurrences associated with corona textures; A: Optical microscopy image; B: SEM-BSE image; C: Corona texture with titanium-impregnated quartz. The intensity of the Ti-enriched edge is correlating with the size of the corona (SEM-BSE).

Abbildung 40: Monazit Vorkommen, assoziiert mit Corona-Texturen; A: Durchlichtmikroskopie; B: SEM-BSE; C: Corona Textur mit Titan-imprägnierten Quarz. Die Intensität des Ti-angereicherten Saumes korreliert mit der Größe der Corona.

Table 9: Occurrence of monazite textures in breccia samples. * The amount of clasts in this part of the drill core is approx. 50 %. The thin section of SES1.18 is not representative.

Tabelle 9: Vorkommen der Monazit Texturen und Akkumulationen in den Brekzienproben. * Der Anteil an Klasten ist in diesem Teil des Bohrkerns ca. 50%. Der Dünnschliff SES1.18 ist nicht repräsentativ.

Sample	Colour of the matrix	Amount of clasts [%]	Finely distributed monazites	Corona texture	Monazite accu-mulation
SES1.12	red	70	●		●
SES1.13	beige	65	●		●
SES1.16	grey	50	●		
SES1.18	grey	0*	●		
SES1.19	grey	50	●		
SES1.20	beige	70	●		●
SES1.21	red	40	●		●
SES1.22	beige	25	●	●	●
SES1.23	beige	30	●	●	●
SES1.24	beige	30	●	●	●
SES1.29	red	35	●	●	●
SES1.30	beige	70	●		
SES1.31	grey	65	●		●

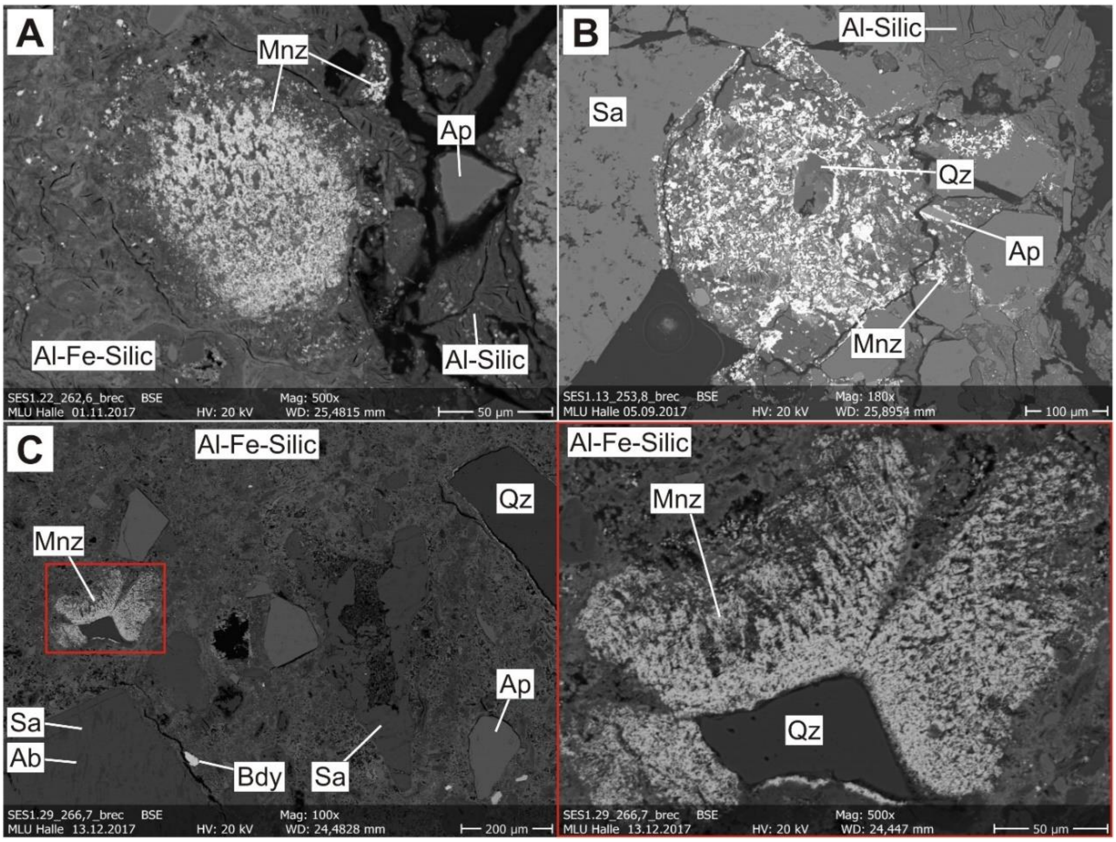

Figure 41: Monazite accumulations (SEM-BSE); A,B: Monazite accumulation in a phenoclast; C: Combination of accumulation and corona structure.

Abbildung 41: Monazit Akkumulationen (SEM-BSE); A,B: Monazit Anreicherungen in einem Phenoklast; C: Kombination von Akkumulation und Corona-Struktur

EDX-measurements on monazite crystals are a bit technically complicated, because of the small size of the crystals (excitation domain of the electron beam). Therefore, some element concentrations (like the concentration of calcium) are influenced by surrounding phases (like calcite) that also contain these elements. For the REE as well as for a couple of other elements the data is precise enough, because they do not occur in the adjacent phases.

The amount of REE ranges in average from 7.9 to 10.4 % (35.9-42.1 wt.%), while breccia-hosted monazites contain in average more REE than those in the alvikite section. Cerium, followed by lanthanum and neodymium are the REE with the highest content. The distribution of these three elements is similar to the whole rock analyses. While the breccia- and porphyry-hosted monazites show nearly the same distribution, the differences in monazites of the alvikite sections varying over a wider range (Fig. 42 A). This variation is primarily caused by a lower amount of cerium in the greater part of these measurements and explains the generally lower content of total REE in alvikite sections. The comparison of monazites associated with individual alvikite veins revealed no pattern or correlation (Fig. 42 B).

The REE distribution of the breccia-hosted monazites is comparable to the average composition of carbonatite-hosted monazites (Rosenblum & Fleischer 1995) (Fig. 42 C).

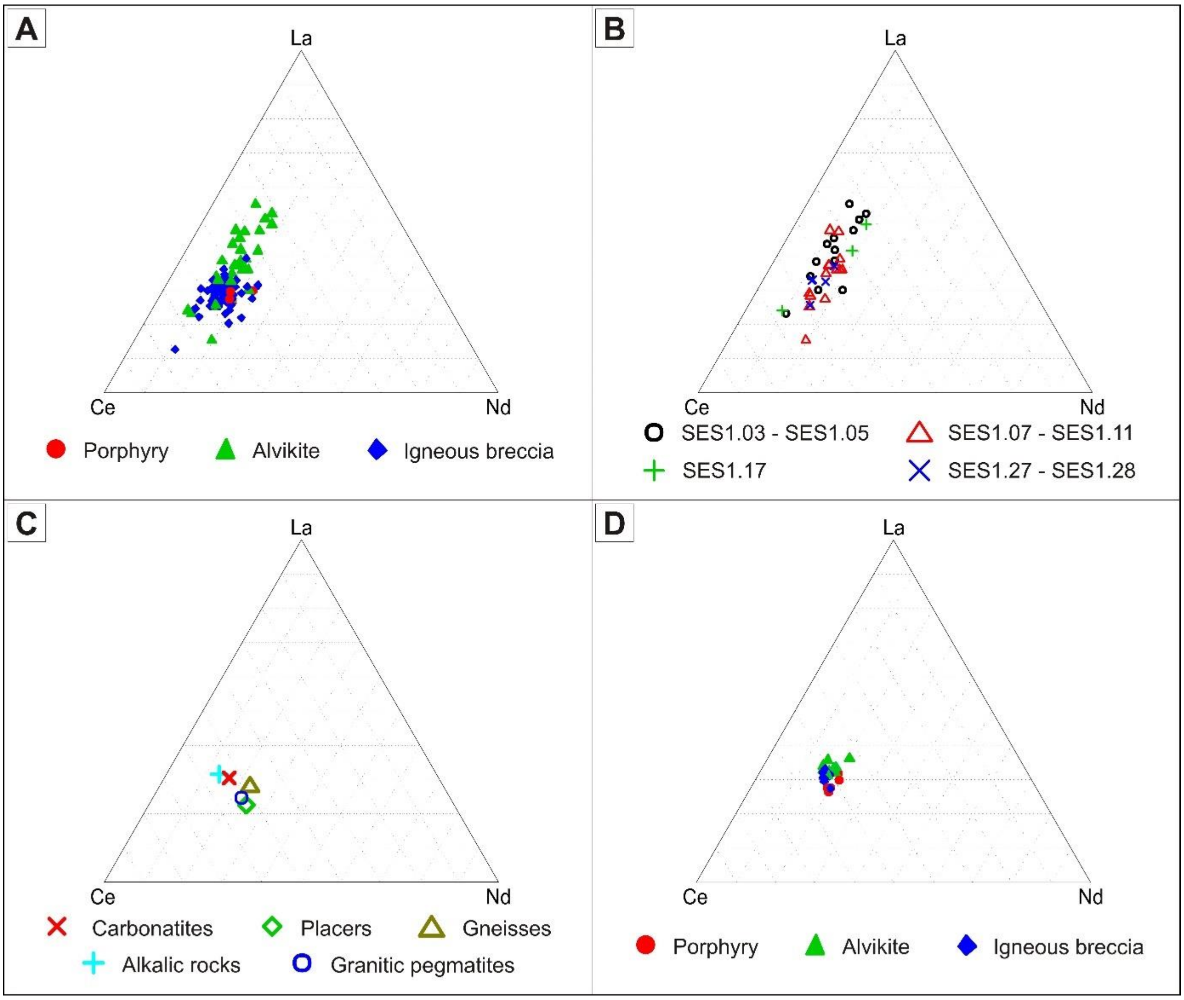

Figure 42: Distribution of the most common REE in monazites; A: EDX data of all samples; B: EDX data of the alvikite hosted monazites; C: Typical monazite compositions (after Rosenblum & Fleischer 1995); D: Data from whole rock analysis (C and D are based on wt.%. Due to the similar weight of La, Ce and Nd, this is comparable with the mol.% of the EDX data in these ternary plots).

Abbildung 42: Verteilung der am häufigsten in Monazite eingebaute SEE; A: EDX-Daten von allen Proben; B: EDX Daten von Monaziten aus Alvikitproben; C: Typische Monazit Zusammensetzung (nach Rosenblum & Fleischer 1995); D: Geochemische Daten der Gesamtgesteinsanalyse (C und D basieren auf wt.%. Auf Grund der ähnlichen Atommasse von La, Ce und Nd sind diese ternären Diagramme vergleichbar mit den auf mol.% basierenden EDX-Daten).

Other often detected elements in the breccia samples are strontium and thorium (Tab. 10). While strontium was found in nearly all monazites, thorium was predominantly detected in breccia-hosted monazites, especially in monazite, which occur within cloudy accumulation textures. The occurrence of thorium-containing monazites is not correlating with the data from whole rock analysis.

The dependence of the frequency of monazites in the thin sections with the total amount of REE in the whole rock analyses is not verifiably. Alvikites show a weak trend, but no precise correlation between the occurrence of monazites and REE amount is ascertainable. In the breccia sections, the samples with the lowest proportion of clasts have the highest amount of REE. These are also the samples, which show a high density of monazites, but the varying matrix-to-clast ratio prevents a clear conclusion.

6.4.7 REE-fluorocarbonates

REE-fluorocarbonates are the second group, which contain a high amount of REE. They occur mainly in alvikite samples and additionally in breccia samples with grey matrix, especially in sample SES1.18. The mineral names of the REE-fluorocarbonate group are defined by their most common REE and by the relation of calcium to the REE with bastnaesite and synchisite as endmember (Tab. 11) (Meng et al. 2002).

In the majority of the alvikite sections, the REE-fluorocarbonates occur rarely and form clusters of euhedral, up to 10 µm long, sharp-tipped needles, which are grown secondary in cavities (Fig. 43 A). Only in two samples (SES1.8 and SES1.27), these clusters are bigger and occur more often. In the sample SES1.8, there are more needles per cluster, which are disposed closer (Fig. 43 B), while in SES1.28 only one aggregate per occurrence is recognizable, in which single needles have grown together.

Like mentioned above, in the breccia sections, the REE-fluorocarbonates occur only associated to a grey coloured matrix. With the exception of sample SES1.18, the REE-fluorocarbonates consist of spherical aggregates, which reach up to 20 µm and consist of needles, which are smaller, than those in the alvikite sections (Fig. 43 C).

The aggregates have a heterogeneous surface in the BSE-image, in which the single needles cannot kept apart due to the high density of their accumulation. Such REE-fluorocarbonates are located in the altered alumo-siliceous matrix and seem not to be bound to cavities as observed in the alvikite sections.

Table 10: Average amounts of REE, Sr and Th of the monazites sorted by rock types (EDX-data). Thorium was predominantly detected in breccia-hosted monazites.

Tabelle 10: Durchschnittliche Gehalte an SEE, Sr und Th der Monazite sortiert nach Lithotype (EDX-Daten). Thorium wurde vor allem in Monaziten aus Brekzienproben gemessen.

Lithotype	Meas. points	REE [%]		Strontium [%]		Thorium (> LOD) [%]		
		Average content	Std. deviation	Average content	Std. deviation	Readings > LOD	Average content	Std. deviation
Porphyry	**5**	**13.9**	**3.8**	**0.49**	**0.33**	**40**	**0.15**	**0.02**
Igneous breccia	**84**	**10.4**	**3.3**	**1.14**	**0.57**	**49**	**0.43**	**0.39**
Alvikite	**36**	**7.9**	**2.8**	**0.61**	**0.26**	**6**	**0.06**	**0.01**

Table 11: Classification of REE fluorocarbonates (MENG et al. 2002).

Tabelle 11: Klassifikation der SEE-Fluorokarbonate (MENG et al. 2002)

Ca / REE	Mineral	Formula
0	Bastnaesite-(Ce)	$Ce(CO_3)F$
	Bastnaesite-(La)	$La(CO_3)F$
	Bastnaesite-(Y)	$Y(CO_3)F$
0.5	Parisite-(Ce)	$Ca(Ce,La)_2(CO_3)_3F_2$
	Parisite-(Nd)	$Ca(Nd,Ce,La)_2(CO_3)_3F_2$
0.66	Röntgenite-(Ce)	$Ca_2(Ce,La)_3(CO_3)_5F_3$
1	Synchisite-(Ce)	$CaCe(CO_3)_2F$
	Synchisite-(Nd)	$CaNd(CO_3)_2F$
	Synchisite-(Y)	$CaY(CO_3)_2F$

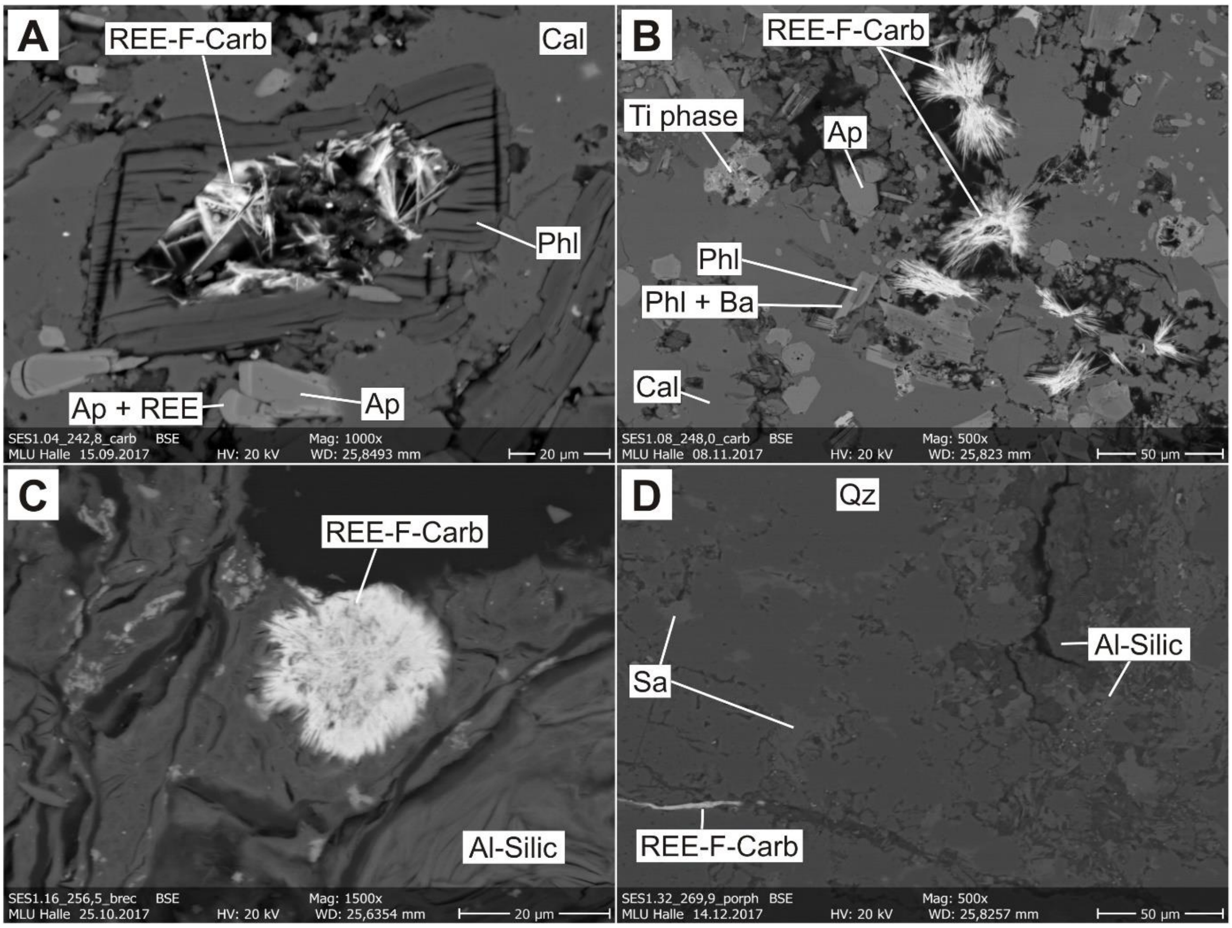

Figure 43: Typical REE-fluorocarbonate occurrences (SEM-BSE); A: Small needle-shaped crystals in cavity in alvikite section; B: Larger aggregates from the alvikite sample SES1.08; C: Typical aggregate from a breccia section with grey matrix; D: REE-fluorocarbonate vein in the porphyry section. The occurrence of the vein shows, that there was a small impregnation of the wall rock by the intrusion or hydrothermal fluids.

Abbildung 43: Typische Vorkommen von SEE-Fluorokarbonaten (SEM-BSE); A: Kleine nadelige Kristalle in Hohlraum in Alvikitbereich; B: Größere Aggregate auch der Alvikit-Probe SES1.08; C: Typische Aggregate in Brekzienbereichen mit grauer Matrix; D: SEE-Fluorokarbonat-Ader in porphyrischen Bereich. Das Auftreten der Ader zeigt, dass es eine kleine Imprägnation des Nebengesteins durch die Intrusion oder durch hydrothermale Fluide gab.

In one thin section (SES1.32) of porphyry samples, REE-fluorocarbonates were detected (Fig. 43 D). Indeed, these phases occur as veins, which is a hint, that there was an impregnation of the wall rock by the carbonatitic intrusion or late hydrothermal or supergene REE-rich fluids.

In the thin section of sample SES1.18 REE-fluorocarbonate aggregates occur, which are up to 300 µm in diameter. They are embedded in a calcitic matrix and apparently not related to cavities (Fig. 44). This intergrowth texture indicates, that the calcite is also a secondary phase as well as the matrix in the other breccia samples.

The crystals in this thin section show a zonation from bastnaesite with in the core area to synchisite composition in the outer crystal area. Due to the higher weight of the REE in comparison to calcium, the bastnaesite zone look brighter in the BSE-image than the synchisite zones, in which a part of the REE is substituted by calcium.

44 measurements on REE-fluorocarbonates have been carried out with the SEM-EDX. In all samples, cerium was the most common REE, but the ratio from calcium to REE is varying from 0.2 to 1.6. Therefore, compositionally he whole range from bastnaesite-(Ce) to synchisite-(Ce) exists (Fig 45). The large zoned crystals of sample SES1.18, where calcium-rich and calcium-poor parts could be observed separately, can be classified as bastnaesite-(Ce) and synchisite-(Ce).

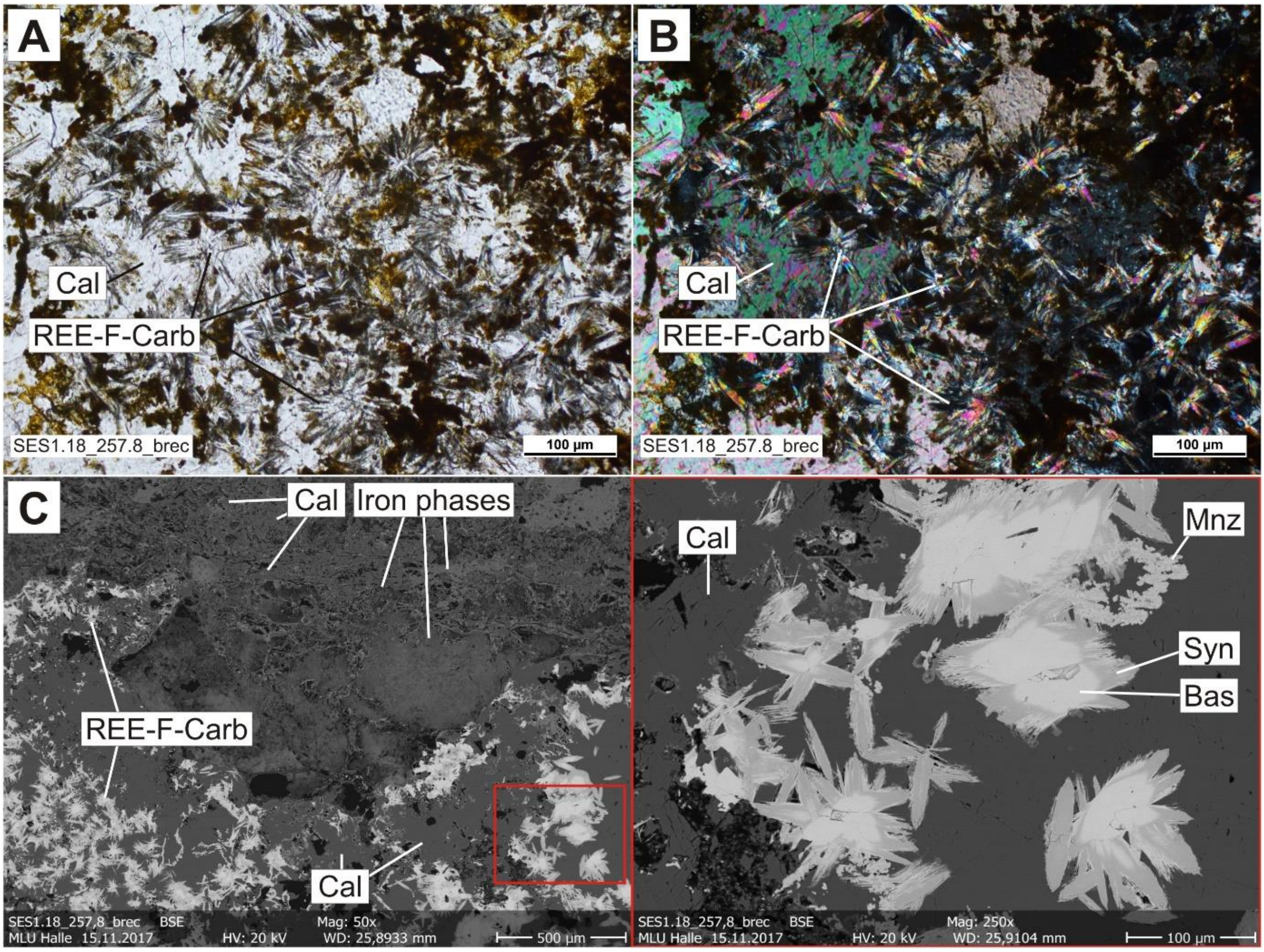

Figure 44: Large REE-fluorocarbonate crystals in the sample SES1.18 (A: optical microscopy; B: optical microscopy, crossed nicols; C: SEM-BSE). The zonation from a bastnaesite core to a synchisite rim is recognizable in the BSE-image.

Abbildung 44: Große SEE-Fluorokarbonat Kristalle in der Probe SES1.18 (A: Durchlichtmikroskopie; B: Durchlichtmikroskopie (gekreuzte Nicols); C: SEM-BSE). Die Zonierung von Bastnäsit im Kern zu Synchisit in den Randbereichen ist im BSE-image erkennbar.

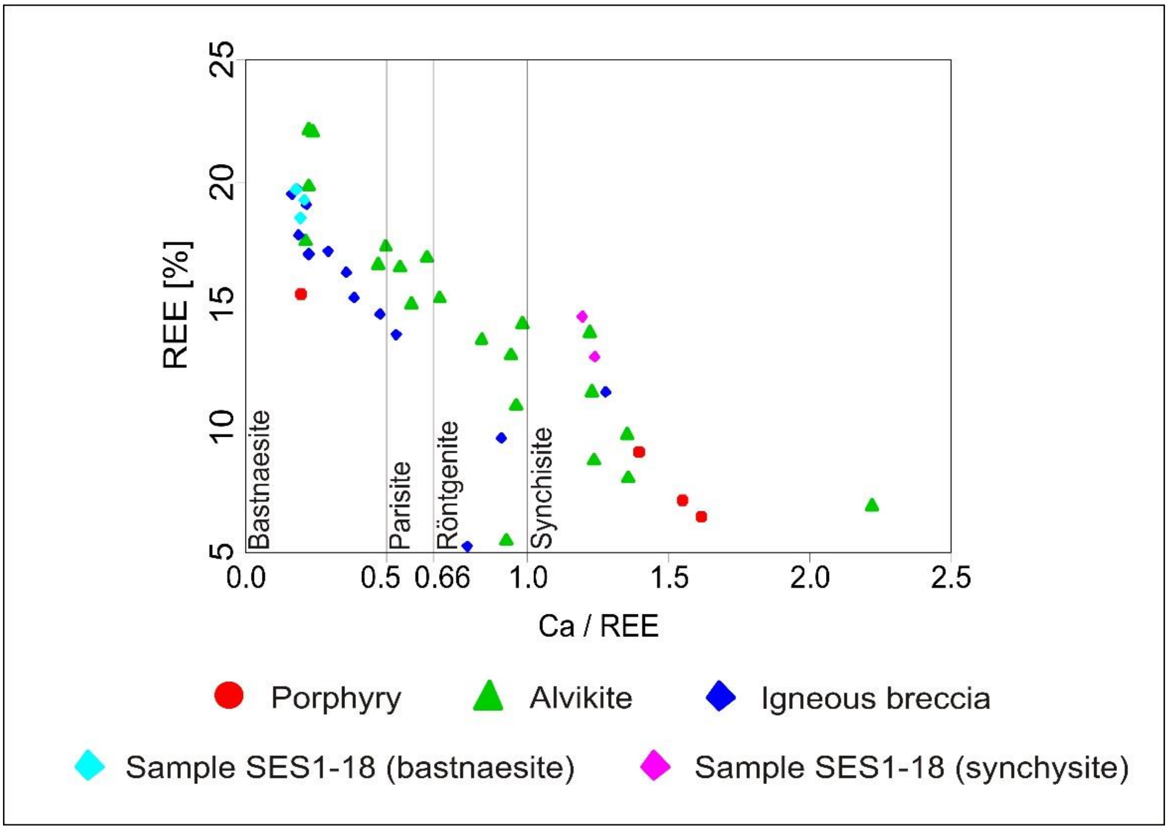

Figure 45: REE-Ca/REE plot for the categorization of the REE-fluorocarbonates (EDX-data). The measured crystals plot in the complete range of possible fields.

Abbildung 45: SEE-Ca/SEE-Diagramm zur Kategorisierung der SEE-Fluorokarbonate (EDX-Daten). Die gemessenen Kristalle plotten in die komplette Bandbreite der möglichen Felder.

The total amount of REE with approximately 15% (54 wt.%) is in average very similar to the content of the REE-fluorocarbonates from the breccia and alvikite sections, but individual minerals show variations from 10-22 % (25-65 wt.%). Especially in the alvikite sample SES1.27, the amount of REE in REE-fluorocarbonates is much higher than in the other alvikite section (Tab. 12). The distribution of the main REE (cerium, lanthanum and neodymium) is in the same dimension in comparison with monazites, but is varying a bit more. The measurements from alvikites are subjected to wider variations (Fig. 46).

Here again, the sample SES1.27 is standing out, because of an enormous enrichment of cerium. The REE-fluorocarbonate crystals contain in average 20 % (65 wt.%) cerium and only 0.5 (1.6%) lanthanum. The other alvikite-hosted minerals occur in two clusters with an average cerium to lanthanum ratio of 5-8 and 1.4-1.9. There is no correlation between the shape of the REE-fluorocarbonate crystals and their position in this ternary plot.

6.4.8 Nb-Zr-Ti-Ca-Oxides

By the use of the SEM-EDX-analysis, a couple of minerals were detected, which can be interpreted as oxides from various elements. There are the zirconium-rich, the niobium-rich and the titanium-rich oxides, in which all measured phases contain at least low amounts of these three elements and additionally calcium. Three subgroups can be clearly distinguished by their EDX-data (Fig. 47).

The zirconium-rich oxides can be identified easily as zirconolite, because of their composition and their shape showing mostly twinning euhedral crystals (chapter 6.4.8.1). Minerals of the three groups can contain low amounts of REE.

The niobium rich oxides can be easily classified as pyrochlore, which are described more detailed in section 6.4.8.2. The titanium oxides can also belong to pyrochlore group or represent different titanium oxides. Here, especially the amount of calcium is varying in a wider range than for the niobium-rich oxides. The amount of zirconium in both subgroups is mostly low, but detectable. This may also be a hint that both phases and the zirconolites belong to the same mineral supergroup.

Table 12: Average REE and fluorine contents of the different REE-fluorocarbonate types (EDX-data). The measurements, carried out in thin section SES1.27 show a completely different composition.

Tabelle 12: Durchschnittliche Gehalte an SEE und Fluor in den verschiedenen Vorkommen von SEE-Fluorokarbonaten (EDX-Daten). Die Messungen von Kristallen in Dünnschliff SES1.27 zeigen eine stark abweichende Zusammensetzung.

		REEs [%]		Fluorine [%]	
Lithotype	Measured points	Average content	Std. deviation	Average content	Std. deviation
Porphyry	4	9,5	3.6	9.6	1.7
Igneous breccia	19	15.9	3.8	13.8	4.4
Alvikite	21	14.1	4.6	9.9	3.6
Alvikite without SES1.27	17	12.6	3.6	9.4	3.8
SES1.27	4	20.4	1.8	12.2	4.4

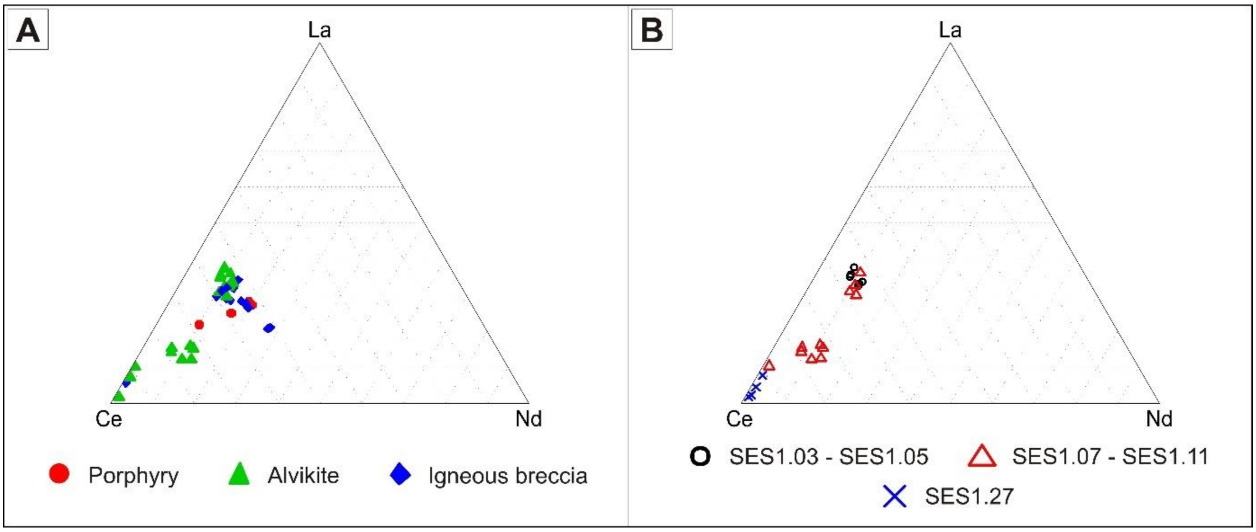

Figure 46: Distribution of the most common REE (EDX data); A: All samples; B: Alvikite hosted REE-fluorocarbonates. The measured crystals of SES1.27 show high amount of cerium.

Abbildung 46: Verteilung der am häufigsten eingebauten SEE (EDX-Daten); A: Alle Proben; B: SEE-Fluorokarbonate aus Alvikitproben. Die gemessenen Kristalle von Schliff SES1.27 besitzen hohe Gehalte an Cer.

6.4.8.1 Zirconolite

The zirconium-rich oxides were classified as zirconolites (**$CaZrTi_2O_7$**), which can easily be confused with zirkelite, which has the same chemical composition and possess a cubic crystal system, while zirconolite is an umbrella term for all other occurring minerals with the same sum formula but various crystal systems, especially monoclinic (BAYLISS 1989). The different mineral phases cannot be distinguished by EDX-data, but there are some differences, in their crystal shape and colour. While zirconolites have yellowish or dark brown to opaque coloured prismatic crystals, zirkelites have reddish or dark brown to opaque colour and their habit of euhedral crystals is octahedral. Furthermore, metamict alteration is typical for zirconolite (MELGAREJO & MARTIN 2011). Based on these differences, a part of the minerals can clearly identified as zirconolite. For the other remaining minerals, where a classification is not possible, zirconolite was also used as a general term.

Zirconolite occurs only in the alvikite sections where it is the main zirconium-bearing phase. Often, the crystals are euhedral to subhedral with prismatic habitus and twinning (Fig. 48). The size of these crystals varies from 15 to 150 µm. Some detected minerals occurred as small anhedral grains. Nearly all detected zirconolites are overgrown with pyrochlore predominantly on the end face of the tabular crystals.

This paragenesis occurs in a wide range of pyrochlore-zirconolite ratios. There are large zirconolites with a small pyrochlore covering as well as small zirconolite grains located in larger pyrochlore crystals.

24 analyses of zirconolites were made using the SEM-EDX. Apart from the major elements calcium, titanium and zirconium, also some other elements could be detected. Especially iron and thorium occur in all measured minerals. Niobium, yttrium and REE were also present in some zirconolites in small amounts (Tab. 13).

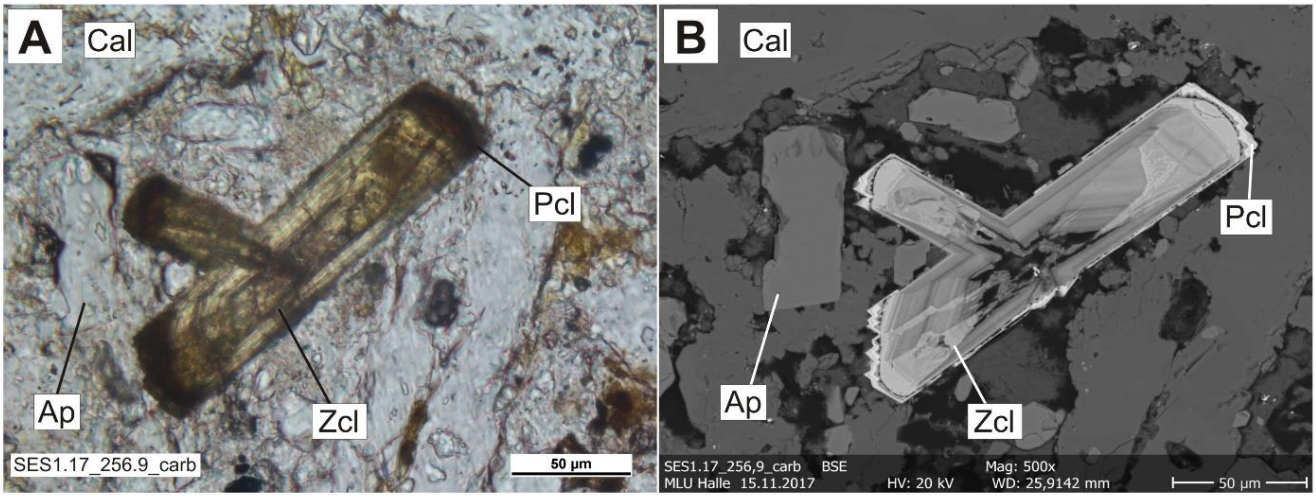

Figure 47: Euhedral zirconolite crystal overgrown by pyrochlore (A: optical microscopy; B: SEM-BSE).

Abbildung 47: Idiomorpher Zirkonolith-Kristall, mit Phyrochlor umwachsen (A: Durchlichtmikroskopie; B: SEM-BSE)

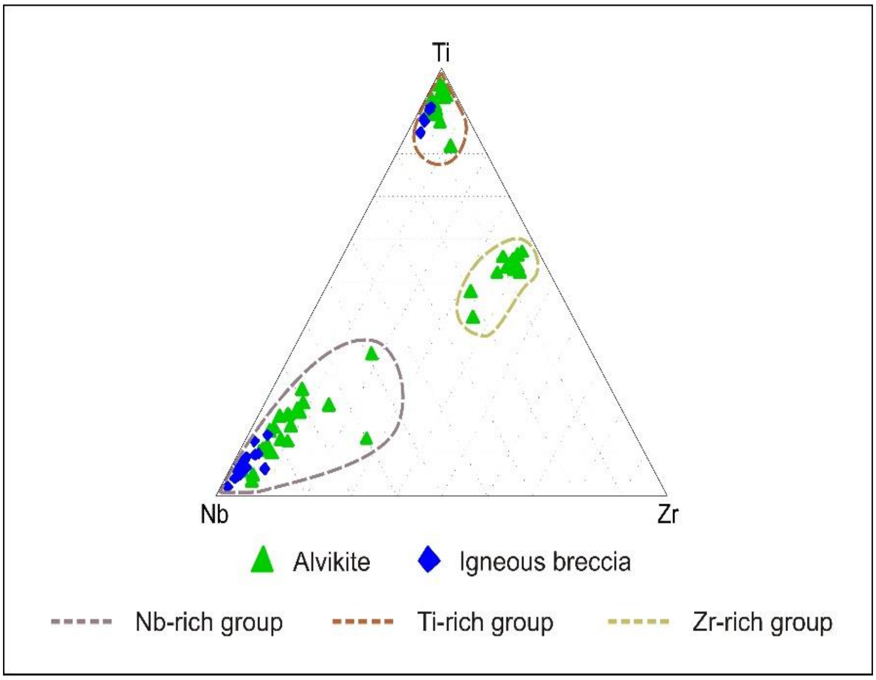

Figure 48: Distinction of the three Nb-Zr-Ti-oxides subgroups. The separation of the minerals by their main oxides is clearly visible

Abbildung 48: Unterscheidung der drei Nb-Zr-Ti-Oxide Untergruppen. Die Unterteilung der Minerale nach ihrer Hauptoxide ist deutlich erkennbar.

Table 13: Average composition of zirconolites (EDX-data, n=24).

Tabelle 13: Durchschnittliche Zusammensetzung der Zirkonolithe (EDX-Daten, n=24)

Element	Readings > LOD [%]	Average content [%]	Std. deviation [%]
Calcium	100	8.39	0.73
Titanium	100	14.20	1.36
Zirconium	100	10.57	1.38
Thorium	100	0.26	0.09
Iron	100	3.09	0.77
Niobium	54	0.38	0.11
Yttrium	50	2.07	0.88
REEs	33	0.16	0.07

6.4.8.2 Pyrochlore

The niobium rich oxides are classified as a member of the pyrochlore supergroup and because of the high amounts of niobium, these minerals are classified as pyrochlore (ATENCIO et al. 2010). The general formula of pyrochlore is: **$(Ca,Na)_2Nb_2O_6(OH,F)$** (MELGAREJO & MARTIN 2011).

Pyrochlore minerals were found in the alvikite section as well as in the igneous breccias. In the alvikite sections, the majority of the crystals occur in a paragenesis with zirconolite, in which they overgrow zirconolite as a reaction rim (Fig. 49 A,B). These crystals are euhedral to subhedral and 5-50 µm in diameter. In some cases, only the euhedral pyrochlore crystal is visible, which has a small altered area in the centre indicating the former presence of zirconolite. Most pyrochlore minerals in the alvikite sections have a zonation, which is to filigree, to detect differences by means of the EDX-analysis.

The pyrochlore crystals in the breccia sections are generally larger than in the alvikite sections, and show mostly anhedral, partially fractured phenocrysts that have no zonation (Fig. 49 C,D). Only a few euhedral to subhedral crystals were detected, which also show no signs of zonation. Some minerals are partially dissolved and replace by other phases like secondary apatite. Pyrochlore minerals are the main niobium-bearing phases and contain in average 13-18 % (32-42 wt.%) niobium. Their amount is a slightly higher in the breccia sections, than in the alvikites. Beside calcium and niobium, also a couple of other elements like titanium, iron, sodium, zirconium, strontium and REE were detected. Especially sodium occurs in a relative high amount of 3.2 % in the alvikite-hosted and 7.7 % in the breccia-hosted pyrochlore crystals. REE occur mainly in the alvikite-hosted pyrochlore, in which the amount is approximately 3 % in average (Tab. 14).

6.4.8.3 Titanium oxides

The titanium-rich oxides include a couple of secondary minerals or phases, in which titanium is the main element. Anhedral heterogeneous aggregates with a size of 5-15 µm were observed in the alvikite sections. They contain REE enriched speckles, which can be clearly identified by their bright colour in the BSE-image (Fig. 50 A).

Furthermore, there are phases, which are associated to altered magnetites occurring in the alvikites as well as in the igneous breccias. These have nearly the same chemical composition as the aggregates mentioned above and replace dissolved magnetite (Fig. 50 B).

The classification of these titanium oxides is difficult. A couple of other possible cations like calcium, niobium, zirconium, iron and REE were detected with the EDX-analysis. These elements occur in low amounts of less than 4 % (Tab. 15). Potential phases could be simple titanium oxide minerals like rutile, anatase or brookite. Especially rutile incorporates a variety of other cations like zirconium and niobium (MELGAREJO & MARTIN 2011). The association to magnetite indicates an alteration of magnetite to ilmenite, but therefore, the amount of iron is too low.

The occurrence of calcium, niobium, zirconium and titanium in one mineral can also be interpreted, to be a member of the pyrochlore supergroup, where betafite is a possible titanium rich mineral (ČERNÝ & ERCIT 1989) (Fig. 51). Perovskite (**$CaTiO_3$**) is another possible calcium-titanium oxide, which is common in carbonatites, but normally contains higher amounts of calcium (ČERNÝ & ERCIT 1989).

Table 14: Average composition of pyrochlores (EDX-data).

Tabelle 14: Durchschnittliche Zusammensetzung der Pyrochlore (EDX-Daten)

Element	Alvikite (n=24) [%]			Igneous breccia (n=27) [%]		
	Readings > LOD	Average content	Std. deviation	Readings > LOD	Average content	Std. deviation
Calcium	100	10.19	2.64	100	9.85	1,80
Niobium	100	13.69	2.79	100	17.65	2,95
Titanium	96	2.68	1.22	100	1.41	0,55
Iron	100	2.24	2.59	78	1.17	1,28
Sodium	88	3.23	1.57	100	7.69	1,92
Zirconium	92	1.46	1.02	78	0.55	0,24
REEs	96	2.92	1.16	89	0.33	0,23
Strontium	50	0.54	0.22	93	0.96	0,35
Yttrium	50	0.43	0.09	22	0.18	0,06
Thorium	33	0.25	0.20	37	0.38	0,22
Uranium	50	0.34	0.15	19	0.83	0,40
Lead	42	1.57	0.97	7	0.66	0,01

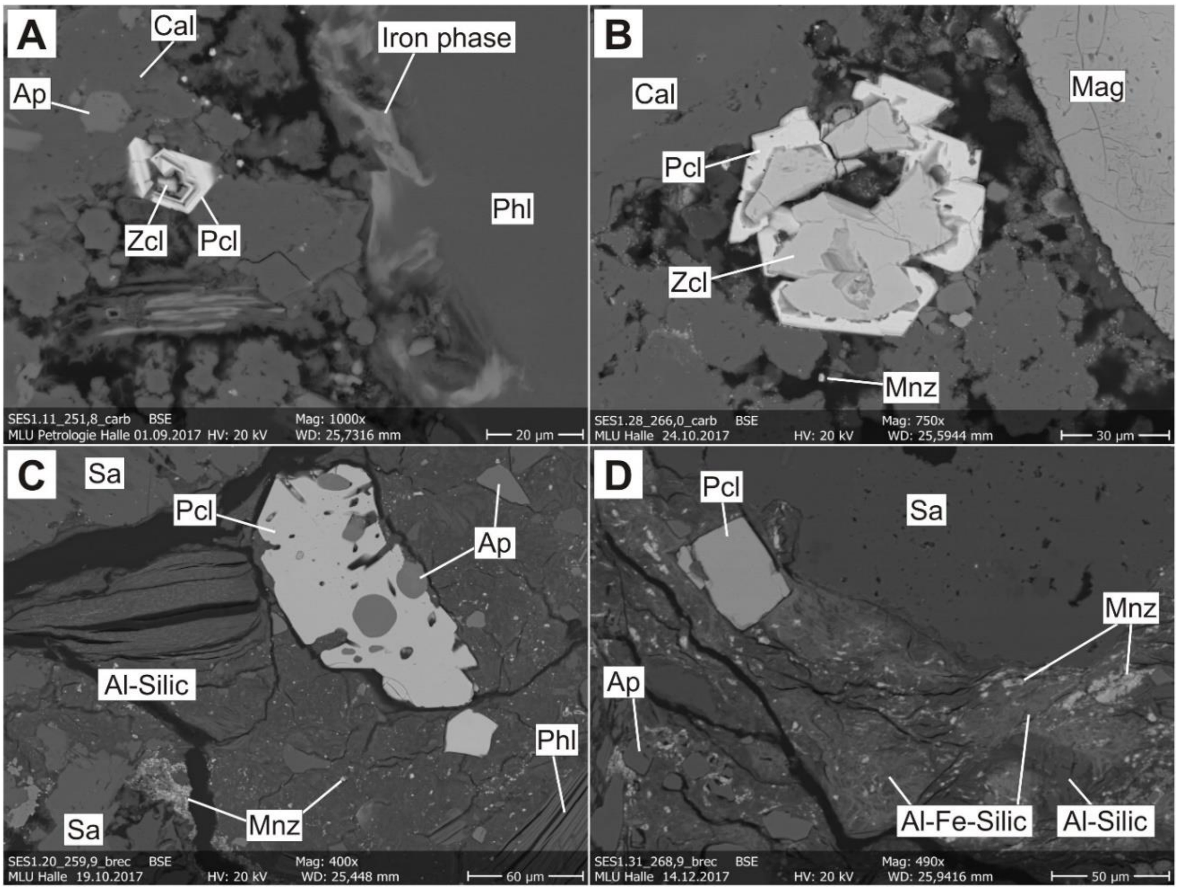

Figure 49: Examples of pyrochlore crystals (SEM-BSE); A,B: Pyrochlore surrounding zirconolite in alvikite sections; C: Anhedral pyrochlore crystal in breccia sections intergrown with apatite; D: Euhedral and broken pyrochlore crystal in breccia section.

Abbildung 49: Beispiele für Pyrochlorkristalle (SEM-BSE); A,B: Pyrochlore, um Zirkonolith gewachsen, in Alvikitbereichen; C: Xenomorpher Pyrochlorkristall in Brekzienbereich, verwachsen mit Apatit; D: Idiomorpher und zerbrochener Pyrochlor in Brekzienbereich

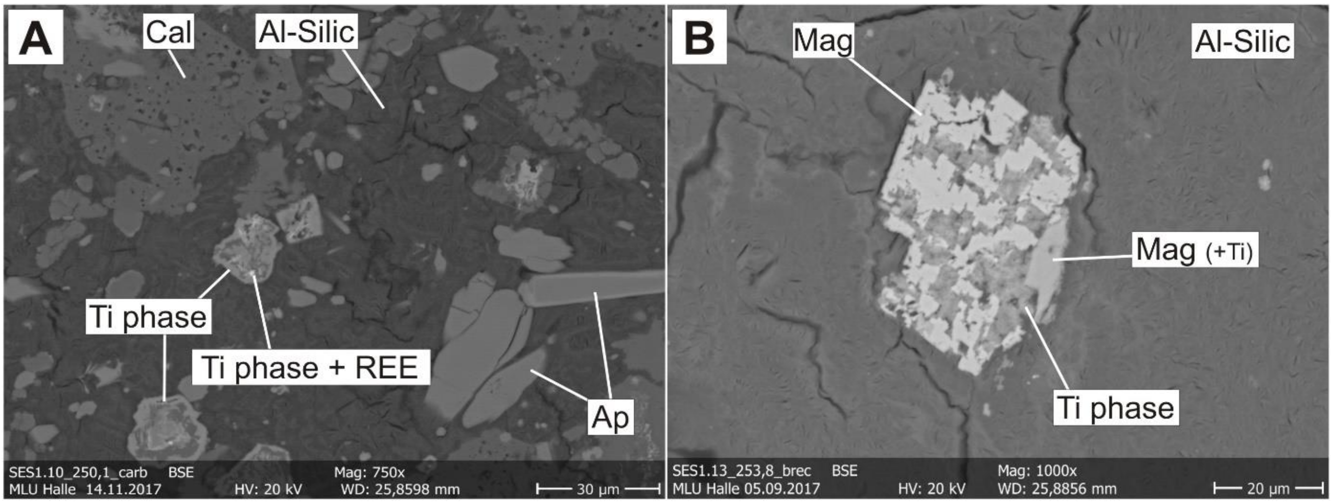

Figure 50: Examples for Ti-oxides; A: Secondary Ti-phase in alvikite section with REE enriched speckles; B: Ti-phase in breccia section as a replacement of magnetite.

Abbildung 50: Beispiele für Ti-Oxide; A: Sekundäre Ti-Phase in Alvikitbereich mit SEE-angereicherten Sprenkeln; B: Ti-Phase in Brekzienbereich als eine Substitution von Magnetit

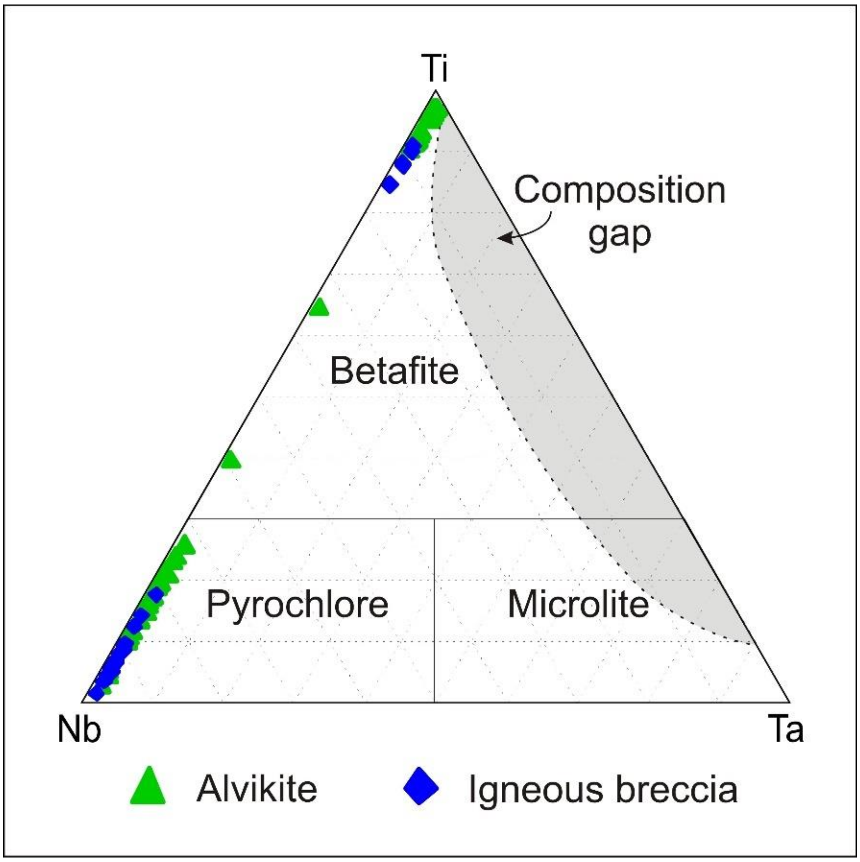

Figure 51: Ternary plot for the classification of members of the pyrochlore supergroup. The crystals classified as pyrochlore (chapter 6.4.8) plot in the pyrochlore field, while the titanium-rich oxides plot in the betafite field (after Černý & Ercit 1989 and Melgarejo & Martin 2011).

Abbildung 51: Ternärer Plot zur Klassifikation von Vertretern der Pyrochlor-Supergruppe. Die Kristalle, die als Pyrochlor klassifiziert wurden (Kapitel 6.4.8) plotten in das Pyrochlor-Feld, während die Ti-reichen Oxide in das Betafit-Feld plotten (nach Černý & Ercit 1989 und Melgarejo & Martin 2011)

Table 15: Average composition of Ti-oxides (EDX-data).

Tabelle 15: Durchschnittliche Zusammensetzung der Ti-Oxide (EDX-Daten)

Element	Alvikite (n=23) [%]			Igneous breccia (n=5) [%]		
	Readings > LOD	Average content	Std. deviation	Readings > LOD	Average content	Std. deviation
Calcium	100	3.87	3.99	100	0.47	0.16
Titanium	100	20.10	6.92	100	17.10	4.75
Niobium	100	1.48	1.70	100	2.10	0.98
Iron	100	1.91	0.81	100	3.63	2.20
Zirconium	91	0.79	0.65	100	0.20	0.06
REEs	65	2.38	1.86	0	-	-

6.4.9 Baddeleyite

Baddeleyite (**ZrO_2**) is a mineral, which was only detected in the breccia sections and represents the only zirconium-bearing mineral, except accessory zircons occurring in the porphyritic clasts. Baddeleyite is a typical accessory mineral in carbonatites, were it is one of the early crystallizing minerals (CHAKHMOURADIAN 2006). It is stable over a wide range of temperature and pressure conditions of the upper mantle and lower crust. During the late stage intrusion of carbonatitic melts, the baddeleyite can be replaced by zirconolite (LUMPKIN 1999), what is the cause, that no baddeleyite was found in the alvikite sections.

The baddeleyite crystals in the breccias are anhedral, partially broken fragments of phenocrysts (Fig. 52). The majority of the detected crystals were 15-100 µm in size, but there are also single crystals, that reach a size up to 500 µm.

The occurrences of baddeleyite are randomly and too rare to deduce a statement about the quantity in the single thin section. If no baddeleyite was detected in a sample, it does not mean, that the sample does not contain it. Twelve baddeleyite crystals could be measured by EDX analysis. The amount of zirconium is in average 33% (71 wt.%), what is exact the expected amount, which results from its stoichiometric formula. Yttrium and strontium were detected in some crystals with lower amounts of approximately 1 % (Tab. 16).

6.4.10 Other rare minerals

The minerals in this chapter were only detected occasionally. Although these phases are too rare for a statistical evaluation, their occurrence gives hints on the environment, in which they were formed and/or altered.

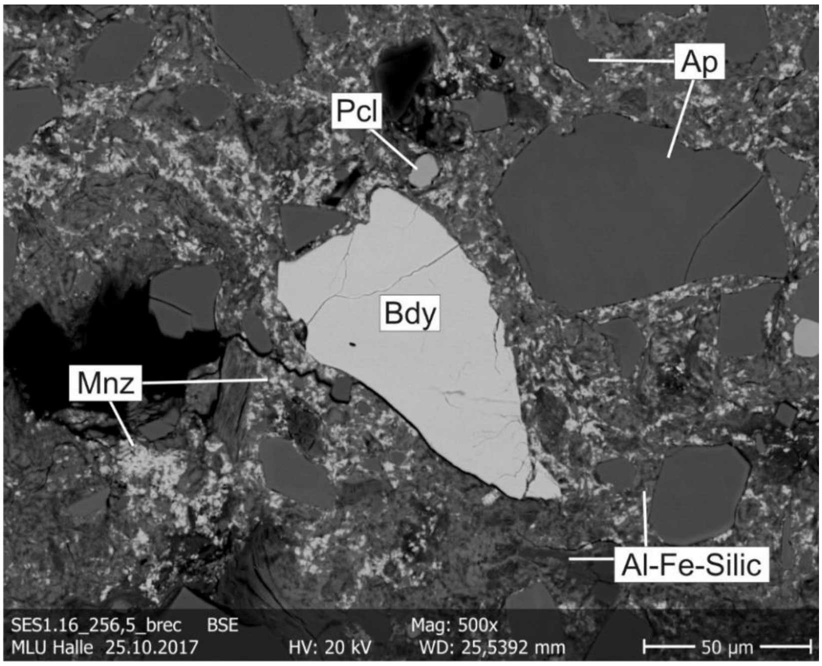

Figure 52: Baddeleyite fragment in breccia section (SEM-BSE).

Abbildung 52: Baddeleyit Fragment in Brekzienprobe (SEM-BSE)

Table 16: Average composition of the baddeleyites (EDX-data, n=12).

Tabelle 16: Durchschnittliche Zusammensetzung der Baddeleyite (EDX-Daten, n= 12)

Element	Readings > LOD [%]	Average content [%]	Std. deviation [%]
Zirconium	100	33.18	5.35
Yttrium	45	1.16	0.31
Strontium	36	1.01	0.46

6.4.10.1 Barite

Apart from the barium-enriched rims of some phlogopite crystals, barite is the major barium-bearing phase in the samples. Barite is typically associated to hydrothermal vein type and exhalative deposits, where it is formed at low temperature by mesothermal or epithermal fluids (Rösler 1991). The occurrence of barite in thin sections correlates with the total amount of barium in the whole rock analysis. It occurs only linked to altered sections and cavities, so the majority of the occurrences are finely distributed anhedral crystals (Fig. 53 A). Additionally, in some breccia sections large subhedral crystals occur, which can be fragmented and reach a size of up to 100 µm (Fig. 53 B).

Nine barite crystals were measured with the EDX and contain in average 13 % (50 wt.%.) barium. Beside barium and sulphur (13 %), the barites are also containing smaller amounts (<1 %) of strontium.

Barite veins also occur in the porphyry and the porphyritic clasts of the breccia, but there were no links between the occurrences in the different rock types detected. That is why it cannot be differentiated, whether different barite types were formed at the same or two different events.

6.4.10.2 Uranophane

Uranophane was only detected in the alvikite samples SES1.08 and SES1.10. The thin section of SES1.08 contains an oxidation horizon, where some uranophane occurs in a small iron leached zone. In SES1.10, uranophane is located at the transition between two different alvikite units. This indicates, that a special environment is necessary for the formation of uranophane, which seems to be limited to small areas. The occurrence of uranophane is not correlating with the total amount of uranium in the samples, but this can be caused by the rare detection of uranophane. Uranophane typically occurs in oxidised zones of uranium deposits, where it is described as a weathering product of uraninite (Plášil 2017). However, there are also carbonatites, in which the occurrence of uranophane is described (Peterson et al. 2011). The detected uranophane minerals represent anhedral aggregates, which are grown in cavities (Fig. 54).

The size of these aggregates is up to 20 µm. According to EDX-data (n=5), the amount of uranium and silicon is in average at 10 %, while the amount of calcium is slightly lower. Furthermore, it were low amounts of phosphorus (1-5 %) and yttrium (1-3 %) detected.

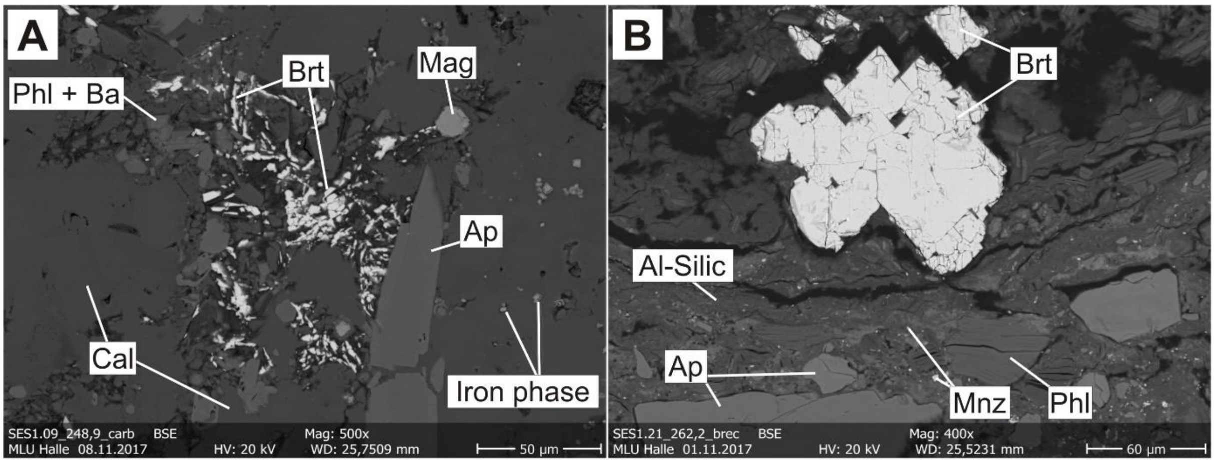

Figure 53: Occurrence of barite in an alvikite sample (A) and a breccia sample (B) (SEM-BSE). The crystals are linked to cavities and altered areas.

Abbildung 53: Auftreten von Baryt in einer Alvikitprobe (A) und einer Brekzienprobe (B) (SEM-BSE). Die Kristalle sind an Hohlräume und alterierte Bereiche gebunden.

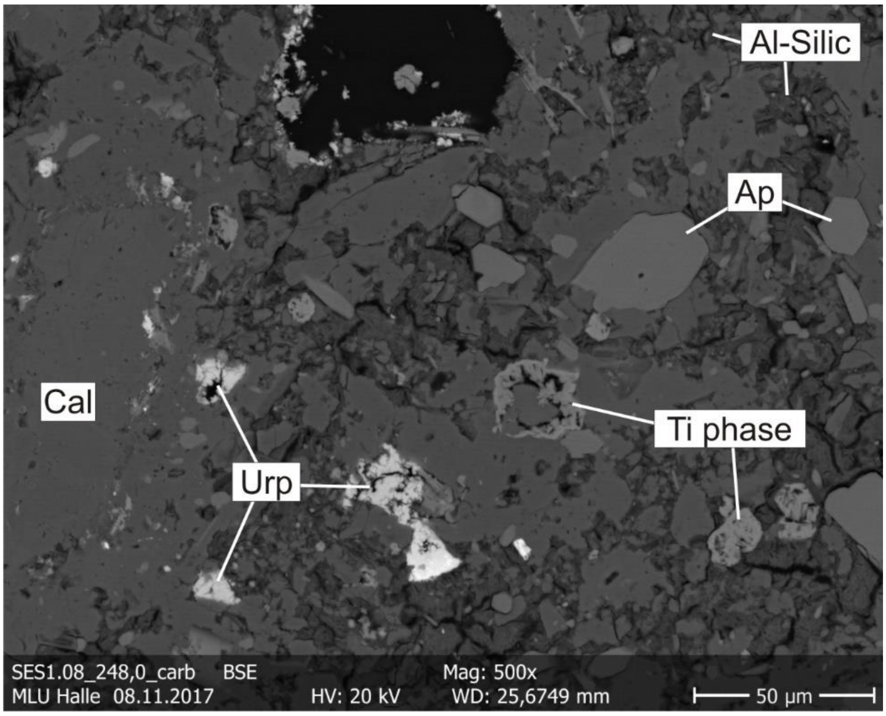

Figure 54: Uranophane in cavities in the iron leached part of alvikite sample SES1.08, which contains an oxidation front (SEM-BSE).

Abbildung 54: Uranophan in Hohlräumen in einem an Eisen gebleichten Teil der Alvikitprobe SES1.08; welche eine Oxidationsfront beinhaltet (SEM-BSE)

6.4.10.3 Sulphides

Sulphides were found very rarely. In total, six chalcopyrites, three pyrites, two sphalerites and one galena were detected. The sulphides are mostly tiny, just a few micrometres in diameter, anhedral (sometimes subhedral) grains, which are located in cavities as well as in the matrix of the alvikites or breccia sections (Fig. 55 A). The small size of the grains prevents a precise EDX-measurement, so that a sulphide grain surrounded by calcite can contain up to 10 % calcium in the EDX-analysis. The second type of detected sulphides is bound to areas, in which also uranophane was detected. In these areas, up to 25 µm large euhedral to subhedral pyrite crystals occur, which have been altered and partially dissolved (Fig. 55 B).

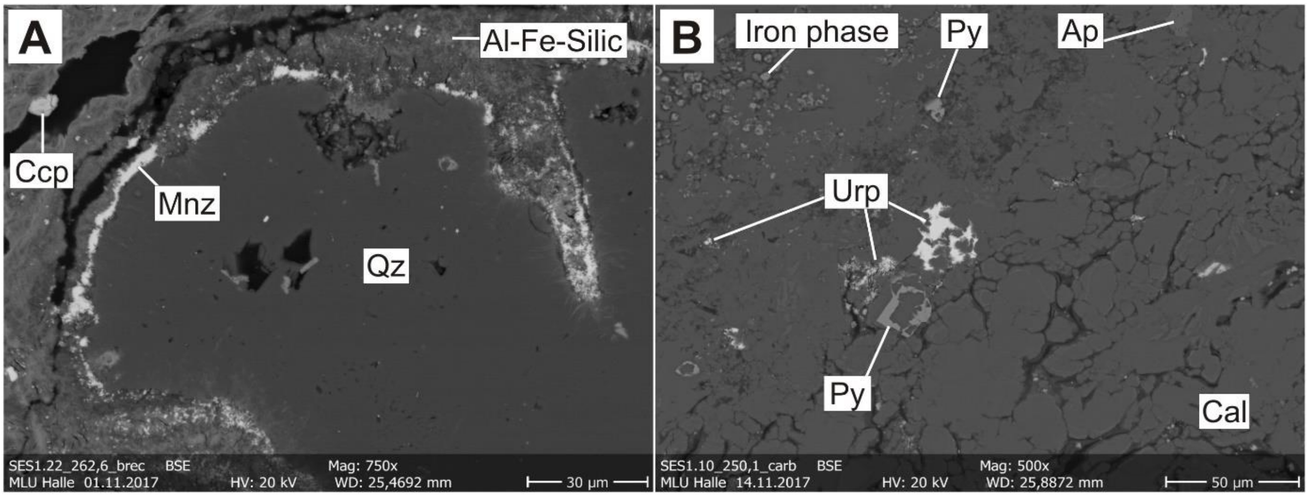

Figure 55: Examples for sulphides; A: Chalcopyrite grain in breccia sample; B: partially dissolved pyrite in a uranophane-containing area (SEM-EDX).

Abbildung 55: Beispiele für Sulfide; A: Chalkopyrit Korn in Brekzienprobe; B: Teilweise aufgelöster Pyrit in einem Uranophan haltigen Abschnitt.

6.5 Reflectance spectroscopy

The “near infra-red” and “shortwave infra-red” (NIR and SWIR) reflectance spectroscopy is a capable method for the identification of dominating iron phases and clay minerals.

Spectra that show a broad and round absorption band in the wavelength range of 850-980 nm indicate a mineral phase with substantial portion of trivalent iron. Regarding the presence of iron oxi-hydroxides, an absorption minimum located between 850 and 900 nm indicates that the sample contains predominantly hematite. If this feature is located between 900 and 980 nm, the sample is goethite dominated. The more the absorption minimum shifts to 900 nm, the more it represents a mixture of both iron phases. A further absorption feature is located at 1412-1413 nm that is a general absorption band of clay minerals and indicated hydroxyl water. Commonly, clay minerals show a characteristic absorption band between 2200 nm and 2400 nm, which is attributed to the vibrational overtone mode of a metal-hydroxyl complex in the octahedral-layer. Sample of porphyry and Igneous breccia show a sharp asymmetric band at 2205-2212 nm that is characteristic for montmorillonite caused by Al-OH. The reflectance feature for molecular water is situated at 1906. Another reflectance minimum, which was detected in some samples is located from 2232-2237 nm and is caused by a not clearly determinable clay mineral. This absorption feature could be caused by a member of the smectite or chlorite group, while many phyllosilicates like illite, kaolinite, muscovite, biotite or lepidolite can be excluded. The absorption band located at 2329-2339 nm mainly occurs in spectra of alvikite samples is caused by the vibration of a calcium-oxygen-complex in calcite minerals, why it can be distinguished clearly from other carbonates like dolomite or ankerite. Some of the samples, especially intrusive breccia show a weak absorption band at 2229-2239 nm, which probably belongs to chlorite (HAUFF 2005).

With the reflectance spectroscopy, it is only possible to detect major mineral phases, thus rare earth minerals like monazite or the REE-fluorocarbonates cannot be determined, because of their low quantity. Monazite and the REE-fluorocarbonates have a number of sharp significant absorption bands in the NIR, but none of these have been detected.

Absorption spectra of the different rock types are shown in figure 56 and the determined absorption features are listed in table 17. Decisive for the interpretation is only the relative size of the absorption features in the respective spectrum. The absolute reflectance of a sample is an expression its reflected energy generally, which is variating by different parameters, e.g. roughness of the sample. Therefore, the powdered samples have more pronounced absolute absorption bands than rock samples, on which the measurement was carried out on the surface. The relative depth of the reflectance/absorption features is in both cases the same.

In spectra of the porphyry section, the trivalent iron absorption band is dominated by goethite, but is also influenced significantly by the occurrence of hematite. The absorption band at 2208 nm, generally formed by clay minerals, is deep and symmetrical, which is caused by montmorillonite and thus, represents the major clay mineral determined in the porphyry rock. A very weak absorption feature at 2250 nm originates probably from Fe-OH-molecule vibration in chlorite. Spectral data of the joints occurring in the porphyry show the same infrared-active mineral phases except for the iron phase, which is more dominated by hematite.

The breccias have a high amount of clay minerals, which is mostly represented by montmorillonite. Only in the breccias with grey matrix and some breccias with low contents of clasts, a second clay mineral of the smectite group occurs, which could not closer determined. Hematite is the dominating iron phase in the breccias with red matrix, while predominantly goethite occurs in all other samples. Additionally, the spectra of the breccias contain a weak carbonate absorption at 2335 nm, which is the characteristic wavelength for calcite (Ca-C-O-bond).

In the alvikite sections, the general absorption band for clay minerals is much weaker developed than in the spectra of the other lithotypes. Consequently, a precise identification of clay minerals was not possible. Calcite bands dominate the spectra of the alvikites. Iron occurs dominantly as goethite in sections with brownish and greyish matrix and as hematite in the reddish areas.

Table 17: Measured reflectance features and their occurrence. Dots in brackets are minor phases.

Tabelle 17: Gemessene Reflektanzbanden und ihr Auftreten. Punkte in Klammern sind Nebenphasen.

Wavelength [nm]	Mineral	Porphyry		Breccia				Alvikite		
		Rock	Joint	Red m.	Beige m.	Beige m.*	Grey m.	Grey. m.	Red. m.	Brow. m.
850-900	Hematite (dominating iron phase)		●	●					●	
900-980	Goethite (dominating iron phase)	(●)			●	●	●	●		●
1412-1414	Clay minerals	●	●	●	●	●	●	(●)	(●)	(●)
1904-1908	Molecular water	●	●	●	●	●	●	●	●	●
2205-2212	Montmorillonite	●	●	●	●	(●)	●			
2232-2237	Clay minerals					●	(●)			
2329-2339	Calcite							●	●	●
2354-2359	(Chlorite)	●	●							

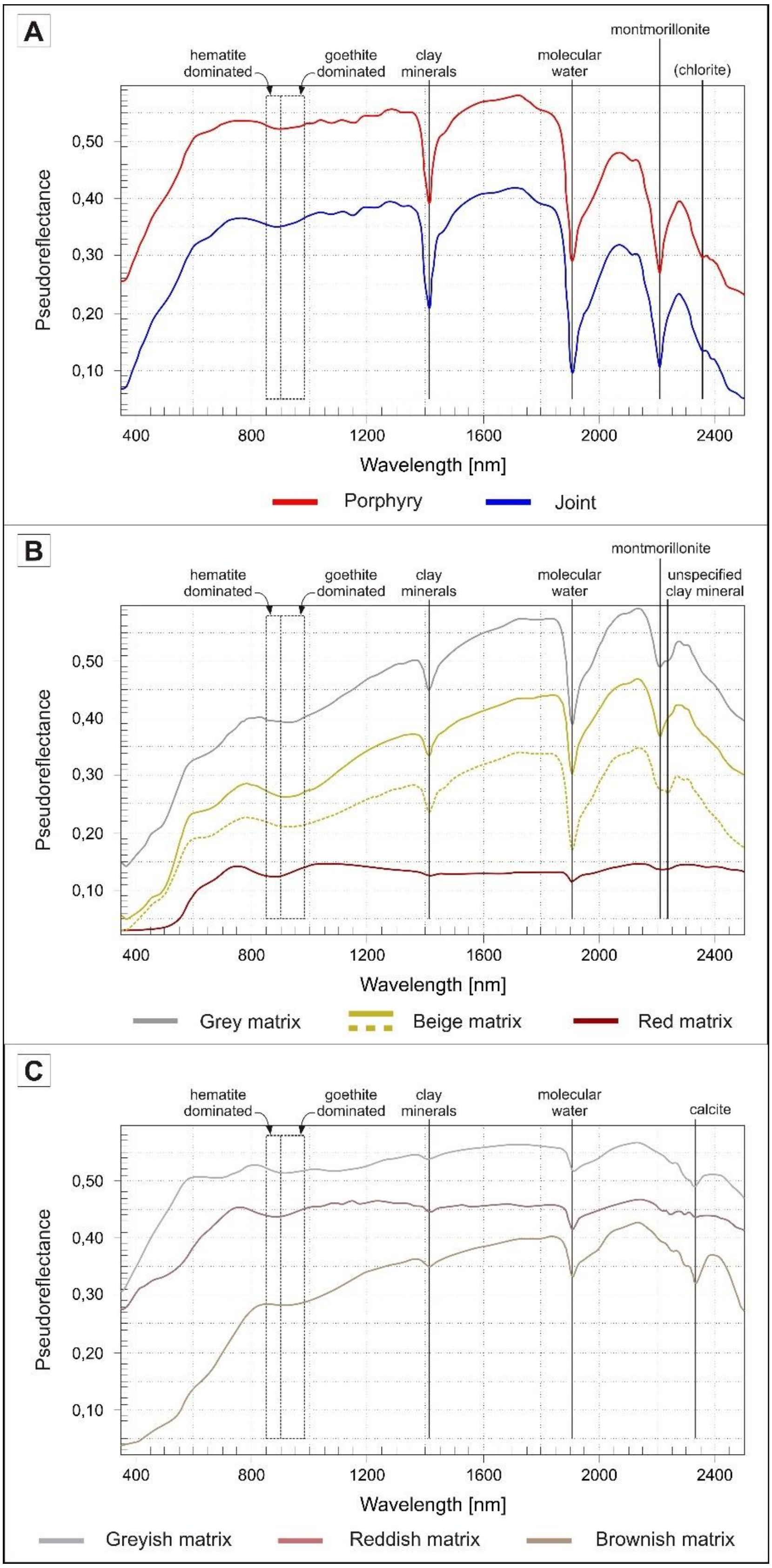

Figure 56: Average reflectance spectra of the different lithotypes; A: Porphyry; B: Igneous breccia (the dotted line is the group of beige breccias with minor clasts); C: Alvikites.

Abbildung 56: Durchschnittliche Reflektanzsprektren der verschiedenen Lithotypen; A: Porphyre; B: Magmatische Brekzie (die gepunktete Linie ist die Gruppe der klastenarmen Brekzien mit beiger Matrix; C: Alvikite

7. Discussion

How does the geochemistry of the mineralisation can be summarized?

A REE-mineralisation (including associated elements like niobium) was determined in the drill core section. This includes the alvikite veins and the matrix of the igneous breccias. Especially the LREE occur in average with 50 times higher amounts, than in the upper continental crust. The amount of niobium is even 100 times higher. In total, the mineralised areas have up to 1.2 % **REE_2O_3**. The amount of niobium can only be estimated because of the maximum detection limit of the ICP-MS and can be up to 0.2 % in the breccia sections. The quantity of the mineralisation is mainly correlating with the proportion of the matrix.

The amounts of barium, strontium, uranium and thorium are also higher in the mineralised sections, but varying in a wide range, which is not correlating with the REE-mineralisation.

Compared to deeper sections of the Storkwitz body, only a few elements with divergent concentrations were analysed. The REE are nearly equal distributed and the ratio between LREE and HREE is similar.

How does the mineralogy of the mineralisation can be summarized?

All detected phases and minerals are sorted according to the samples, in which they occur in the table 18 for the breccia samples and table 19 for the alvikite samples.

Figure 57 shows the distribution of some minerals, which characterize the mineralisation and/or give indications for alteration processes. The REE-mineralisation is predominantly characterized by secondary phases, especially monazite and REE-fluorocarbonates. Remarkable is, that the REE-fluorocarbonates only occur in alvikites and breccia sections with grey matrix. Monazite is the most detected REE-bearing mineral and occurs fine disseminated as tiny crystals in the matrix and in breccia samples. Additionally, monazite occurs accumulated as replacement texture or as corona texture around quartz clasts. Apatites in general have low contents of REE, but in some sections, especially alvikite section, REE-enriched apatite rims are recognizable.

Pyrochlore, the main niobium-bearing phase, occurs also in different shapes in the breccia and alvikite samples. The breccia-hosted pyrochlores are mainly anhedral phenocryst fragments, while the alvikite-hosted pyrochlores are mainly euhedral, overgrowing zirconolite and show a zonation. Zirconolite is the only detected zirconium-bearing phase in alvikite sections, while in the breccias only baddeleyite phenocrysts occur. The dominating iron phase is, according to the macroscopic observation, hematite that dominates the red/reddish coloured sections, while goethite predominantly occurs in the remaining part of the drill core.

Except of a small REE-fluorocarbonate vein in a porphyry section, there is no mineralogical indication, that the porphyritic wall rocks and xenoliths of the breccia are impregnated by intrusion or later hydrothermal processes.

Table 18: Overview of the occurring minerals and phases in the matrix of the igneous breccia samples.

Tabelle 18: Überblick über die in der Matrix der magmatischen Brekzienproben auftretenden Minerale und Phasen

Sample	**Main phase**	**Main phase - minor phase**	**Minor phase - accessory phase**	**Accessory phase**	**Rare phase**
(Amount of clasts)	> 20 %	5 - 20 %	1-5 %	1 % - acc.	< acc.
SES1.12 55%	Fe-oxi-hydroxides	Alumosilicates	Phlogopite Apatite Pyrochlore	Monazite Baddeleyite Sulfides	
SES1.13 65%	Alumosilicates	Fe-oxi-hydroxides	Phlogopite Apatite	Monazite Pyrochlore	REE-F-Carb Magnetite
SES1.16 50%	Alumosilicates	Apatite	Fe-oxi-hydroxides Phlogopite REE-F-Carb Pyrochlore	Monazite Baddeleyite	
SES1.18 0 %*	Calcite	Fe-oxi-hydroxides REE-F-Carb	Alumosilicates Apatite	Monazite	Pyrochlore
SES1.19 65%	Alumosilicates		Fe-oxi-hydroxides REE-F-Carb Apatite	Monazite, Pyrochlore	Phlogopite Barite
SES1.20 70%	Alumosilicates	Fe-oxi-hydroxides	Phlogopite Apatite	Monazite Pyrochlore	Barite
SES1.21 40%	Alumosilicates Fe-oxi-hydroxides		Phlogopite Monazite Apatite	Pyrochlore Barite	Baddeleyite
SES1.22 25%	Alumosilicates Fe-oxi-hydroxides	Apatite	Phlogopite Monazite	Magnetite Baddeleyite	Pyrochlore Sulfides
SES1.23 30%	Alumosilicates	Fe-oxi-hydroxides Apatite	Phlogopite Monazite	Pyrochlore	Baddeleyite
SES1.24 30%	Alumosilicates	Fe-oxi-hydroxides Apatite	Phlogopite Monazite	Baddeleyite Pyrochlore Barite	
SES1.29 35%	Fe-oxi-hydroxides	Alumosilicates	Phlogopite Apatite	Monazite Baddeleyite Pyrochlore	
SES1.30 70%	Alumosilicates Fe-oxi-hydroxides	Apatite	Phlogopite Monazite	Pyrochlore	
SES1.31 65%	Alumosilicates Fe-oxi-hydroxides		Phlogopite Monazite Apatite	REE-F-Carb Pyrochlore	

Table 19: Overview of the occurring minerals and phases in the alvikite samples.

Tabelle 19: Überblick über die in den Alvikit-Proben auftretenden Minerale und Phasen

Sample	**Main phase** > 20 %	**Main phase - minor phase** 5 - 20 %	**Minor phase - accessory phase** 1-5 %	**Accessory phase** 1 % - acc.	**Rare phase** < acc.
SES1.3	Calcite Alumosilicates	Apatite Magnetite	Fe-oxi-hydroxides Phlogopite	Monazite	Pyrochlore
SES1.4	Calcite	Alumosilicates Magnetite	Phlogopite Apatite	Fe-oxi-hydroxides Monazite	REE-F-Carb Pyrochlore
SES1.5	Calcite	Alumosilicates Magnetite	Phlogopite Apatite	Fe-oxi-hydroxides Monazite	REE-F-Carb Pyrochlore
SES1.7	Calcite	Alumosilicates Phlogopite	Fe-oxi-hydroxides Apatite Magnetite	Pyrochlore	Monazite REE-F-Carb Barite
SES1.8	Calcite Alumosilicates	Phlogopite, Apatite	Fe-oxi-hydroxides Magnetite	REE-F-Carb Pyrochlore Uranophane	Monazite REE-F-Carb Sulfides
SES1.9	Calcite		Alumosilicates Phlogopite Apatite Magnetite	Fe-oxi-hydroxides Pyrochlore	Zirconolite
SES1.10	Calcite	Alumosilicates Apatite Magnetite	Phlogopite	Fe-oxi-hydroxides Pyrochlore	Monazite Sulfides Barite Uranophane
SES1.11	Calcite	Phlogopite Magnetite	Alumosilicates Apatite	Fe-oxi-hydroxides Monazite Zirconolite Pyrochlore	REE-F-Carb
SES1.17	Calcite	Alumosilicates	Phlogopite Apatite Magnetite	Monazite Zirconolite Pyrochlore	Fe-oxi-hydroxides
SES1.27	Calcite Alumosilicates		Phlogopite Apatite Magnetite	Fe-oxi-hydroxides REE-F-Carb Zirconolite Pyrochlore	Monazite
SES1.28	Calcite	Alumosilicates	Fe-oxi-hydroxides Phlogopite Apatite Magnetite	Monazite Zirconolite Pyrochlore	

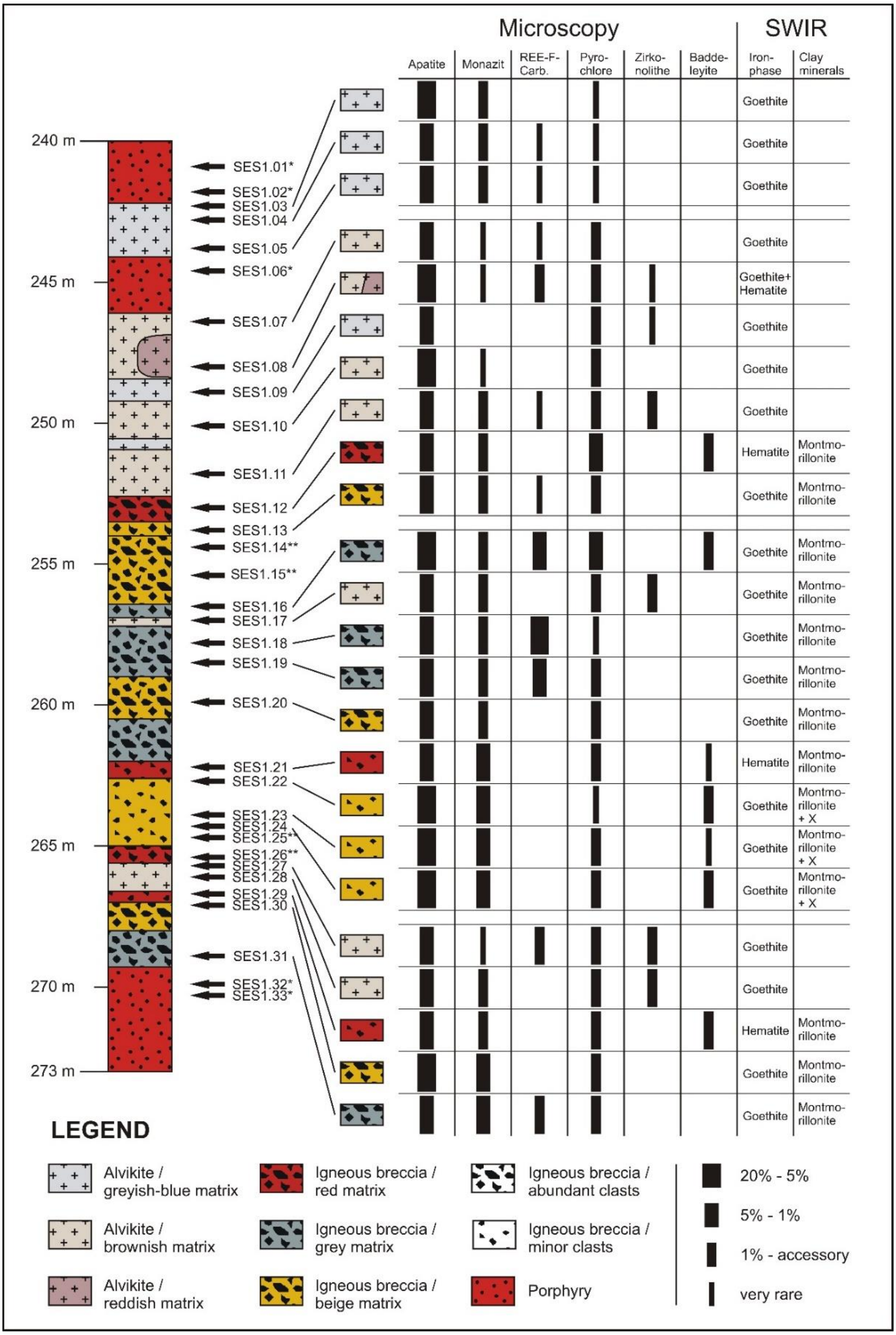

Figure 57: Overview of the distribution of phases and minerals, which characterize the mineralisation and/or possible environments. (* These samples do not belong to the mineralised part of the core; ** Of these samples, no thin section could be made).

Abbildung 57: Überblick über die Verteilung der Phasen und Minerale, welche die Mineralisation und/oder deren Entstehungsbedingungen charakterisieren (* Diese Proben gehören nicht zum mineralisierten Bereich; ** Von diesen Proben konnte kein Dünnschliff angefertigt werden.)

How is the relationship of the different lithotypes?

The macroscopic examination of the drill core SES-1/2012 revealed that three main rock types occur. The parts of the drill core, which belong to the carbonatite intrusion, consist of an igneous breccia body and some alvikite veins, which penetrate the breccia. Obviously, the alvikite veins belong to a later magmatic stage than the igneous breccias. The boundary between these two lithotypes is sharp, although the breccia reveals indications of displacement of clasts near some contacts. The different matrix colours of the igneous breccia are partially linked to the contact to the alvikite veins. A colour gradient from red to beige to grey is observed at the contact to the alvikite.

The alvikite veins as youngest lithological unit consist of a matrix, which is made of calcite and takes up more than 50 vol.%, so that the classification as a calico-carbonatite is correct. Due to the fine-grained calcite crystals and the volcanic arrangement of the veins it can be classified as alvikites.

The breccia body is also a part of a carbonatite complex, but it has generally no matrix forming calcite minerals. The matrix is nearly completely formed by alumo-siliceous matrix and iron phases, so it can be assumed, that the initial carbonatic matrix was altered and replaced by these secondary phases. Due to other minerals (apatite, baddeleyite, pyrochlore, phlogopite, REE-minerals) and the high amount of trace elements (REE, Y, Zr, Nb) (WOOLLEY & KEMPE 1989), which are typical for a carbonatite intrusion, the breccia can be classified as altered carbonatite breccia.

Whether the breccia body is an intrusive breccia or a diatreme breccia cannot be determined clearly. The breccia clasts belong mainly to the surrounding porphyritic rocks and only a few of them are made of lithological units, which could be displaced from deeper levels. An example therefore are black shale clasts, which can be assigned to the Klitschmar-Formation, which is located approximately 400 m below the examined drill core section (REICHERT et al. 2015). This mixture of clasts from different levels of depth could be a hint for a diatreme structure. On the other hand, the clasts from deeper levels are much more rounded which does not fit in the assumption of one explosive event. In the literature, diatremes are described in the UML-CR Delitzsch, for example in Serbitz as well as the occurrence or intrusive breccias (KRÜGER et al. 2013).

The porphyry of the “Schenkenberger Plagiogranitporphyr” represents the non-mineralised wall rock of the intrusion. Consequently, it is the oldest lithological unit and shows a sharp boundary to the other adjoining lithotypes. Although there is a rare occurrence of REE-fluorocarbonate veins in the porphyritic samples, which indicate a minor impregnation of the wall rock by magmatic phases or fluids, the wall rock can be regarded as completely non-mineralised. The total amount of REE and some associated elements is even lower than the average of the upper continental crust.

Which mineral forming processes are possible?

In carbonatites there are four main stages possible, in which phases can be formed and altered and elements can be mobilized, transported and deposited (ANDERSEN et al. 2017). The first stage of course is the magmatic stage, in which many minerals, especially the phenocrysts crystallize. Carbonatite magma has many volatile components (for example H_2O, Cl, F, S), which are residual enriched in the magma, so that a fluid phase is formed, which contains many incompatible elements. From this genetic relationship arise two possibilities, how the minerals, which incorporate these incompatible elements, will be formed. They can crystallize directly out from the magma, or out from the fluid phase. In this case, the elements can be resorbed from the magma or remobilised from earlier phases (VERPLANCK 2017). This second stage is directly linked to the magmatic intrusion and called carbothermal (ANDERSEN et al. 2017). The third stage is the “normal” epithermal stage and at least supergene processes represents the last stage, which can change the mineralogical composition (VERPLANCK 2017).

The minerals, which are detected in the mineralised sections can only be partially assigned to a certain stage. The large phenocrysts (apatite, phlogopite, magnetite, pyrochlore in breccias, baddeleyite), which clearly belong to the magmatic stage, are already crystallized in a greater depth. For the majority of the fine- to medium-grained crystals (apatite, zirconolite, phlogopite, pyrochlore in alvikites) associated with the ground-mass it is not absolutely clear, whether they are formed primary magmatic, primary carbothermal, secondary carbothermal, or hydrothermal. The calcite matrix in the alvikites is most likely overprinted carbothermal, because a fine-grained magmatic-texture could not be observed. Calcite veins and areas containing larger crystals are, insofar they do not belong to a xenolith, formed later and therefore belong to the hydrothermal or supergene stage, as shown in terms of the calcitic matrix of the thin section SES1.18.

The majority of the monazites and all REE-fluorocarbonates can be interpreted as secondary carbothermal, hydrothermal or supergene because of their texture and association to altered areas and secondary phases. The Alumosilicates and iron phases are secondary as well and most likely formed by a hydrothermal or supergene process.

Which further statements can be deduced from the mineralogy of the mineralised sections?

Apatite occurs in extrusive rocks as euhedral prismatic phenocrysts and as smaller groundmass crystals. The phenocrysts often react with hydrothermal fluids, what can cause the formation of monazite, REE-fluorocarbonates and secondary apatites. Hydrothermal apatites often have lower amounts of REE, strontium, manganese and thorium but higher amounts of fluorine (CHAKHMOURADIAN et al. 2017). The REE enriched rim, which was detected in several thin sections, is an often-occurring zoning in carbonatite-hosted apatites. This zoning can grow as a consequence of a couple of processes. In general, the early crystallisation of apatite causes a depletion of REE in the remaining magma, so that the rims must be formed in a later process. Possible is, that the crystallisation of other phases like baddeleyite, magnetite and phlogopite causes a residual enrichment of REE in the magma (or in a further generated fluid phase) or that a new magma with a changing composition brings new REE to the melt. Epithermal overprints can also build rims at apatites, but these would be enriched with other elements than REE. REE from those fluids are mainly deposited in secondary monazite or REE-fluorocarbonates (CHAKHMOURADIAN et al. 2017). It can conclude, that REE-enriched rims were formed in a magmatic or carbothermal environment.

The oscillatory zonation of **pyrochlores** in the alvikite sections is often related to a magmatic or carbothermal event. Altered pyrochlores have a higher proportion of vacancies in their A-position. These occur especially in supergene weathered, but also in hydrothermal altered pyrochlores (Mitchell 2015). In the analysed pyrochlores, the amount of possibly A-position cations (mainly Ca, Na) is in the breccia 3 mol.% higher than in the alvikites, but the difference is too low to derive a different grade of alteration. The Bear Lodge carbonatites (USA) contain secondary betafite, in which the calcium and uranium is incorporated (A-position in the pyrochlore formula) (ANDERSEN et al. 2017). In Mt. Weld (Australia), the pyrochlores are supergene leached and partially replaced by crandallite (LOTTERMOSER & ENGLAND 1988). Crandalite was not found in this study, but betafite from Bear Lodge could be a hint, that the detected secondary titanium oxides represent betafite with a high proportion of vacancy.

The **phlogopites** show microscopically some of the most evident indications of alteration. The presence of secondary goethite can be regarded as a product of weathering. This alteration begins with the loss of the interlayered ions and a partially iron oxidation. During this, goethite is formed and the phlogopite begins to transform to vermiculite. Advanced alteration would cause a release of cations from the octahedral layers and the transformation to kaolinite (GILKES 1979). This second alteration step was not observed in the samples. Barium- or iron-enriched rims are common in carbonatite hosted phlogopites. These rims result from kinoshitalite substitution (REGUIR et al. 2009). Phlogopite and kinoshitalite are endmembers of a solid solution. For the substitution potassium and silicon interchange with barium and tetrahedral alumina (FLEEt et al. 2003).

The difference of the zirconium-bearing minerals (**baddeleyite** in the breccias and **zirconolite** in the alvikites) cannot be explained by hydrothermal processes and must be caused by different magmatic environments in the different magmatic stages. Zirconolite is quiet common in carbonatites and can be formed from baddeleyite (GIERE et al. 1998). But this reaction, which takes place in fluid phases cause a zirconolite rim around the baddeleyite crystals and does not lead to new formed euhedral zirconolite crystals (LUMPKIN 1999). Therefore, the hydrothermal transformation can be ruled out. The baddeleyites in the igneous breccia have no zirconolite rim and the zirconolites in the alvikites have no baddeleyite core.

Monazite in carbonatite is often a secondary phase, which is associated with apatite and completely can replace it. In the Purulia phoscorite (India), corona textures of monazite around apatites are described (CHEN et al. 2017). The apatite-monazite association is also described for the Bayan Obo mine (China). Additionally, the monazites of the Bayan Obo mine occur disseminated and accumulated in clusters (DENG et al. 2017). Another locality, where monazite is accumulated as corona around quartz was not found in the literature.

Hydrothermal and igneous monazites crystals are difficult to distinguish. In average, the hydrothermal monazites are smaller crystals with a lower amount of thorium (< 1 wt.%), while in igneous monazites, the concentration of thorium is higher (3-5 wt.%) (SCHANDL & GORTON 2004). In the measured monazites, the thorium concentration is in most cases lower than 1 wt.%. Only in some monazites, the amount is similar to igneous monazites, but these crystals belong to an accumulation as phenoclast, so they can be interpreted as secondary too. The differences between hydrothermal and supergene monazite is not jet described in the literature. It can be estimated, that the monazites, which are finely disseminated in the alumo-siliceous matrix of the breccias, were formed concurrent. With an average size of less than one micrometre, the monazites are smaller than the most crystals, which are described in the literature. Additionally, it was not possible to distinguish between monazite and rabdophane, what could give a hint on formation conditions. Summarizing, the different monazite textures display mostly secondary phases, but they are not understood yet very well.

Montmorillonite belongs to the dioctahedral smectites and is endmember of the montmorillonite-beidellite series. It is typically a product of the weathering of mafic to intermediate volcanic rocks and therefore not a climate indicator like for example kaolinite. For the emergence of montmorillonite, sufficient amounts of dissolved divalent iron and magnesium are necessary. Consequently, montmorillonite can be easier formed in weak reducing than in oxidising environment (Heim 1990). These conditions fit in the interpretation, that the matrix of the igneous breccias was originally carbonatic. The dissolution of carbonates such as dolomite or ankerite would release the necessary amount of iron and magnesium ions.

Which transportation and alteration environments can be assumed for the REE?

The REE mainly occur as complexes in liquid phases, so that the mobility of REE cannot be derived only by the chemical environment (pH, Eh). Especially chloride and sulphide are REE-mobilizing ligands, whereas fluoride causes deposition. The presence of fluoride in combination with neutralized acidity causes the immobilization of REE. In addition, the occurrence of phosphate and carbonate causes the precipitation of monazite and REE-fluorocarbonates. If barium is available and the transport of the rare earth elements is linked to sulphides, then the deposition of barite is possible. This is only one example for transport and deposition of REE. In general, there is very little knowledge about the behaviour of REE in carbonate-bearing solution of the high temperature stability of many complexes like REE-hydroxyl complexes (Migdisov et al. 2016). The fractionation of the REE can give hints to the environment, in which they were deposited. The majority of the REE only exist in a trivalent stage, and so the chemical behaviour is similar (Sicius 2016). Europium, which can occur divalent and trivalent, causes a negative europium anomaly in many lithotypes. This is caused by extremely reducing conditions in hot fluids, which effect, that the divalent europium stays mobile, while all other REE precipitate (Brookins 1988). The lack of a europium anomaly in the alvikites and breccias can be therefore interpreted that such a fluid phase was absent. Cerium can exist trivalent as well as tetravalent. The tetravalent cerium is very insoluble and forms the mineral cerianite (**CeO_2**). Therefore, a negative cerium anomaly can exist, if a REE-containing solution has an oxidising environment, which causes the oxidation and precipitation of cerium. For example sea water has a clear negative cerium anomaly (Brookins 1988).

The geochemical data show no cerium anomaly, so that oxidising fluids, which were able to oxidise cerium, can be ruled out. The REE-distribution of the breccia-hosted monazites and REE-fluorocarbonates also showed no indication of a cerium anomaly. In the alvikite sections, small differences in distribution of the REE were detected, which can be caused by an oxidation of cerium. Especially the REE-fluorocarbonates in thin section SES1.27 are extremely cerium-rich.

Furthermore, under supergene conditions, the LREE can be deposited easier, than the HREE, so that the ration between LREE to HREE increases. In Mt. Weld, the REE were mobilised by acidic solutions in the aerated zone and the LREE were precipitated as monazite and rabdophane in the groundwater zone due to higher pH values. This causes an enrichment of the LREE in the groundwater zone and in a bigger scale a residual enrichment of REEs, because many other elements are dissolved and transported much further (Lottermoser 1990). Niobium is in most environments relative insoluble and therefore also residual enriched in supergene altered carbonatite systems (Mitchell 2015). The comparison of the geochemical data with the dataset from deeper sections of the drill core shows that the ratio of LREE to HREE is slightly bigger in the deeper sections.

This can be interpreted, that a supergene alteration, which causes a mobilisation and transport of REE did not take place on a large scale. Furthermore, no cerianite was detected. However, this means that a supergene transport and cerium oxidation is ruled out, while an in-situ replacement of REE-minerals by supergene overprint cannot be excluded. It can be an indication, that REE minerals are formed carbothermal or hydrothermal, but it was not possible, to determine chemical parameters of the fluid phase. A comparison with other carbonatites shows, that a variety of possible environments can be considered, in which the REE phases can be formed (Tab. 20).

Table 20: Examples for hydrothermal environments, in which other REE-minerals were formed (after MIGDISOV et al. 2016).

Tabelle 20: Beispiele für hydrothermale Bedingungen, in denen sich andere SEE-Minerale gebildet haben (nach MIGDISOV et al. 2016)

Name, locality	Major REE-minerals	Associated fluid chemistry
Bayan Obo, China	Monazite-(Ce) Bastnaesite-(Ce)	Early monazite-(Ce) stage: >280–330 °C at P>0.7 kbar, 1-5 wt.% NaCl; Main stage bastnaesite-(Ce): >400 °C to 300 °C at P >0.9 to 1.4 kbar, 6–10 wt.% NaCl
The Gallinas Mountains, New Mexico	Bastnaesite-(Ce)	≈400 °C, sulfate-rich NaCl-KCl brines having a salinity of ≈15 wt.% NaCl equivalent
Karonge, Burundi	Bastnaesite-(Ce) Monazite-(Ce)	Preliminary homogenization data suggest that they formed at >420 °C
Capitan Pluton, New Mexico	Allanite-(Ce) REE -rich titanite	Homogenization temperatures 260 to 480 °C; 80 wt.% total salt, including up to 44 wt.% Cl, 5245 ppm F, 24210 ppm SO_4
Olympic Dam, South Australia.	Bastnaesite-(Ce) Florencite-(Ce) Monazite-(Ce) Xenotime-(Y) Britholite-(Ce)	Magnetite stage: >400 °C, medium-hyper saline (20-45 wt.% NaCl), Hematite stage: 150–300 °C, 1-8 wt.% NaCl

How can the different colours of the matrix in the igneous breccias be interpreted?

The matrix colours are obviously caused by the oxidation state and the amount of iron. The red coloured matrix sections have increased amounts of iron, which is predominantly deposited as hematite, whereas in the other sections goethite is predominating. Additionally, the breccia sections with grey matrix are the only occurrences of breccia hosted REE-fluorocarbonates and the thin section SES1.18, which also has a grey matrix, is the only breccia sample, where calcite was detected under the microscope.

The interpretation of the special thin section SES1.18 is, that individual secondary calcite veins occur in the grey matrix, in which extremely large REE-fluorocarbonates have grown. These veins could be the cause for the weak reaction with hydrochloric acid when tested.

In general, the colour of the matrix can be interpreted in two ways. One possibility is, that the whole breccia was oxidized due to alteration and only the grey and beige areas have been subsequently reduced. However, it is more likely, that the breccia initially was goethite-dominated and then red areas were subsequently oxidized to hematite, because the red portions of the rock are generally spatially linked to the intrusive contacts with the alvikites. The oxidation could have been caused by the intrusion of the alvikite veins, or by later descending oxidizing (meteoric) fluids, which used the contact zones as fluid pathways. However, the latter explanation is less likely, since in this case, a similar zonation should also be associated with the alvikite veins.

How useful is the measurement of the magnetic susceptibility?

The measurement of the magnetic susceptibility was carried out in order to test the suitability and applicability of this method for petrological characterization and differentiation of various rock types and possibly alteration zone. The results show clearly the differences of the single rock types and together with the information from microscopy the mineral phases, which are responsible for the susceptibility, have been determined as well. However, it was not possible, to define single phases without the results from the microscopy. Therefore, it is advisable to use the measurements of the susceptibility only in combination with microscopic studies.

In the case of the examined drill core section, the different rock types could be distinguished easily macroscopically, but if this is not possible, then the susceptibility is a good and non-destructive method, to measure in a short time a high amount of samples to get some first information about the magnetic variability of the rock. In the best case, different zones of rock types and/or alteration can be identified and distinguished, so that the most interesting areas for sampling and further investigations are quickly identified.

8. Conclusions

The upper part of the Storkwitz-Carbonatite has been characterised geochemically and mineralogically based on a detailed multi-method investigation of recently provided drill core samples. The following results are concluded from these investigations:

- The alvikite veins and igneous breccias contain a REE-mineralisation with an average concentration of 0.2 - 1.2 wt.% REE_2O_3. The majority of the enriched REE are LREE, especially the elements lanthanum, cerium, and neodymium.

- The REE-bearing minerals have formed predominantly by secondary processes. Due to the detection limit of the SEM-EDX analyses, it was not possible, to determine analytically and statistically reliable concentrations of the REE in the primary magmatic minerals.

- The breccia matrix is completely altered and original minerals were replaced by cryptocrystalline secondary phases, which could originate either from hydrothermal or from supergene processes. However, the elevated temperatures at which hydrothermal processes typically take place would form better defined mineral phases and crystals and are less likely to result in the formation of cryptocrystalline minerals and textures, which indicate very immature mineral formation at low temperatures. It is thus more likely that the cryptocrystalline mineral phases have formed by supergene, low-temperature processes, related to oxidising fluids that descended relatively deeply below the former land surface.

- Another indication for supergene processes is the existence of abundant goethite as interlayers to phlogopite and the marked cryptocrystallinity of the entire matrix of the breccia body. One can assume that the finely disseminated monazite in the breccia also formed during the same supergene process together with the recrystallization of the matrix.
- No enrichment of the REE content of the upper part of the mineralisation, compared to the deeper parts of the intrusion can be detected with the geochemical data. The supergene processes have thus not led to a significant enrichment of REE in the upper part of the mineralisation. It appears more likely that the supergene REE-minerals formed in-situ by replacing magmatic precursor REE-bearing minerals.

- Locally, the REE concentrations differ substantially in REE-fluorocarbonates, but far less in monazites. This REE-fractionation can be observed predominantly in the alvikite veins, which might be caused by spatially restricted, microscale cerium oxidation. Such a cerium oxidation in alvikites requires an oxidizing environment, which would point further to a supergene origin of this phenomenon.

The REE-mineralization associated with breccias and alvikite as observed in the studied drill core contains predominantly secondary mineral phases such as monazite as well as bastnaesite-synchisite group minerals. Microscopic observations reveal that the matrix of breccia is completely altered. Supergene alteration is strongly suggested by the mineral paragenesis and textural evidence, although the supergene processes have apparently not led to a significant enrichment of the REE in the near-surface portion of the Storkwitz carbonatite.

Annex

Table 21: Petrographic log of the drill core SES-1/2012 from 240 to 273 m.

Tabelle 21: Petrografischer Log der Bohrkerns SES-1/2012 von 240 bis 272 m

Depth from [m]	Depth to [m]	Conservation [m]	Lithotype	Rock characteristics
240	241.1	Massive core	Porphyry	Porphyric texture, fine- to medium-grained, Qz and Feldspar phenocrysts (approx. 1 mm), yellowish to ochre colour, no reaction with HCl, occasionally joints with brownish filling.
241.1	242.2	Massive core, 241.8 - 242 big fragments	Porphyry	Porphyric texture, fine- to medium-grained, Qz and Feldspar phenocrysts (approx. 1 mm), increasingly light reddish colour, smooth transition to roof rock, no reaction with HCl, increasingly occurring joints with hematite.
242.2	244.1	Massive core	Alvikite	Greyish Matrix with white calcitic speckles, streaks and veins, partially zonation recognizable, greyish matrix homogeneous in itself, Magnetite phenocrysts, Phlogopite phenocrysts partially accumulated in layers, strong reaction with HCl
244.1	246.1	244.1-244.6 massive core, 244.6-245 and 245.5-246.1 big fragments, 245-245.5 small fragments,	Porphyry	Porphyric texture, fine- to medium-grained, Qz and Feldspar phenocrysts (approx. 5 mm), reddish colour with beige sections, leached near joints, abundant big joints, partially with hematite, no reaction with HCl, penetrating alvikite vein from the roof rock
246.1	247.6	Small fragments; 246,6-246,8 and 247,3-247,5 big fragments	Alvikite	Greyish brown rock, soft, clayish matrix, some xenoliths, magnetite phenocrysts, strong reaction with HCl, colour transition to reddish brown in lower section
247.6	248.2- 249	Massive core, broken several times	Alvikite	Massive rock, clayish matrix, ochre to reddish colour with sharp oxidation horizon, increasing amount of magnetites, strong reaction with HCl
248.2-249	249-249.2	Massive core, broken several times	Alvikite	Fine grained matrix, greyish blue to blue colour, homogeneous appearance, calcite veins, strong reaction with HCl
249-249.2	250.6	Massive core	Alvikite	Greyish to greyish-brown rocks, partially clayish matrix, magnetite phenocrysts, strong reaction with HCl
250.6	250.8	Massive core	Alvikite	Fine grained matrix, greyish blue to blue colour, homogeneous appearance, calcite veins, strong reaction with HCl
250.8	252.5	Massive core, 251.6-252 big fragments	Alvikite	Greyish to greyish-brown rocks, partially clayish matrix, magnetite phenocrysts, strong reaction with HCl
252.5	253.5	Well conserved core, big fragments	Igneous breccia	Breccia with abundant clasts, mainly sub-angular porphyritic clasts, brick-red matrix, nearly no reaction with HCl
253.5	254	Fragments, breccia texture recognizable	Igneous breccia	Breccia with abundant clasts, mainly sub-angular porphyritic clasts, beige matrix, nearly no reaction with HCl
254	254.3	Fragments, breccia texture recognizable	Igneous breccia	Breccia with abundant clasts, mainly sub-angular porphyritic clasts, greyish matrix, very weak reaction with HCl
254.3	256.5	Loose, breccia texture not recognizable	Igneous breccia	Breccia with abundant clasts, beige to ochre matrix, nearly no reaction with HCl

Continued from table 21 – Fortsetung von Tabelle 21

Depth from [m]	Depth to [m]	Conservation [m]	Lithotype	Rock characteristics
256.5	256.9	Loose, breccia texture not recognizable	Igneous breccia	Breccia with abundant clasts, greyish brown matrix, weak reaction with HCl
256.9	257.2	Fragmented core	Alvikite	Approx. 10 cm wide alvikite vein, dark grey matrix, magnetite phenocrysts, strong reaction with HCl
257.2	259	Fragments 257.2-257.8, below massive core	Igneous breccia	Breccia with abundant clasts, mainly sub-angular porphyritic clasts, grey matrix, weak reaction with HCl
259	260.5	Largely massive core	Igneous breccia	Breccia with abundant clasts, mainly sub-angular porphyritic clasts, beige to ochre matrix, nearly no reaction with HCl
260.5	262	Loose, breccia texture not recognizable	Igneous breccia	Breccia with abundant clasts, greyish brown matrix, nearly no reaction with HCl
262	262.6	Loose, breccia texture not recognizable	Igneous breccia	Breccia with minor smaller clasts, (max. a few centimetres big), matrix clayish, brick-red and disintegrated, very weak reaction with HCl
262.6	264	Largely massive core	Igneous breccia	Breccia with minor clasts, mainly sub-angular porphyritic clasts, beige to ochre matrix, nearly no reaction with HCl
264	265	Largely massive core	Igneous breccia	Breccia with minor clasts, mainly sub-angular porphyritic clasts, beige to ochre heterogeneous matrix, rare calcite streaks, nearly no reaction with HCl
265	265.6	Largely massive core	Igneous breccia	Breccia with abundant clasts, mainly sub-angular porphyritic clasts, red matrix, no reaction with HCl
265.6	265.9	Massive core	Alvikite	Greyish to black fine-grained matrix, calcite streaks, heterogeneous appearance, strong reaction with HCl
265.9	266.6	Massive core	Alvikite	Greyish to brown medium-grained clayish matrix, homogeneous appearance, rare reddish streaks, strong reaction with HCl
266.6	266.9	Massive core	Igneous breccia	Breccia with minor smaller clasts, (max. a few centimetres big), matrix clayish and brick-red nearly no reaction with HCl
266.9	267.95	Massive core	Igneous breccia	Breccia with abundant clasts, mainly sub-angular porphyritic clasts, beige to ochre matrix, nearly no reaction with HCl
267.95	268.3	One big Clast	Igneous breccia	Greyish brown to reddish massive porphyritic xenolith
268.3	269.3	Massive core	Igneous breccia	Breccia with abundant clasts, mainly sub-angular porphyritic clasts, grey matrix, weak reaction with HCl
269.3	273	Massive core	Porphyry	Porphyric texture, fine- to medium-grained, Qz and Feldspar phenocrysts (approx. 1 mm), yellowish-ochre to light red colour, leached at joints, no reaction with HCl, occasionally joints with talc filling and slickensides, penetrated by porphyritic, maybe andesitic veins (270.8-273 m).

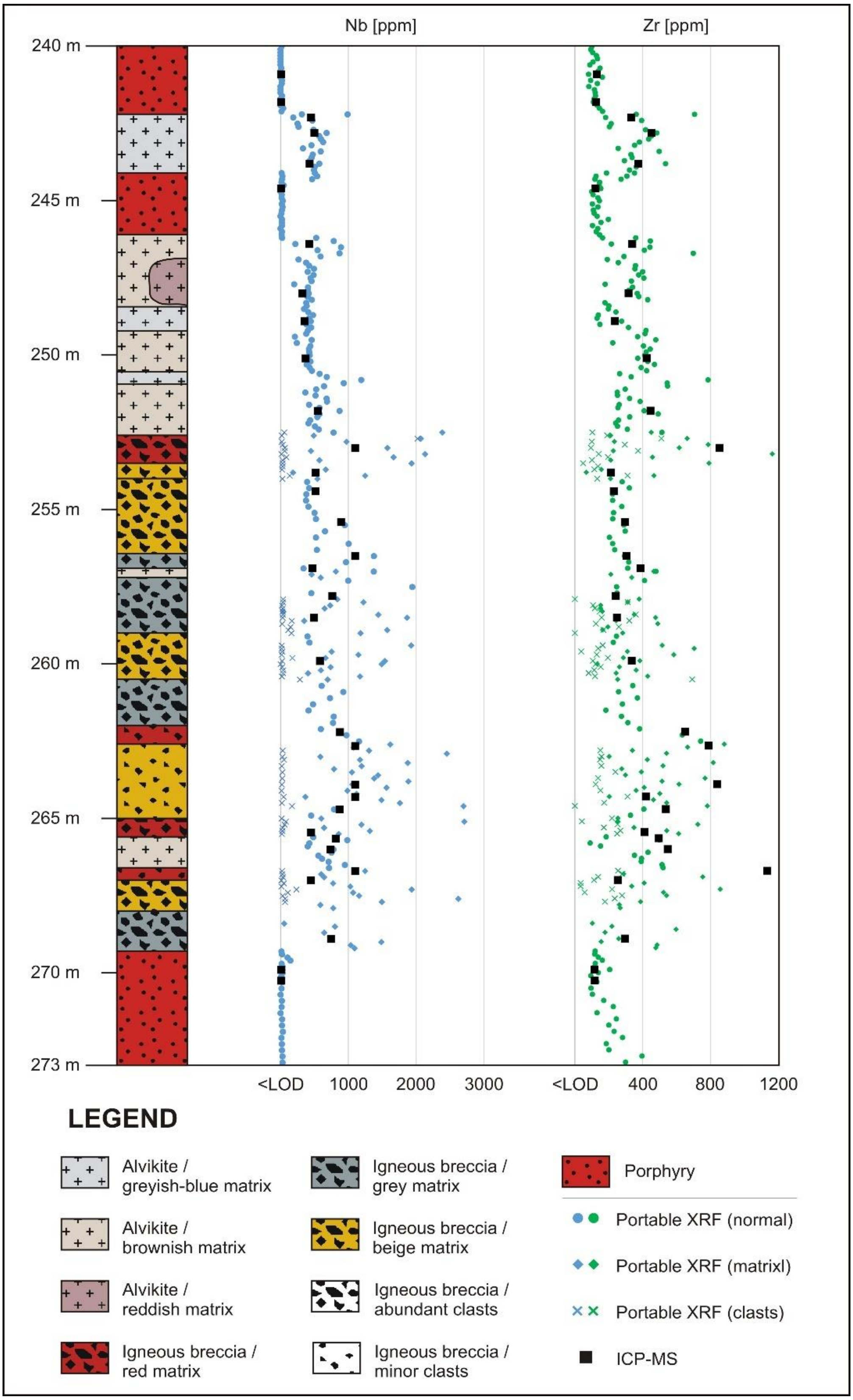

Figure 58: Portable XRF reading of the Nb and Zr concentrations in comparison with ICP-MS whole rock analysis. Portable XRF data are presented separate for matrix and clasts in the breccia sections.

Abbildung 58: Ergebnisse der portablen RFA-Messungen für Nb und Zr im Vergleich mit der ICP-MS Gesamtgesteinsanalyse. In den Brekzien-Bereichen sind die portablen RFA Werte in Klasten und Matrix unterteilt.

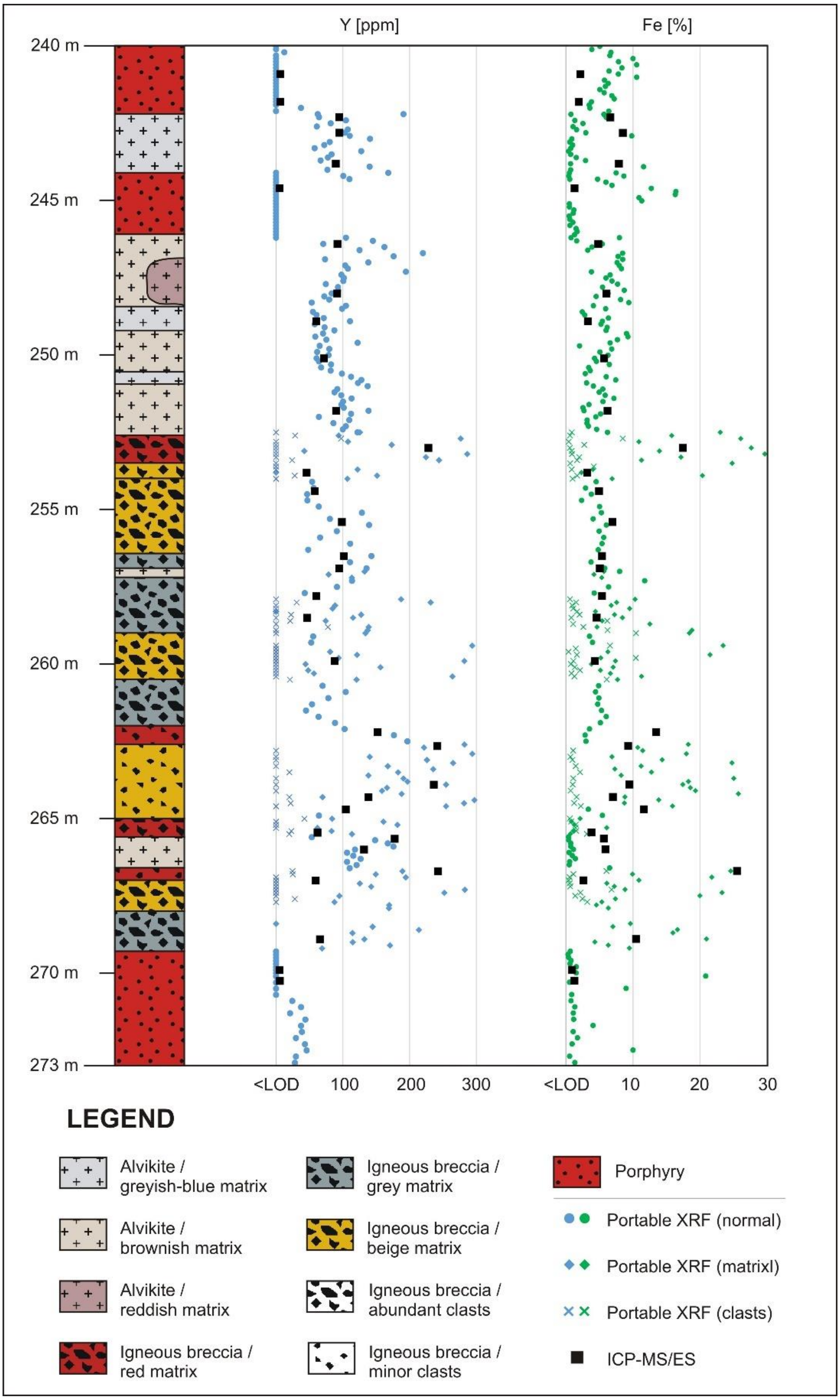

Figure 59: Portable XRF reading of the Y and Fe concentrations in comparison with ICP-MS/ES whole rock analysis. Portable XRF data are presented separate for matrix and clasts in the breccia sections.

Abbildung 59: Ergebnisse der portablen RFA-Messungen für Y und Fe im Vergleich mit der ICP-MS/ES Gesamtgesteinsanalyse. In den Brekzien-Bereichen sind die portablen RFA Werte in Klasten und Matrix unterteilt.

Table 22: Table with the geochemical data from the whole rock analysis for all taken samples; colour codes by their lithology.

Tabelle 22: Tabelle mit den geochemischen Daten der Gesamtgesteinsanalyse für alle genommen Proben; Farbkodiert je nach Lithotyp

Major oxides / elements (ICP-ES) [1/2]		Analyte	Weight	SiO_2	Al_2O_3	Fe_2O_3	MgO	CaO	Na_2O	K_2O
		Method	WGHT	LF200	LF200	LF200	LF200	LF200	LF200	LF200
		Unit	kg	%	%	%	%	%	%	%
		MDL	0.01	0.01	0.01	0.04	0.01	0.01	0.01	0.01
Sample	**Depth [m]**	**Lithotype**								
SES1.01	**240.90**	**Porphyry**	0.14	69.12	15.95	3.11	0.49	0.26	4.11	3.71
SES1.02	**241.80**	**Porphyry**	0.23	70.34	15.59	2.79	0.36	0.26	5.13	3.33
SES1.03	**242.30**	**Alvikite**	0.18	9.13	3.02	9.50	6.78	36.53	0.28	0.48
SES1.04	**242.80**	**Alvikite**	0.19	10.14	3.70	12.17	7.90	32.76	0.31	0.64
SES1.05	**243.80**	**Alvikite**	0.22	9.98	3.59	11.31	7.54	33.71	0.26	0.45
SES1.06	**244.60**	**Porphyry**	0.25	71.72	15.65	1.86	0.66	0.40	3.39	3.00
SES1.07	**246.40**	**Alvikite**	0.12	7.02	2.39	6.93	5.60	41.18	0.19	0.44
SES1.08	**248.00**	**Alvikite**	0.16	11.32	4.05	8.67	4.73	35.61	0.34	0.87
SES1.09	**248.90**	**Alvikite**	0.25	3.13	1.19	4.69	1.71	48.63	0.17	0.31
SES1.10	**250.10**	**Alvikite**	0.32	13.57	4.53	8.18	3.28	33.24	0.47	0.58
SES1.11	**251.80**	**Alvikite**	0.24	6.27	1.86	8.90	2.08	43.20	0.25	0.44
SES1.12	**253.00**	**Igneous breccia**	0.10	38.03	9.43	24.95	1.89	8.19	1.57	2.81
SES1.13	**253.80**	**Igneous breccia**	0.13	65.45	14.35	4.57	1.13	1.33	1.88	4.92
SES1.14	**254.40**	**Igneous breccia**	0.16	63.67	13.40	7.09	1.18	1.45	2.13	4.86
SES1.15	**255.40**	**Igneous breccia**	0.20	57.34	13.60	9.93	1.44	2.37	2.25	4.13
SES1.16	**256.50**	**Igneous breccia**	0.13	56.94	14.17	7.73	1.38	3.20	1.98	4.17
SES1.17	**256.90**	**Alvikite**	0.18	5.86	2.17	7.24	2.17	44.19	0.27	0.35
SES1.18	**257.80**	**Igneous breccia**	0.21	54.37	13.07	7.72	1.18	6.25	2.28	3.78
SES1.19	**258.50**	**Igneous breccia**	0.23	62.71	13.78	6.59	1.29	1.85	2.86	3.29
SES1.20	**259.90**	**Igneous breccia**	0.39	60.72	14.26	6.18	1.18	2.92	2.12	4.38
SES1.21	**262.20**	**Igneous breccia**	0.26	45.47	11.01	19.27	1.78	5.42	1.27	3.33
SES1.22	**262.65**	**Igneous breccia**	0.24	42.73	10.92	13.31	2.91	8.76	1.21	3.56
SES1.23	**263.90**	**Igneous breccia**	0.22	44.71	10.90	13.59	2.59	7.64	1.19	3.30
SES1.24	**264.30**	**Igneous breccia**	0.27	55.35	13.70	10.05	1.56	3.00	1.42	3.76
SES1.25	**264.70**	**Igneous breccia**	0.16	50.74	12.44	16.64	1.71	2.72	1.31	3.82
SES1.26	**265.45**	**Igneous breccia**	0.18	64.81	14.26	5.47	1.00	1.44	1.60	4.93
SES1.27	**265.65**	**Alvikite**	0.13	4.57	1.89	8.12	2.04	43.74	0.31	0.31
SES1.28	**266.00**	**Alvikite**	0.18	6.06	2.36	8.46	2.30	42.55	0.35	0.34
SES1.29	**266.70**	**Igneous breccia**	0.28	31.60	8.70	36.51	1.90	5.65	1.07	3.48
SES1.30	**267.00**	**Igneous breccia**	0.30	66.31	14.50	3.76	1.07	1.19	1.98	4.36
SES1.31	**268.90**	**Igneous breccia**	0.25	52.00	12.51	14.98	1.64	1.77	3.25	6.19
SES1.32	**269.90**	**Porphyry**	0.21	71.79	16.03	1.34	0.49	0.30	4.38	3.06
SES1.33	**270.25**	**Porphyry**	0.16	70.96	16.06	1.85	0.51	0.29	4.45	2.98

Continued from Table 22 – Fortsetung von Tabelle 22

Major oxides / elements (ICP-ES)		Analyte	TiO_2	P_2O_5	MnO	Cr_2O_3	Ba	Sc	LOI	Sum
		Method	LF200	LF200	LF200	LF200	LF200	LF200	LF200	LF200
		Unit	%	%	%	%	ppm	ppm	%	%
[2/2]		MDL	0.01	0.01	0.01	0.002	1	1	-5.1	0.01
Sample	Depth [m]	Lithotype								
SES1.01	240.90	Porphyry	0.20	0.07	0.02	<0.002	1822	3	2.7	99.93
SES1.02	241.80	Porphyry	0.20	0.07	<0.01	<0.002	895	2	1.8	99.94
SES1.03	242.30	Alvikite	1.83	2.62	0.79	0.031	794	18	27.9	98.99
SES1.04	242.80	Alvikite	2.44	2.75	0.89	0.045	874	22	25.1	98.95
SES1.05	243.80	Alvikite	2.39	2.59	0.76	0.024	544	20	26.4	99.04
SES1.06	244.60	Porphyry	0.21	0.08	<0.01	<0.002	1408	3	2.8	99.92
SES1.07	246.40	Alvikite	1.52	3.73	0.56	0.014	3333	15	29.1	99.03
SES1.08	248.00	Alvikite	2.52	2.50	0.81	0.025	5673	18	27.1	99.15
SES1.09	248.90	Alvikite	0.51	2.40	0.45	0.017	3234	11	35.6	99.13
SES1.10	250.10	Alvikite	2.54	2.73	3.22	0.038	3014	18	26.5	99.22
SES1.11	251.80	Alvikite	1.15	3.30	1.12	0.035	1264	17	30.5	99.30
SES1.12	253.00	Igneous breccia	0.59	5.92	0.13	0.008	1903	27	4.6	98.31
SES1.13	253.80	Igneous breccia	0.28	0.88	0.04	0.003	1440	8	4.6	99.54
SES1.14	254.40	Igneous breccia	0.30	1.00	0.06	0.003	641	11	4.2	99.41
SES1.15	255.40	Igneous breccia	0.36	1.79	0.08	0.007	1036	13	5.4	98.83
SES1.16	256.50	Igneous breccia	0.50	2.18	0.05	0.006	1629	16	6.4	98.88
SES1.17	256.90	Alvikite	1.07	3.28	0.74	0.033	496	14	31.8	99.24
SES1.18	257.80	Igneous breccia	0.41	1.34	0.37	0.004	876	16	8.4	99.24
SES1.19	258.50	Igneous breccia	0.37	1.05	0.10	0.004	838	11	5.5	99.45
SES1.20	259.90	Igneous breccia	0.40	2.07	0.07	0.004	824	9	4.8	99.24
SES1.21	262.20	Igneous breccia	0.45	4.16	0.14	0.007	2202	20	6.1	98.69
SES1.22	262.65	Igneous breccia	0.55	6.65	0.14	0.010	2499	22	7.1	98.08
SES1.23	263.90	Igneous breccia	0.49	5.08	0.44	0.007	4654	22	7.7	98.18
SES1.24	264.30	Igneous breccia	0.43	2.20	0.10	0.007	1785	15	7.0	98.72
SES1.25	264.70	Igneous breccia	0.42	2.01	0.12	0.006	2506	15	6.7	98.95
SES1.26	265.45	Igneous breccia	0.50	0.82	0.05	0.004	1253	10	4.4	99.46
SES1.27	265.65	Alvikite	1.18	3.80	1.13	0.032	502	12	31.8	98.94
SES1.28	266.00	Alvikite	1.20	3.89	0.53	0.040	1085	17	30.8	99.00
SES1.29	266.70	Igneous breccia	0.55	4.42	0.12	0.012	2445	21	3.9	98.15
SES1.30	267.00	Igneous breccia	0.33	0.82	0.02	0.003	1232	6	5.0	99.44
SES1.31	268.90	Igneous breccia	0.48	1.20	0.17	0.006	803	15	4.7	98.96
SES1.32	269.90	Porphyry	0.21	0.08	<0.01	<0.002	855	2	2.1	99.92
SES1.33	270.25	Porphyry	0.20	0.08	0.02	<0.002	823	3	2.4	99.93

Continued from Table 22 – Fortsetung von Tabelle 22

Rare earth elements (ICP-MS) [1/2]		Analyte	La	Ce	Pr	Nd	Sm	Eu	Gd	Tb
		Method	LF200	LF200	LF200	LF200	LF200	LF200	LF200	LF200
		Unit	ppm	ppm	ppm	ppm	ppm	ppm	ppm	ppm
		MDL	0.1	0.1	0.02	0.3	0.05	0.02	0.05	0.01
Sample	Depth [m]	Lithotype								
SES1.01	240.90	Porphyry	21.2	42.4	4.27	15.9	2.37	0.59	1.84	0.22
SES1.02	241.80	Porphyry	32.0	60.6	6.49	23.0	3.39	0.79	2.22	0.26
SES1.03	242.30	Alvikite	1371.8	2042.6	198.27	607.8	67.11	16.78	42.12	4.74
SES1.04	242.80	Alvikite	1232.0	1962.1	201.93	625.8	71.04	17.73	43.63	5.03
SES1.05	243.80	Alvikite	1175.7	1840.1	181.36	560.6	63.35	15.97	40.85	4.38
SES1.06	244.60	Porphyry	29.7	44.3	5.35	18.3	2.76	0.49	1.87	0.22
SES1.07	246.40	Alvikite	1147.2	1879.2	193.88	605.5	70.00	17.73	43.37	4.82
SES1.08	248.00	Alvikite	882.8	1199.6	119.91	377.0	46.24	12.41	31.37	3.73
SES1.09	248.90	Alvikite	472.2	689.7	76.34	258.1	35.11	9.52	24.52	2.92
SES1.10	250.10	Alvikite	699.4	1085.4	113.66	373.7	45.78	12.14	31.83	3.58
SES1.11	251.80	Alvikite	672.6	1021.9	118.15	403.3	53.28	14.34	36.52	4.34
SES1.12	253.00	Igneous breccia	1767.6	3361.1	379.48	1296.8	165.29	41.53	103.07	12.03
SES1.13	253.80	Igneous breccia	573.1	951.8	101.53	322.5	34.60	7.88	19.46	2.18
SES1.14	254.40	Igneous breccia	855.8	1379.9	149.40	462.4	48.19	10.39	25.39	2.76
SES1.15	255.40	Igneous breccia	1885.9	3242.4	342.43	1062.7	103.88	21.99	53.77	5.32
SES1.16	256.50	Igneous breccia	1488.5	2572.7	266.86	848.7	88.49	20.08	51.27	5.34
SES1.17	256.90	Alvikite	801.0	955.5	135.49	457.3	58.41	15.25	39.01	4.56
SES1.18	257.80	Igneous breccia	1011.6	1602.9	177.97	561.5	58.64	12.66	30.74	3.23
SES1.19	258.50	Igneous breccia	736.5	1214.5	127.58	405.5	42.50	9.51	22.97	2.49
SES1.20	259.90	Igneous breccia	1041.6	1795.7	182.47	575.4	63.71	14.75	37.33	4.46
SES1.21	262.20	Igneous breccia	1802.4	2934.7	325.00	1045.9	115.29	27.15	66.96	7.54
SES1.22	262.65	Igneous breccia	2701.9	4829.4	490.69	1607.0	177.95	42.35	109.48	12.18
SES1.23	263.90	Igneous breccia	2697.3	4315.0	470.77	1538.1	175.52	41.78	109.00	11.59
SES1.24	264.30	Igneous breccia	1901.6	3278.2	327.41	1045.1	113.24	25.84	68.01	6.80
SES1.25	264.70	Igneous breccia	1388.6	2266.6	234.72	737.1	79.74	18.45	50.08	5.27
SES1.26	265.45	Igneous breccia	650.4	1042.9	103.72	320.6	35.41	8.17	23.43	2.70
SES1.27	265.65	Alvikite	1488.3	2104.9	241.82	818.7	107.02	29.23	77.92	8.84
SES1.28	266.00	Alvikite	961.6	1,570.0	161.92	541.3	72.97	20.50	55.47	6.31
SES1.29	266.70	Igneous breccia	2417.7	4172.4	425.37	1382.4	154.53	36.50	99.71	10.38
SES1.30	267.00	Igneous breccia	774.1	1184.2	122.60	372.5	37.96	8.45	23.59	2.68
SES1.31	268.90	Igneous breccia	1588.3	2581.0	259.71	787.2	75.21	16.54	41.93	4.21
SES1.32	269.90	Porphyry	21.7	41.5	4.33	15.0	2.30	0.54	1.59	0.21
SES1.33	270.25	Porphyry	18.5	30.0	3.71	12.8	2.04	0.44	1.40	0.20

Continued from Table 22 – Fortsetung von Tabelle 22

Rare earth elements (ICP-MS) [2/2]		Analyte	Dy	Ho	Er	Tm	Yb	Lu	∑REE	$\sum\mathrm{REE_2O_3}$
		Method	LF200	LF200	LF200	LF200	LF200	LF200	calc.	calc.
		Unit	ppm	ppm	ppm	ppm	ppm	ppm	ppm	%
		MDL	0.05	0.02	0.03	0.01	0.05	0.01	-	-
Sample	**Depth [m]**	**Lithotype**								
SES1.01	**240.90**	**Porphyry**	1.23	0.21	0.58	0.08	0.67	0.09	97.95	0.012
SES1.02	**241.80**	**Porphyry**	1.29	0.19	0.57	0.08	0.60	0.09	138.07	0.016
SES1.03	**242.30**	**Alvikite**	21.07	3.20	7.83	0.97	5.92	0.81	4485.6	0.526
SES1.04	**242.80**	**Alvikite**	22.69	3.52	8.33	1.04	6.26	0.84	4296.9	0.504
SES1.05	**243.80**	**Alvikite**	19.75	3.17	7.47	0.96	5.66	0.80	4009.7	0.470
SES1.06	**244.60**	**Porphyry**	1.18	0.18	0.51	0.07	0.54	0.08	110.8	0.013
SES1.07	**246.40**	**Alvikite**	21.48	3.29	7.79	0.96	5.62	0.75	4093.7	0.480
SES1.08	**248.00**	**Alvikite**	17.20	2.83	7.41	0.94	5.52	0.74	2799.3	0.328
SES1.09	**248.90**	**Alvikite**	13.83	2.23	5.33	0.68	4.00	0.57	1655.2	0.194
SES1.10	**250.10**	**Alvikite**	15.90	2.57	6.08	0.72	4.31	0.56	2467.5	0.289
SES1.11	**251.80**	**Alvikite**	20.36	3.26	7.89	1.02	6.46	0.89	2454.2	0.288
SES1.12	**253.00**	**Igneous breccia**	55.53	8.53	20.26	2.45	14.20	1.84	7458.1	0.875
SES1.13	**253.80**	**Igneous breccia**	10.10	1.64	4.14	0.56	3.58	0.46	2079.4	0.244
SES1.14	**254.40**	**Igneous breccia**	12.46	2.06	5.44	0.73	4.75	0.66	3018.6	0.354
SES1.15	**255.40**	**Igneous breccia**	22.17	3.43	7.85	1.04	6.31	0.82	6858.8	0.804
SES1.16	**256.50**	**Igneous breccia**	23.78	3.56	9.07	1.11	6.39	0.83	5488.1	0.643
SES1.17	**256.90**	**Alvikite**	20.71	3.36	8.03	1.07	6.58	0.86	2601.8	0.305
SES1.18	**257.80**	**Igneous breccia**	14.15	2.12	5.01	0.69	4.09	0.56	3546.2	0.416
SES1.19	**258.50**	**Igneous breccia**	10.63	1.70	4.04	0.53	3.41	0.48	2629.	0.308
SES1.20	**259.90**	**Igneous breccia**	20.59	3.22	7.48	0.95	5.52	0.70	3841.6	0.450
SES1.21	**262.20**	**Igneous breccia**	33.79	5.49	13.78	1.78	10.87	1.49	6544.4	0.767
SES1.22	**262.65**	**Igneous breccia**	55.66	8.79	21.13	2.60	15.20	1.97	10318.0	1.210
SES1.23	**263.90**	**Igneous breccia**	51.80	8.04	20.09	2.53	15.18	2.03	9695.1	1.137
SES1.24	**264.30**	**Igneous breccia**	29.47	4.66	12.08	1.55	9.36	1.25	6963.2	0.816
SES1.25	**264.70**	**Igneous breccia**	23.28	3.76	9.44	1.26	7.95	1.06	4931.9	0.578
SES1.26	**265.45**	**Igneous breccia**	13.10	2.18	5.70	0.78	5.01	0.68	2276.9	0.267
SES1.27	**265.65**	**Alvikite**	40.07	6.31	15.10	1.87	11.38	1.49	5130.9	0.602
SES1.28	**266.00**	**Alvikite**	29.72	4.78	11.82	1.48	9.09	1.23	3580.1	0.420
SES1.29	**266.70**	**Igneous breccia**	49.45	8.37	21.30	2.76	16.12	2.20	9042.1	1.060
SES1.30	**267.00**	**Igneous breccia**	12.51	2.13	5.49	0.71	4.22	0.53	2611.3	0.306
SES1.31	**268.90**	**Igneous breccia**	17.13	2.40	6.01	0.74	4.50	0.60	5451.4	0.639
SES1.32	**269.90**	**Porphyry**	1.15	0.17	0.58	0.07	0.55	0.07	94.96	0.011
SES1.33	**270.25**	**Porphyry**	1.03	0.20	0.65	0.07	0.65	0.09	77.48	0.009

Continued from Table 22 – Fortsetung von Tabelle 22

Trace elements (ICP-MS) [1/4]		**Analyte**	**Be**	**Co**	**Cs**	**Ga**	**Hf**	**Nb**	**Rb**	**Sn**
		Method	**LF200**	**LF200**	**LF200**	**LF200**	**LF200**	**LF200**	**LF200**	**LF200**
		Unit	**ppm**	**ppm**	**ppm**	**ppm**	**ppm**	**ppm**	**ppm**	**ppm**
		MDL	**1**	**0.2**	**0.1**	**0.5**	**0.1**	**0.1**	**0.1**	**1**
Sample	**Depth [m]**	**Lithotype**								
SES1.01	**240.90**	**Porphyry**	4	2.8	11.9	16.2	3.2	7.8	151.9	<1
SES1.02	**241.80**	**Porphyry**	7	3.2	15.0	15.4	3.3	7.7	129.8	<1
SES1.03	**242.30**	**Alvikite**	7	26.9	1.8	8.7	5.2	449.5	15.0	3
SES1.04	**242.80**	**Alvikite**	5	36.5	1.3	11.5	6.7	498.2	18.7	3
SES1.05	**243.80**	**Alvikite**	8	31.5	2.2	11.1	6.5	428.7	13.6	4
SES1.06	**244.60**	**Porphyry**	3	1.6	33.5	16.5	3.0	8.3	152.4	<1
SES1.07	**246.40**	**Alvikite**	5	24.5	1.3	7.5	4.9	425.1	12.0	2
SES1.08	**248.00**	**Alvikite**	8	26.5	1.5	11.2	5.6	321.8	22.5	5
SES1.09	**248.90**	**Alvikite**	7	6.4	0.5	3.1	2.8	352.0	10.9	2
SES1.10	**250.10**	**Alvikite**	5	32.1	3.0	12.4	6.5	368.9	21.5	3
SES1.11	**251.80**	**Alvikite**	8	19.9	5.0	6.4	5.4	547.7	25.1	4
SES1.12	**253.00**	**Igneous breccia**	24	19.2	30.9	17.1	12.1	>1000	129.3	11
SES1.13	**253.80**	**Igneous breccia**	4	5.6	17.7	15.2	5.3	518.1	178.2	5
SES1.14	**254.40**	**Igneous breccia**	8	5.6	14.3	15.2	5.7	515.1	182.4	8
SES1.15	**255.40**	**Igneous breccia**	15	9.0	21.3	15.4	6.6	892.7	157.9	9
SES1.16	**256.50**	**Igneous breccia**	10	13.8	16.1	17.2	8.1	>1000	152.3	9
SES1.17	**256.90**	**Alvikite**	4	14.4	0.7	5.5	4.6	472.0	12.5	3
SES1.18	**257.80**	**Igneous breccia**	9	6.9	11.8	15.6	6.3	763.0	149.7	14
SES1.19	**258.50**	**Igneous breccia**	3	5.2	9.3	15.3	7.3	491.6	120.0	5
SES1.20	**259.90**	**Igneous breccia**	9	6.4	18.6	15.2	6.2	581.2	165.8	8
SES1.21	**262.20**	**Igneous breccia**	22	11.2	26.1	15.0	9.4	876.5	140.9	11
SES1.22	**262.65**	**Igneous breccia**	18	7.5	24.0	15.7	12.8	>1000	152.8	13
SES1.23	**263.90**	**Igneous breccia**	14	8.7	22.2	18.6	14.4	>1000	183.0	15
SES1.24	**264.30**	**Igneous breccia**	14	16.0	23.3	19.2	8.3	>1000	194.8	15
SES1.25	**264.70**	**Igneous breccia**	20	14.9	34.0	16.9	9.6	871.4	189.3	8
SES1.26	**265.45**	**Igneous breccia**	10	4.1	32.4	18.2	7.6	449.4	242.8	6
SES1.27	**265.65**	**Alvikite**	12	23.9	1.0	5.4	5.8	814.9	14.2	4
SES1.28	**266.00**	**Alvikite**	8	23.0	0.8	5.6	6.4	737.0	15.2	4
SES1.29	**266.70**	**Igneous breccia**	37	18.0	29.5	14.8	14.2	>1000	160.2	14
SES1.30	**267.00**	**Igneous breccia**	7	11.2	23.3	18.7	5.8	447.1	196.7	5
SES1.31	**268.90**	**Igneous breccia**	6	5.2	23.0	16.9	7.0	743.7	201.6	12
SES1.32	**269.90**	**Porphyry**	2	1.2	12.5	15.8	3.3	10.0	139.7	<1
SES1.33	**270.25**	**Porphyry**	3	1.8	17.9	16.9	3.4	8.7	151.1	2

Continued from Table 22 – Fortsetung von Tabelle 22

Trace elements (ICP-MS) [2/4]		Analyte	Sr	Ta	Th	U	V	W	Zr	Y
		Method	LF200	LF200	LF200	LF200	LF200	LF200	LF200	LF200
		Unit	ppm	ppm	ppm	ppm	ppm	ppm	ppm	ppm
		MDL	0.5	0.1	0.2	0.1	8	0.5	0.1	0.1
Sample	Depth [m]	Lithotype								
SES1.01	240.90	Porphyry	270.2	0.4	5.4	1.1	19	6.1	129.0	6.3
SES1.02	241.80	Porphyry	191.7	0.3	5.0	3.9	19	14.8	124.9	6.5
SES1.03	242.30	Alvikite	1469.1	11.1	61.1	10.4	203	12.5	331.9	94.6
SES1.04	242.80	Alvikite	1563.1	12.8	74.2	12.9	235	12.7	451.3	95.0
SES1.05	243.80	Alvikite	1286.5	12.3	65.6	12.1	237	23.0	373.7	89.6
SES1.06	244.60	Porphyry	240.2	0.4	5.4	1.8	17	7.0	122.0	5.3
SES1.07	246.40	Alvikite	1827.0	12.0	77.0	13.2	186	21.9	338.2	92.1
SES1.08	248.00	Alvikite	2108.1	11.4	43.3	40.4	304	131.7	316.1	91.6
SES1.09	248.90	Alvikite	4328.8	9.9	39.3	9.2	173	2.7	235.7	60.1
SES1.10	250.10	Alvikite	1949.9	13.0	47.7	12.2	324	17.0	422.9	71.9
SES1.11	251.80	Alvikite	1259.5	19.0	62.6	13.9	157	17.9	445.9	89.9
SES1.12	253.00	Igneous breccia	1525.2	57.1	169.0	71.9	257	178.6	852.4	228.4
SES1.13	253.80	Igneous breccia	441.8	6.8	34.8	19.2	73	28.4	212.8	45.9
SES1.14	254.40	Igneous breccia	502.5	5.6	37.4	25.8	129	24.3	229.6	58.3
SES1.15	255.40	Igneous breccia	755.7	10.1	63.2	63.7	200	55.4	295.7	98.8
SES1.16	256.50	Igneous breccia	1005.2	14.5	73.3	53.1	234	99.2	303.5	101.4
SES1.17	256.90	Alvikite	1907.1	17.1	61.4	15.0	159	34.4	386.1	94.7
SES1.18	257.80	Igneous breccia	763.8	8.3	46.4	30.1	167	68.5	241.0	60.3
SES1.19	258.50	Igneous breccia	553.6	5.6	35.3	22.9	133	30.1	247.7	46.7
SES1.20	259.90	Igneous breccia	872.0	12.1	55.9	35.9	116	47.7	335.2	87.7
SES1.21	262.20	Igneous breccia	1228.8	28.1	87.1	40.1	300	126.4	649.2	152.3
SES1.22	262.65	Igneous breccia	1739.7	43.3	148.5	30.4	301	253.0	788.9	241.7
SES1.23	263.90	Igneous breccia	1696.0	42.1	129.2	27.8	243	125.8	838.5	236.4
SES1.24	264.30	Igneous breccia	925.5	17.5	81.4	102.5	163	205.2	418.4	138.6
SES1.25	264.70	Igneous breccia	907.4	15.5	62.2	64.0	236	107.6	536.2	104.6
SES1.26	265.45	Igneous breccia	552.6	7.2	36.5	42.1	89	85.0	410.3	62.1
SES1.27	265.65	Alvikite	1174.3	18.9	70.0	46.0	156	36.7	494.6	177.9
SES1.28	266.00	Alvikite	2189.9	21.5	84.6	35.2	220	19.8	546.9	131.9
SES1.29	266.70	Igneous breccia	1594.2	32.7	110.2	58.2	255	655.9	1132.9	242.9
SES1.30	267.00	Igneous breccia	606.4	6.3	35.2	55.7	60	58.9	252.8	59.6
SES1.31	268.90	Igneous breccia	806.5	7.1	37.1	24.2	408	98.5	295.2	65.9
SES1.32	269.90	Porphyry	297.5	0.4	4.6	1.0	14	5.4	116.2	5.2
SES1.33	270.25	Porphyry	311.5	0.3	4.4	3.0	13	10.8	117.3	5.7

Continued from Table 22 – Fortsetung von Tabelle 22

Trace elements (ICP-MS) [3/4]		**Analyte**	**Mo**	**Cu**	**Pb**	**Zn**	**Ni**	**As**	**Cd**	**Sb**
		Method	**AQ200**	**AQ200**	**AQ200**	**AQ200**	**AQ200**	**AQ200**	**AQ200**	**AQ200**
		Unit	**ppm**	**ppm**	**ppm**	**ppm**	**ppm**	**ppm**	**ppm**	**ppm**
		MDL	**0.1**	**0.1**	**0.1**	**1**	**0.1**	**0.5**	**0.1**	**0.1**
Sample	**Depth [m]**	**Lithotype**								
SES1.01	**240.90**	**Porphyry**	1.8	25.6	1.7	29	2.5	10.8	<0.1	<0.1
SES1.02	**241.80**	**Porphyry**	4.5	14.4	7.0	13	1.6	17.7	<0.1	<0.1
SES1.03	**242.30**	**Alvikite**	0.4	31.3	31.0	333	70.4	10.7	1.2	0.2
SES1.04	**242.80**	**Alvikite**	0.4	27.2	27.4	306	97.7	7.1	0.7	<0.1
SES1.05	**243.80**	**Alvikite**	0.3	23.0	17.6	309	61.0	6.2	0.8	<0.1
SES1.06	**244.60**	**Porphyry**	1.0	7.9	2.6	26	2.0	9.2	<0.1	<0.1
SES1.07	**246.40**	**Alvikite**	0.4	32.0	16.8	220	47.5	12.6	1.0	<0.1
SES1.08	**248.00**	**Alvikite**	0.8	23.4	8.1	127	58.5	22.5	0.5	<0.1
SES1.09	**248.90**	**Alvikite**	5.3	5.9	38.7	111	17.6	23.8	0.6	1.1
SES1.10	**250.10**	**Alvikite**	0.5	43.1	18.9	142	59.7	4.3	0.5	0.2
SES1.11	**251.80**	**Alvikite**	1.1	19.8	39.1	236	31.1	24.5	1.7	0.5
SES1.12	**253.00**	**Igneous breccia**	18.8	39.8	74.9	253	18.5	251.6	<0.1	1.7
SES1.13	**253.80**	**Igneous breccia**	2.4	36.3	8.8	81	6.1	43.7	<0.1	0.2
SES1.14	**254.40**	**Igneous breccia**	5.5	28.9	12.5	148	6.8	51.6	<0.1	0.3
SES1.15	**255.40**	**Igneous breccia**	8.7	47.6	25.4	207	10.6	146.7	<0.1	0.4
SES1.16	**256.50**	**Igneous breccia**	5.9	15.1	36.2	151	10.2	45.2	<0.1	0.3
SES1.17	**256.90**	**Alvikite**	1.1	4.4	32.3	226	33.7	20.7	3.4	0.4
SES1.18	**257.80**	**Igneous breccia**	3.5	18.1	31.3	180	6.5	108.7	2.2	0.2
SES1.19	**258.50**	**Igneous breccia**	2.0	11.9	24.0	155	6.1	54.9	<0.1	<0.1
SES1.20	**259.90**	**Igneous breccia**	3.4	19.6	20.2	106	6.7	46.7	<0.1	0.5
SES1.21	**262.20**	**Igneous breccia**	11.6	43.5	31.0	376	13.6	102.2	<0.1	0.6
SES1.22	**262.65**	**Igneous breccia**	8.8	26.9	27.9	243	8.3	162.0	<0.1	0.4
SES1.23	**263.90**	**Igneous breccia**	9.6	7.8	27.8	317	8.3	71.0	0.3	0.3
SES1.24	**264.30**	**Igneous breccia**	10.4	10.7	21.8	141	11.4	137.3	0.2	0.3
SES1.25	**264.70**	**Igneous breccia**	12.0	31.8	20.5	328	13.2	113.7	<0.1	0.4
SES1.26	**265.45**	**Igneous breccia**	3.7	17.1	23.3	75	3.6	34.6	<0.1	0.2
SES1.27	**265.65**	**Alvikite**	1.8	38.8	41.0	271	36.2	34.4	1.5	1.0
SES1.28	**266.00**	**Alvikite**	1.3	8.8	44.3	266	36.8	24.7	0.8	1.0
SES1.29	**266.70**	**Igneous breccia**	48.5	13.5	66.5	451	37.1	255.8	<0.1	6.3
SES1.30	**267.00**	**Igneous breccia**	1.3	10.3	10.5	165	6.4	29.4	0.2	0.3
SES1.31	**268.90**	**Igneous breccia**	5.4	6.1	13.9	180	7.2	75.4	<0.1	0.3
SES1.32	**269.90**	**Porphyry**	0.2	3.2	2.0	52	1.1	1.6	<0.1	<0.1
SES1.33	**270.25**	**Porphyry**	0.5	1.3	1.1	21	0.8	5.4	<0.1	<0.1

Continued from Table 22 – Fortsetung von Tabelle 22

Trace elements (ICP-MS) (+ TOT/C; TOT/S) (4/4)		**Analyte**	**Bi**	**Ag**	**Au**	**Hg**	**Tl**	**Se**	**TOT/C**	**TOT/S**
		Method	**AQ200**	**AQ200**	**AQ200**	**AQ200**	**AQ200**	**AQ200**	**TC000**	**TC000**
		Unit	**ppm**	**ppm**	**ppm**	**ppm**	**ppm**	**ppm**	**ppm**	**ppm**
		MDL	**0.1**	**0.1**	**0.5**	**0.01**	**0.1**	**0.5**	**0.02**	**0.02**
Sample	**Depth [m]**	**Lithotype**								
SES1.01	**240.90**	**Porphyry**	<0.1	<0.1	<0.5	<0.01	0.2	<0.5	<0.02	<0.02
SES1.02	**241.80**	**Porphyry**	0.4	<0.1	<0.5	<0.01	0.3	<0.5	<0.02	<0.02
SES1.03	**242.30**	**Alvikite**	0.3	<0.1	3.2	<0.01	<0.1	<0.5	7.10	<0.02
SES1.04	**242.80**	**Alvikite**	0.2	<0.1	4.0	<0.01	<0.1	<0.5	6.29	<0.02
SES1.05	**243.80**	**Alvikite**	0.2	<0.1	7.2	<0.01	<0.1	<0.5	6.54	<0.02
SES1.06	**244.60**	**Porphyry**	0.4	<0.1	<0.5	<0.01	0.7	<0.5	0.04	<0.02
SES1.07	**246.40**	**Alvikite**	<0.1	<0.1	23.3	<0.01	<0.1	<0.5	7.67	0.09
SES1.08	**248.00**	**Alvikite**	<0.1	<0.1	5.0	<0.01	<0.1	<0.5	6.94	0.03
SES1.09	**248.90**	**Alvikite**	0.2	<0.1	14.1	<0.01	<0.1	<0.5	9.90	0.03
SES1.10	**250.10**	**Alvikite**	<0.1	<0.1	8.8	<0.01	<0.1	<0.5	6.79	0.06
SES1.11	**251.80**	**Alvikite**	0.2	<0.1	9.0	<0.01	0.2	<0.5	8.26	0.03
SES1.12	**253.00**	**Igneous breccia**	0.7	<0.1	13.4	0.05	0.7	0.7	0.14	0.04
SES1.13	**253.80**	**Igneous breccia**	0.2	<0.1	36.1	<0.01	0.4	<0.5	0.04	<0.02
SES1.14	**254.40**	**Igneous breccia**	0.3	0.2	10.7	<0.01	0.4	<0.5	0.05	<0.02
SES1.15	**255.40**	**Igneous breccia**	0.9	<0.1	14.7	0.02	0.5	<0.5	0.08	0.04
SES1.16	**256.50**	**Igneous breccia**	0.5	1.2	31.8	0.03	0.4	<0.5	0.09	0.09
SES1.17	**256.90**	**Alvikite**	0.3	<0.1	27.0	<0.01	<0.1	<0.5	8.59	<0.02
SES1.18	**257.80**	**Igneous breccia**	0.4	<0.1	53.9	0.02	0.2	<0.5	0.97	0.03
SES1.19	**258.50**	**Igneous breccia**	0.3	0.3	18.5	<0.01	0.2	<0.5	0.07	<0.02
SES1.20	**259.90**	**Igneous breccia**	0.5	<0.1	1.4	<0.01	0.3	<0.5	0.07	<0.02
SES1.21	**262.20**	**Igneous breccia**	0.4	0.7	40.7	0.04	0.5	0.7	0.08	0.07
SES1.22	**262.65**	**Igneous breccia**	0.4	<0.1	34.4	0.06	0.5	0.8	0.11	0.05
SES1.23	**263.90**	**Igneous breccia**	0.3	<0.1	13.8	<0.01	0.5	1.6	0.30	0.09
SES1.24	**264.30**	**Igneous breccia**	0.5	<0.1	10.6	<0.01	0.4	<0.5	0.07	0.06
SES1.25	**264.70**	**Igneous breccia**	0.4	0.6	22.6	<0.01	0.4	0.9	0.07	0.06
SES1.26	**265.45**	**Igneous breccia**	0.2	0.2	1.6	<0.01	0.3	<0.5	0.08	<0.02
SES1.27	**265.65**	**Alvikite**	0.7	<0.1	17.3	0.02	<0.1	0.8	8.59	0.03
SES1.28	**266.00**	**Alvikite**	0.2	0.2	25.7	<0.01	<0.1	<0.5	8.19	0.03
SES1.29	**266.70**	**Igneous breccia**	0.5	0.2	2.2	<0.01	0.6	1.1	0.06	0.06
SES1.30	**267.00**	**Igneous breccia**	0.4	<0.1	4.3	0.02	0.4	<0.5	0.03	0.04
SES1.31	**268.90**	**Igneous breccia**	0.2	<0.1	37.3	<0.01	0.3	<0.5	0.07	<0.02
SES1.32	**269.90**	**Porphyry**	<0.1	<0.1	<0.5	<0.01	<0.1	<0.5	<0.02	<0.02
SES1.33	**270.25**	**Porphyry**	0.2	<0.1	<0.5	<0.01	<0.1	<0.5	0.05	<0.02

Bibliography

ANDERSEN, A. K.; CLARK, J. G.; LARSON, P. B.; DONOVAN, J. J. (2017): REE fractionation, mineral speciation, and supergene enrichment of the Bear Lodge carbonatites, Wyoming, USA. In *Ore Geology Reviews* 89, pp. 780–807. DOI: 10.1016/j.oregeorev.2017.06.025

ASD Inc. (2012): TerraSpec 4 User Manual. ASD Document 600691. Boulder (Colorado)

ATENCIO, D.; ANDRADE, M. B.; CHRISTY, A. G.; GIERE, R.; KARTASHOV, P. M. (2010): The Pyrochlore Supergroup of Minerals. Nomenclature. In *The Canadian Mineralogist* 48 (3), pp. 673–698. DOI: 10.3749/canmin.48.3.673

BARTINGTON INSTRUMENTS Ltd.: MS2/MS3 Magnetic Susceptibility System. Product brochure. Witney, Oxford. Available online at http://www.bartington.com/Literaturepdf/Datasheets/MS2_MS3%20DS0020.pdf, checked on 1/9/2018

BAYLISS, P. (1989): Mineral Nomenclature. Zirconolite. In *Mineralogical Magazine* 53 (373), pp. 565–569. DOI: 10.1180/minmag.1989.053.373.07

BELL, K.; BLENKINSOP, J.; KWON, S. T.; TILTON, G. R.; SAGE, R. P. (1987): Age and radiogenic isotopic systematics of the Borden carbonatite complex, Ontario, Canada. In *Can. J. Earth Sci.* 24 (1), pp. 24–30. DOI: 10.1139/e87-003

BELL, K.; KJARSGAARD, B. A.; SIMONETTI, A. (1998): Carbonatites - Into The Twenty-First Century. In *Journal of Petrology* 39 (11), pp. 1839–1845. DOI: 10.1093/petrology/39.11.1839

BOYNTON, W. V. (1984): Cosmochemistry of the Rare Earth Elements: Meteorite Studies. In P. Henderson (Ed.): Rare earth element geochemistry, vol. 2. Amsterdam, New York: Elsevier (Developments in Geochemistry, 2), pp. 63–114

BRIGATTI, M. F.; MEDICI, L.; SACCANI, E.; VACCARO, C. (1996): Crystal chemistry and petrologic significance of Fe (super 3+) -rich phlogopite from the Tapira carbonatite complex, Brazil. In *American Mineralogist* 81 (7-8), pp. 913–927. DOI: 10.2138/am-1996-7-814

BROOKINS, D. G. (1988): Eh-pH Diagrams for Geochemistry. Berlin, Heidelberg: Springer Berlin Heidelberg. Available online at http://dx.doi.org/10.1007/978-3-642-73093-1

ČERNÝ, P.; ERCIT, T. S. (1989): Mineralogy of Niobium and Tantalum. In P. Möller, P. Černý, F. Saupé (Eds.): Lanthanides, Tantalum and Niobium. Mineralogy, Geochemistry, Characteristics of Primary Ore Deposits, Prospecting, Processing and Applications Proceedings of a workshop in Berlin, November 1986. Proceedings of a workshop in Berlin, November 1986. Berlin, Heidelberg: Springer Berlin Heidelberg (Special Publication of the Society for Geology Applied to Mineral Deposits, 7), pp. 27–79

CHAKHMOURADIAN, A. R. (2006): High-field-strength elements in carbonatitic rocks. Geochemistry, crystal chemistry and significance for constraining the sources of carbonatites. In *Chemical Geology* 235 (1-2), pp. 138–160. DOI:10.1016/j.chemgeo.2006.06.008

CHAKHMOURADIAN, A. R.; REGUIR, E. P.; ZAITSEV, A. N.; COUËSLAN, C.; XU, C.; KYNICKÝ, J. et al. (2017): Apatite in carbonatitic rocks. Compositional variation, zoning, element partitioning and petrogenetic significance. In *Lithos* 274-275, pp. 188–213. DOI: 10.1016/j.lithos.2016.12.037

CHEN, W.; HONGHUI, H.; BAI, T.; JIANG, S. (2017): Geochemistry of Monazite within Carbonatite Related REE Deposits. In *Resources* 6 (4), p. 51. DOI: 10.3390/resources6040051

CULLERS, R. L.; GRAF, J. L. (1984): Rare Earth Element in Igneous Rocks of the Continental Crust: Predominantly Basic and Ultrabasic Rocks. In P. Henderson (Ed.): Rare earth element geochemistry. Amsterdam, New York: Elsevier (Developments in Geochemistry, 2), pp. 237–274

DENG, M.; XU, C.; SONG, W.; TANG, H.; LIU, Y.; ZHANG, Q. et al. (2017): REE mineralization in the Bayan Obo deposit, China. Evidence from mineral paragenesis. In *Ore Geology Reviews*

91, pp. 100–109. DOI: 10.1016/j.oregeorev. 2017.10.018

EHLING, B.-C. (2008): Kambrium. In G. H. Bachmann, B.-C. Ehling, R. Eichner, M. Schwab (Eds.): Geologie von Sachsen-Anhalt. Stuttgart: Schweizerbart, pp. 65–70

FERRARIS, G.; IVALDI, G. (2002): Structural Features of Micas. In *Reviews in Mineralogy and Geochemistry* 46 (1), pp. 117–153. DOI: 10.2138/rmg.2002.46.03

FLEET, M. E.; DEER, W. A.; HOWIE, R. A.; ZUSSMAN, J. (2003): Micas. 2nd ed. Rock-forming Minerals, 3A: Geological Society. London

GIERE, R.; LUMPKIN, G. R.; WILLIAMS, C. T. (1998): Chemical characteristics of natural zirconolite. In *Schweizerische Mineralogische und Petrographische Mitteilungen* 78, pp. 433–459. DOI: 10.5169/SEALS-59299

GILKES, R. J. (1979): Biotite Alteration in Deeply Weathered Granite. I. Morphological, Mineralogical, and Chemical Properties. In *Clays and Clay Minerals* 27 (5), pp. 349–360. DOI: 10.1346/CCMN.1979.0270505

HAUFF, P. L. (2005): Applied Reflectance Spectroscopy with emphasis on data collection and datainterpretation using field spectrometers. Spectral International Inc. Sydney

HEIM, D. (1990): Tone und Tonminerale. Grundlagen der Sedimentologie und Mineralogie. Stuttgart: Enke

IWAN, L. (2017): Nutzung schneller Scanverfahren zur Charakterisierung von SEE-Vererzungen in Karbonatiten am Beispiel von Storkwitz. Master thesis. Martin-Luther-Universität, Halle [unpublished]

KRÜGER, J. C.; ROMER, R. L.; KÄMPF, H. (2013): Late Cretaceous ultramafic lamprophyres and carbonatites from the Delitzsch Complex, Germany. In *Kimberlite, carbonatite, and potassic magmatism as part of the geochemical cycle* 353 (Supplement C), pp. 140–150. DOI: 10.1016/j.chemgeo. 2012.09.026

LE MAITRE, R. W.; STRECKEISEN, A.; ZANETTIN, B.; LE BAS, M. J.; BONIN, B.; BATEMAN, P. (2002): Igneous Rocks. Cambridge: Cambridge University Press

LOTTERMOSER, B. G. (1990): Rare-earth element mineralisation within the Mt. Weld carbonatite laterite, Western Australia. In *Lithos* 24 (2), pp. 151–167. DOI: 10.1016/0024-4937(90)90022-S

LOTTERMOSER, B. G.; ENGLAND, B. M. (1988): Compositional variation in pyrochlores from the Mt Weld carbonatite laterite, Western Australia. In *Mineralogy and Petrology* 38 (1), pp. 37–51. DOI: 10.1007/BF01162480

LUMPKIN, G.R. (1999): Physical and chemical characteristics of baddeleyite (monoclinic zirconia) in natural environments. An overview and case study. In *Journal of Nuclear Materials* 274 (1), pp. 206–217. DOI: 10.1016/S0022-3115(99)00066-5

MARIEN, C. (2014): Mineralogische Charakterisierung von Karbonatitproben aus der Bohrung Wis-BAW 768/78. Master thesis. Martin-Luther-Universität, Halle [unpublished]

MARIEN, C.; FIEDLER, M.; EHLING, B.-C.; UHDE, B.; BORG, G. (2012): Charakterisierung von Lamprophyren und Karbonatiten im Nordteil des Delitzsch Komplexes (Sachsen-Anhalt). In Deutsche Geologische Gesellschaft – Geologische Vereinigung (Ed.): SDGG Heft 80. GeoHannover 2012. Hannover (Schriftenreihe der Deutschen Gesellschaft für Geowissenschaften, 80), p. 53

MCDONOUGH, W. F.; SUN, S.-s. (1995): The composition of the Earth. In *Chemical Geology* 120 (3-4), pp. 223–253. DOI: 10.1016/0009-2541(94)00140-4

MEISSNER, B. (1964): Zu den bisherigen Ergebnissen des Objektes Kartierung Magnetanomalie Delitzsch. In *Wissenschaftlich-Technischer Informationsdienst* 5 (4), pp. 28–29

MELGAREJO, J. C.; MARTIN, R. F. (2011): Atlas of non-silicate minerals in thin section. Québec: Mineralogical Assoc. of Canada (The Canadian mineralogist Special publication, 7)

MENG, D.; WU, X.; HAN, Y.; MENG, X. (2002): Polytypism and microstructures of the mixed-layer member B_2S, $CaCe_3(CO_3)_4F_3$ in the bastnaesite-(Ce)–synchysite-(Ce) series. In *Earth and Planetary Science Letters* 203 (3), pp. 817–828. DOI: 10.1016/S0012-821X(02)00947-0

MIGDISOV, A.; WILLIAMS-JONES, A. E.; BRUGGER, J.; CAPORUSCIO, F. A. (2016): Hydrothermal transport, deposition, and fractionation of the REE. Experimental data and thermodynamic calculations. In *Chemical Geology* 439, pp. 13–42. DOI: 10.1016/j.chemgeo.2016.06.005

MITCHELL, R. H. (2005): CARBONATITES AND CARBONATITES AND CARBONATITES. In *The Canadian Mineralogist* 43 (6), pp. 2049–2068. DOI: 10.2113/gscanmin.43.6.2049

MITCHELL, R. H. (2015): Primary and secondary niobium mineral deposits associated with carbonatites. In *Ore Geology Reviews* 64, pp. 626–641. DOI: 10.1016/j.oregeorev. 2014.03.010

PANINA, L. I.; MOTORINA, I. V. (2008): Liquid immiscibility in deep-seated magmas and the generation of carbonatite melts. In *Geochem. Int.* 46 (5), pp. 448–464. DOI: 10.1134/S0016702908050029

PETERSON, T. D.; SCOTT, J. M. J.; JEFFERSON, C. W. (2011): Uranium-rich bostonite-carbonatite dykes in Nunavut: recent observations

PLÁŠIL, J. (2017): Structural complexity of uranophane and uranophane-β. Implications for their formation and occurrence. In *Eur.J.Mineral. DOI:* 10.1127/ejm/2017/0029-2691

POTHEN, F. (2013): Dynamic Market Power in an Exhaustible Resource Industry. The Case of Rare Earth Elements. Centre for European Economic Research (Discussion Paper, 14-005). Available online at http://ftp.zew.de/pub/zew-docs/dp/dp14005.pdf, checked on 4/6/2018

REGUIR, E. P.; CHAKHMOURADIAN, A. R.; HALDEN, N. M.; MALKOVETS, V. G.; YANG, P. (2009): Major- and trace-element compositional variation of phlogopite from kimberlites and carbonatites as a petrogenetic indicator. In *Lithos* 112, pp. 372–384. DOI: 10.1016/j.lithos.2009.05.023

REICHERT, J.; FIEDLER, M.; EHSER, A. (2015): Abschlussbericht zur Erlaubnis "Delitzsch". (gemäß §11 Nr. 3 BBergG). Ceritech AG. Leipzig [unpublished]

RÖLLIG, G.; KAMPE, A.; STEINBACH, V.; EHLING, B.-C.; WASTERNACK, J. (1995): Der Untergrund des deutschen Braunkohlereviers. In *Zeitschrift für Geologische Wissenschaften* 23, pp. 3–26

RÖLLIG, G.; VIEHWEG, M.; REUTER, N. (1990): The ultramafic lamprophyres and carbonatites of Delitzsch/GDR. In *Zeitschrift für Angewandte Geologie* 36 (2), pp. 49–54

ROSENBLUM, S.; FLEISCHER, M. (1995): The distribution of rare-earth elements in minerals of the monazite family. -. Washington, D. C.: Unites States Gouvernment Printing Office (U.S. Geological Survey Bulletin, 2140)

RÖSLER, H. J. (1991): Lehrbuch der Mineralogie. 5., unveränd. Aufl. Leipzig: Dt. Verl. für Grundstoffindustrie

RYAN, J. G.; SHERVAIS, J. W.; LI, Y.; REAGAN, M. K.; LI, H. Y.; HEATON, D. et al. (2017): Application of a handheld X-ray fluorescence spectrometer for real-time, high-density quantitative analysis of drilled igneous rocks and sediments during IODP Expedition 352. In *Chemical Geology* 451, pp. 55–66. DOI: 10.1016/j.chemgeo.2017.01.007

SCHANDL, E. S.; GORTON, M. P. (2004): A Textural and geochemical guide to the identification of hydrothermal monazite. Criteria for selection of samples for dating epigenetic hydrothermal ore deposits. In *Economic Geology* 99 (5), pp. 1027–1035. DOI: 10.2113/gsecongeo.99.5.1027

SCHWAB, M.; EHLING, B.-C. (2008): Karbon. In G. H. Bachmann, B.-C. Ehling, R. Eichner, M. Schwab (Eds.): Geologie von Sachsen-Anhalt. Stuttgart: Schweizerbart, pp. 110–140

SELTENERDEN STORKWITZ AG (2012): Erfolgsfaktoren für die Förderung des sächsischen Seltenenerden Vorkommens; Die strategischen Ansätze der Seltenerden Storkwitz AG. [unpublished report]

SICIUS, H. (2016): Seltenerdmetalle: Lanthanoide und dritte Nebengruppe. Eine Reise durch das Periodensystem. Wiesbaden: Springer Spektrum Fachmedien (Essentials)

STANDKE, G. (1995): Horizontkarten des Tertiärs in Sachsen. In *Zeitschrift für Geologische Wissenschaften* 23, pp. 103–117

STRECKEISEN, A. (1979): Classification and nomenclature of volcanic rocks, lamprophyres, carbonatites, and melilitic rocks. Recommendations and suggestions of the IUGS Subcommission on the Systematics of Igneous Rocks. In *Geol* 7 (7), p. 331. DOI: 10.1130/0091-7613(1979)7<331:CANOVR> 2.0.CO;2

SYKES, D.; BAKER, M. B.; WYLLIE, P. J. (1992): Viscous properties of carbonate melts at high pressure. In *Eos, Transactions of the American Geophysical Union* (73), p. 372

TISCHENDORF, G.; FOERSTER, H.-J.; GOTTESMANN, B. (1999): The correlation between lithium and magnesium in trioctahedral micas. improved equations for $_{Li2O}$ estimation from MgO data. In *Mineralogical Magazine* 63 (1), pp. 57–74

UHDE, B. (2011): Petrographische und geochemische Untersuchungen an Lamprophyren, Brekzien und Nebengesteinen des Ultramafitit-Karbonatit-Komplexes von Delitzsch. Diplomarbeit. Martin-Luther-Universität Halle-Wittenberg, Halle [unpublished]

VERPLANCK, PHILIP L. (2017): The Role of Fluids in the Formation of Rare Earth Element Deposits. In *Procedia Earth and Planetary Science* 17, pp. 758–761. DOI: 10.1016/j.proeps.2017.01.014

VONCKEN, J. H. L. (2016): The rare earth elements. An introduction. Cham: Springer (SpringerBriefs in Earth Sciences)

WAGNER, G. A.; COYLE, D. A.; DUYSTER, J.; HENJES-KUNST, F.; PETEREK, A.; SCHRÖDER, B. et al. (1997): Post-Variscan thermal and tectonic evolution of the KTB site and its surroundings. In *Journal of Geophysical Research* 102 (B8), pp. 18.221-18.232

WALTER, H.; SCHNEIDER, J. W. (2008): Perm. In W. Pälchen, H. Walter (Eds.): Geologie von Sachsen. Geologischer Bau und Entwicklungsgeschichte. Stuttgart: Schweizerbart (Geologie von Sachsen), pp. 223–257

WASTERNACK, J. (2008): Ultramafit- Karbonatit-Komplex von Delitzsch. In W. Pälchen, H. Walter (Eds.): Geologie von Sachsen. Geologischer Bau und Entwicklungsgeschichte. Stuttgart: Schweizerbart (Geologie von Sachsen), pp. 478–482

WHITNEY, D. L.; EVANS, B. W. (2009): Abbreviations for names of rock-forming minerals. In *American Mineralogist* 95 (1), pp. 185–187. DOI: 10.2138/am.2010.3371

WISMUT GMBH (1999): Chronik der Wismut. Chemnitz

WOOLLEY, A. R. (1989): The spatial and temporal distribution of carbonatites. In K. Bell (Ed.): Carbonatites. Genesis and evolution. London, Boston: Unwin Hyman, pp. 15–37

WOOLLEY, A. R.; KEMPE, D. R. C. (1989): Carbonatites: nomenclature, average chemical composition and element distribution. In K. Bell (Ed.): Carbonatites. Genesis and evolution. London, Boston: Unwin Hyman, pp. 1–14

WOOLLEY, A. R.; KJARSGAARD, B. A. (2008): Carbonatite occurrences of the world. Map and database

ZEH, A.; GERDES, A. (2010): Baltica- and Gondwana-derived sediments in the Mid-German Crystalline Rise (Central Europe). Implications for the closure of the Rheic ocean. In *Gondwana Research* 17 (2-3), pp. 254–263. DOI: 10.1016/j.gr.2009.08.004

Herausgeber:
Sächsisches Landesamt für Umwelt, Landwirtschaft und Geologie (LfULG)
Pillnitzer Platz 3, 01326 Dresden
Telefon: + 49 351 2612-0
Telefax: + 49 351 2612-1099
E-Mail: lfulg@smul.sachsen.de
www.lfulg.sachsen.de

Autoren:
Max Niegisch, Andreas Kamradt, Gregor Borg
Fachgruppe Petrologie und Lagerstättenforschung
Institut für Geowissenschaften und Geographie
Martin-Luther-Universität Halle-Wittenberg
Von-Seckendorff-Platz 3, 06120 Halle (Saale)
Telefon: +49 345 55 26111
Telefax: +49 345 55 27180
E-Mail: max_niegisch@yahoo.de
andreas.kamradt@geo.uni-halle.de
gregor.borg@geo.uni-halle.de

Fotos:
Autoren

Redaktionsschluss:
12.02.2020

ISSN:
0863-2200

Täglich für
ein gutes Leben.

www.lfulg.sachsen.de